

Event Topology Classifiers at the Large Hadron Collider

Suraj Prasad^{1,*}, Sushanta Tripathy^{2,†}, Bhagyarathi Sahoo^{1,‡} and Raghunath Sahoo^{1,§}

¹*Department of Physics, Indian Institute of Technology Indore,
Simrol, Indore, 453552, Madhya Pradesh, India and*

²*Division of Particle and Nuclear Physics, Department of Physics, Lund University, Lund, 22364, Sweden*
(Dated: June 12, 2025)

Event classifiers are the most fundamental observables to probe the system size and event topology of high-energy collisions. Significant progress has been made to establish suitable event classifiers to probe different physics processes occurring in elementary e^+e^- to heavy-ion collisions in a range of center of mass energies. One of the major motivations to revisit event classifiers at the Large Hadron Collider (LHC) originates from the recent measurements of high multiplicity proton-proton collisions, which have revealed that these small collision systems exhibit features similar to the formation of quark-gluon plasma (QGP), traditionally believed to be only achievable in heavy nucleus-nucleus collisions at ultra-relativistic energies. To pinpoint the origin of these QGP-like phenomena with substantially reduced auto-correlation and selection biases, and to bring all collision systems on equal footing, along with charged-particle multiplicity, lately several event topology classifiers such as transverse sphericity, transverse spherocity, relative transverse activity classifier, and charged-particle flattenicity have been used extensively in experiments as well as in the phenomenological front. In this review article, we extensively discuss the purpose, coverage, and usage guidelines of these event shape classifiers, which can be crucial given the upcoming measurements in a precision era during Runs 3 and 4 of the LHC. In most cases, the event shape observables are found to be better probes in understanding the heavy-ion-like behavior seen at the LHC, while making a multi-differential study of multihadron production dynamics in hadronic and nuclear collisions.

CONTENTS

I. Introduction	2	B. For Pb–Pb collisions: AMPT	21
II. Event Classifiers	4	IV. Interpretation of QGP-like signals with event classifiers	21
A. Different types of events: elastic and inelastic collisions	4	A. Integrated yield and transverse momentum spectra	21
B. Impact parameter and centrality	4	B. Average transverse momentum	24
C. Charged-particle multiplicity (N_{ch})	6	C. Strangeness enhancement	29
D. Number of multi-partonic interactions (N_{mpi})	7	D. Baryon-to-meson ratios and radial flow	32
E. Transverse sphericity (S_T)	8	E. Particle correlations and anisotropic flow	39
F. Transverse spherocity (S_0)	9	F. Searches for jet-quenching	43
1. Infrared Safety	9	V. Extension to heavy-ion collisions	45
2. Collinear Safety	10	A. Transverse Spherocity	45
G. Relative transverse activity classifier (R_T)	11	1. Two-particle correlations and anisotropic flow	46
H. Charged-particle flattenicity (ρ_{ch})	13	2. Eccentricity and elliptic flow fluctuations	48
I. Flow vectors (q_n)	15	3. Symmetry Plane Correlations	50
J. Aplanarity (A)	16	4. Kinetic freeze-out temperature and radial flow	54
K. Thrust, major and minor, oblateness	16	B. Reduced flow vectors (q_n)	54
L. Heavy-jet mass (M_H)	17	C. Role of machine learning	56
M. Jet broadening variables B_T and B_W	17	VI. Final words on each classifier	59
III. Model calculations	19	VII. Outlook	60
A. For pp collisions: PYTHIA 8	20	Acknowledgments	62
1. Color Reconnection	20	References	63
2. Rope Hadronisation	20		

* Suraj.Prasad@cern.ch

† Sushanta.Tripathy@cern.ch

‡ Bhagyarathi.Sahoo@cern.ch

§ Corresponding Author: Raghunath.Sahoo@cern.ch

I. INTRODUCTION

To understand the infancy of our Universe and its evolution, the little bangs of heavy-ions are made in collider experiments like the Large Hadron Collider (LHC) at CERN, Switzerland, and the Relativistic Heavy-Ion Collider (RHIC) at BNL, USA, which reproduces the conditions that happened during the fraction of a second after the Big-Bang. The collision of two nuclei produces a hot and dense system of deconfined quarks and gluons for a short time (order of a few fm/c or 10^{-23} sec). This deconfined and thermalized state of quarks and gluons is often referred to as quark-gluon plasma (QGP). Due to a very short timescale, it is impossible to probe QGP directly. However, several indirect signatures are proposed, such as the presence of strangeness enhancement, quarkonia suppression, jet quenching, collective flow, direct photon production, and direct dilepton production, which validate the presence of QGP. In proton-proton (pp) collisions, where the system size is significantly smaller than Pb-Pb, the main hard parton-parton scatterings produce high transverse momentum (p_T) particles which can be described by the perturbative quantum chromodynamics (pQCD). In the hard regime of QCD, jets are produced from parton scatterings at large p_T . As in this regime, the coupling constant (α_s) is significantly small, precise pQCD calculations can be performed. The semi-hard and soft parton scatterings, which are not a part of the main hard scatterings, form the underlying event (UE) [1, 2]. As the soft-QCD calculations are cumbersome due to a larger value of α_s , the description of the UE is modeled using different QCD-inspired phenomenological approaches [3]. At the LHC energies, due to high parton densities and the composite nature of hadrons, more than one binary interaction among partons is possible in a single pp collision, which is often referred to as multi-parton interactions (MPI) [4]. The MPI phenomenon has been widely supported by experimental data [5, 6] and is one of the key ingredients in the Monte Carlo event generators. In such MPI-based models, the final state in pp collisions is sensitive to the modeling of MPI and non-perturbative effects in the final state, such as color reconnection (CR) and color Ropes, which are modeled in PYTHIA 8 [7] (See Figs. 1 and 2).

Recent measurements of high multiplicity pp collisions at the LHC energies have revealed that these systems exhibit features similar to quark-gluon plasma, such as the presence of radial and elliptic flow [8–16] and enhanced production of strange hadrons with respect to that of charged pions [17–19], traditionally believed to be only achievable in ultra-relativistic nucleus-nucleus collisions. These measurements may point towards a common underlying physics mechanism across collision systems. However, no jet quenching signatures have been reported in small collision systems [20, 21]. The event generators currently available with relevant physics models fail to simultaneously reproduce all the observed phenomena in small collisions. This makes the origin of QGP-like phe-

nomena observed in small systems like pp and p-Pb unclear. Out of several theoretical models, the explanations from the MPI-based models with final state non-pQCD phenomena like CR [7], rope hadronisation [22, 23], and string shoving [24], inherited in PYTHIA8, are able to explain many of the QGP-like signatures in pp collisions. MPI is a phenomenological phenomenon and can not be measured in experiments. Thus, many experimental measurements are performed as a function of charged particle multiplicity in the final state, which has a strong correlation with MPI in MC models. On the other hand, the measurements with charged particle multiplicity show a stronger than linear increase of high- p_T particle yields in high-multiplicity (HM) pp collisions relative to that of minimum bias (MB) events. This signifies a selection bias towards local fluctuations of choosing only hard pp collisions. Such biases can be removed when the event selection is performed with multiplicity measured in a different pseudorapidity interval with respect to the observable of interest. However, it is found that such measurements are still biased by the hard processes contributing to the high- p_T particles [26]. Thus, in small collision systems, such selection biases in the measurements hinder the search for the origin of QGP-like behavior.

To pindown the origin of QGP-like phenomena with substantially diminished selection bias and to bring all the collision systems in an equal footing, along with charged-particle multiplicity (N_{ch}), lately event shape observables such as transverse sphericity (S_0) and transverse sphericity (S_T) are inherited from the usage in e^+e^- collisions since late 1970s [27–30]. Additionally, there are other proposed event shape observables which are used in heavy-ion collisions and jet studies such as third-jet resolution parameter, y_{23} [31–33]; aplanarity, A ; transverse thrust, τ_T ; its minor component, $T_{\perp, \min}$ [34–36]; \mathcal{F} -parameter [37], reduced flow vector, q_2 [38]; and event isotropy [39]. Moreover, several new event shape observables have been recently constructed, for example, relative transverse activity classifiers such as R_T , R_T^{\min} , and R_T^{\max} developed by P. Skands *et. al.* and charged-particle flattenicity (ρ_{ch}) developed by A. Ortiz *et. al.* to reduce the sensitivity to hard processes compared to the classifiers measured based only on charged-particle multiplicity [40–43]. In both experiments as well as in the phenomenological fronts, extensive explorations using the above-mentioned event-shape observables have been performed [25–55]. Also, we have explored the particle production dynamics as a function of transverse sphericity for light, strange [56–60] and heavy flavor [61, 62] sector in proton-proton collisions. The possibility of thermalization in small collision systems has been explored using sphericity as an event-shape observable in Ref. [63, 64]. The global observables, identified particle production, and anisotropic flow coefficients are studied as a function of transverse sphericity in Pb–Pb collisions in Refs. [65–71].

Event shape observables describe the structure of

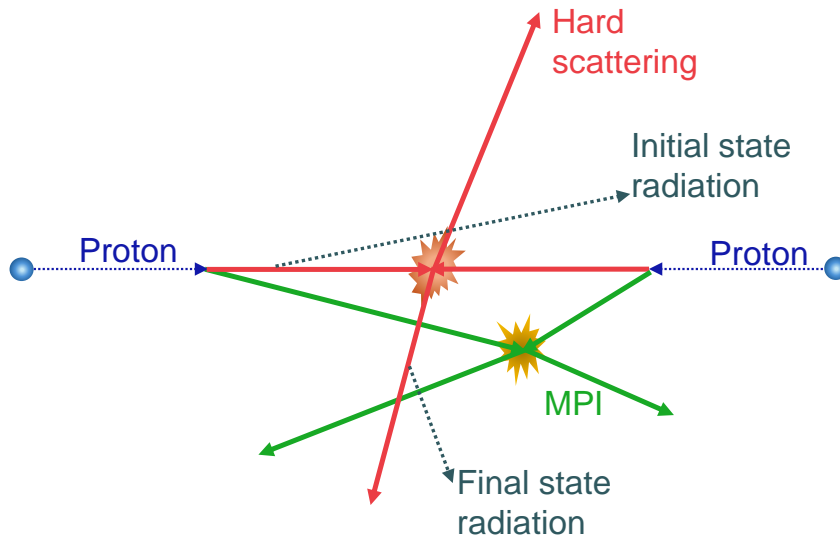


FIG. 1. Pictorial representation of multi-partonic interactions (MPI) in pp collisions.

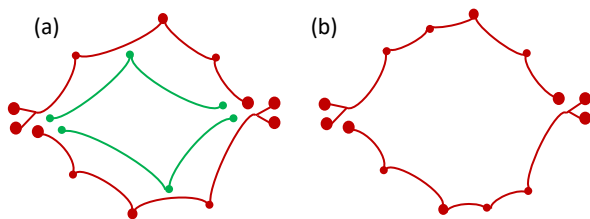


FIG. 2. Pictorial representation of Color Reconnection (CR) in the string fragmentation model. (a) two independent hard scatterings, (b) color reconnected string

hadronic events and properties of their energy flow. Event shape observables are among the first observables proposed to test QCD, and they have played a key role in the progress of understanding of both perturbative and nonperturbative aspects of QCD [27–30]. Event shape in the hadronic collisions was investigated first at the Intersecting Storage Rings [72] and at the $SppS$ [73, 74] at CERN to examine the emergence of jets. Later, event shape observables are explored at Tevatron to study the dependence of transverse energy of the leading jet and contribution from underlying events [75]. In e^+e^- collisions, event shape variables are the popular observables to improve our understanding of QCD dynamics. In e^+e^- and ep deep-inelastic scattering experiment, the study of hadronic final state as a function of event shape has allowed to test the predictions of pQCD and extrac-

tion of strong interaction coupling constant α_s [76–82]. In the late 1970s, event shape observables were instrumental in studying the nature of gluon bremsstrahlung. One of the key results that were confirmed from the usage of event shape observables in experiments is the deduction of gluons as vector particles, although the theoretical prediction during that time suggested that gluons are scalar in nature. Event shape observables have the capability to distinguish the collisions based on their geometrical shapes, and they can measure the extent to which energy flow departs from a dijet structure in an event. Event shape observables are required to possess the property of continuous globalness and are normally categorised in three types, i.e., directly global observables, global observables shared with exponentially suppressed forward terms, and shared with recoil terms (indirectly global observables) [30]. The discussed event shapes in this article fall into the directly global observables category. Event shape observables are expected to be instrumental to test QCD as, by construction, they are collinear and infrared safe observables [29] (see next section for more details). Thus, they do not change their value if a parton is split into two collinear partons or an extra soft gluon is added. This is an important condition for the cancellation of divergences associated with such gluon emissions, which makes them ideal tools for making finite pQCD predictions. In addition, these event-shape classifiers have shown a significant correlation with the number of MPI (N_{mpi}), which makes them the ideal tool for the understanding of QGP-like effects.

In this review article, we extensively discuss the purpose, coverage, and usage guidelines of these event shape classifiers, which can be crucial in view of the upcom-

ing measurements in the precision era at the LHC. Since 1970, there have been several event classifiers proposed and studied. We will mostly highlight the event classifiers which are popular in the early 21st century since the commencement of the LHC in view of the studies of small collision systems at the LHC. We will briefly discuss the most fundamental event classifier for the high energy collisions, i.e, the charged-particle multiplicity measured both in mid and forward rapidities. Then the discussion will be followed by transverse sphero(i)city, which uses the information of charged-particle transverse momenta and the azimuthal angle for each particle. Then, we will discuss the event shape classifiers such as R_T , R_T^{\min} , and R_T^{\max} , which take the advantage of the underlying event and uses the information of charged-particle multiplicity in the transverse region and azimuthal angle of the particles. Last but not least, the study will be focused on a relatively new event shape classifier, charged-particle flattenicity, which takes the information of transverse momentum, pseudorapidity, and azimuthal angle of final state particles. Along with their novelty, the above-discussed event classifiers show significant correlation with N_{mpi} , which will be extensively discussed in the next section. In most cases, the event shape observables are found to be better probes in understanding the heavy-ion-like behavior seen at the LHC. However, the coverage of event shape classifiers usually overlaps with each other. Thus, one needs to have a better understanding of these classifiers while using them. Keeping this in mind, we will summarise the findings from the experimental and phenomenological front, done so far, and we will provide the usage recommendations of these event classifiers. Eventually, to bring all collision systems on equal footing, we will also discuss the extension of these event topology classifiers to heavy-ion collisions, where the particle density in phase space is higher than pp collisions. In this direction, the usefulness of machine learning is highlighted. Given that our focus in this review is to summarise event topology classifiers, rather than studying all possible theoretical/phenomenological models. We pick up two of the widely used event generators, i.e., PYTHIA 8 for pp collisions and A Multi-Phase Transport (AMPT) [83, 84] for heavy-ion collisions, for some of the studies done here for a better understanding of event shapes and multihadron production dynamics. Wherever available, we will discuss the experimental results based on event classifiers.

The paper is organized as follows. We begin with a brief introduction and motivation about the event shape observables in Sec. I. In Sec. II, we define each event classifier. Section III describes event generation methodology and event/track selection criteria used in this study according to experiments. Section IV discusses the results, especially highlighting selection biases, correlation among the classifiers, and particle ratios obtained in pp collisions. Further, we extend the discussion of event shape studies to heavy-ion collisions and the application of machine learning techniques in Sec. V. The impor-

tant findings of each event classifier are summarized in Sec. VI. Finally, Sec. VII presents the summary and provides a brief outlook.

II. EVENT CLASSIFIERS

In this section, we define different event shape observables used at the LHC energies. In addition, the correlation of these event shape observables with the number of multi-partonic interactions (N_{mpi}) is shown and discussed.

A. Different types of events: elastic and inelastic collisions

The final state particle production in hadronic collisions, such as proton-on-proton, is a probe for the initial interactions among the colliding hadrons. An interaction can be classified as elastic or inelastic. In elastic collisions, the incoming and outgoing protons are the same, which takes place via exchange of Pomeron¹ [85]. In contrast, in inelastic collisions, the final state particles are not identical to the initial colliding protons. An inelastic event can be diffractive, which is signified by a small energy exchange between the protons. Sometimes, one or both protons interact with the Pomerons and dissociate into multiple final-state particles. The event is single diffractive (SD) if only one proton dissociates while the other one survives as it is ($p + p \rightarrow p + X$). Similarly, when both the protons dissociate to form multiple particles in the final state, it is called a double diffractive (DD) event ($p + p \rightarrow X_1 + X_2$). Sometimes, two Pomerons are exchanged and both the protons survive along with the production of new particles, i.e., $p + p \rightarrow p + p + X$, it is called a central diffractive (CD) event. Additionally, when more than two Pomerons are exchanged, there is a possibility for both protons to dissociate and lead to the production of new particles. These events are usually accompanied by large particle multiplicity in the final state as compared to other diffractive events. Figure 3 shows the pictorial representation of different types of possible interactions in pp collisions. The inelastic events without SD are called Non-Single Diffractive (NSD). At the LHC, the measurements are usually performed for NSD or inelastic (INEL) events.

B. Impact parameter and centrality

The impact parameter (b) of a collision is one of the key parameters that substantially influence the particle

¹ Pomeron is a colour singlet particle that dominates the elastic scatterings at high energies and has the quantum numbers of the vacuum.

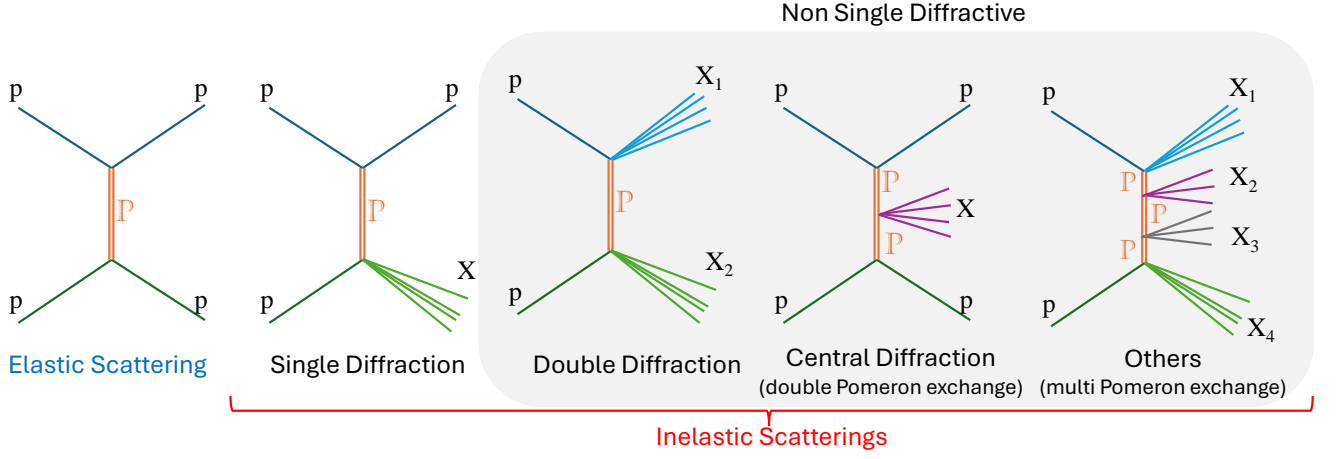


FIG. 3. Schematic showing different types of interactions in pp collisions.

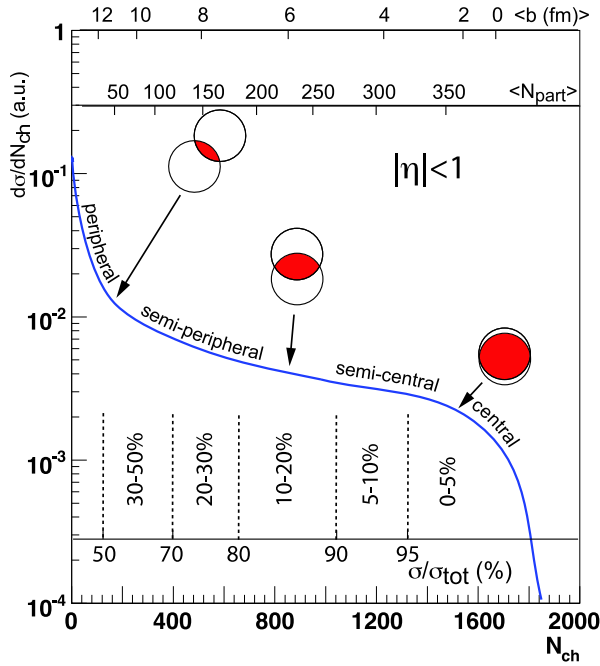


FIG. 4. A schematic representation of the correlation between the final state charged-particle multiplicity distribution (N_{ch}) with the Glauber calculated quantities (b , and N_{part}). The collision centrality classification in experiments is shown explicitly. Figure taken from Ref. [86]

production in the final state. However, its measurement is not trivial in experiments as the length scale of the

impact parameter ranges in the level of a few fermis. Thus, experimental data are typically categorised by the centrality, defined as percentile of events obtained from the number of produced particles or by the number of participant nucleons, N_{part} that is registered in detectors through the estimation of number of spectator nucleons via $N_{part} = 2A - N_{spec}$, where A is the mass number and N_{spec} is the number of spectator nucleons. For example, in ALICE experiment, N_{spec} is given by E_{ZDC}/E_A , where, E_{ZDC} is the energy deposited in zero-degree calorimeters (ZDC) and E_A is beam energy per nucleon. Centrality allows for dividing events into different classes. However, phenomenologically, one needs to assign an impact parameter to a given centrality as depicted in Fig. 4. Thus, theoretical techniques, using the Glauber formalism [86–89] have been developed to allow the estimation of impact parameter along with the number of participant nucleons from experimental data, which considers multiple scattering of nucleons in nuclear targets. Here, we briefly explain how the total inelastic cross-section, the number of binary collisions, and the number of participants depend on the impact parameter.

For a collision of two heavy-nuclei, A and B at relativistic speeds with impact parameter \mathbf{b} as shown in Fig. 5, the inelastic cross-section can be defined as

$$\sigma_{AB}^{inel}(\mathbf{b}) = \int 2\pi b \, db \left[1 - (1 - T_{AB}(\mathbf{b})\sigma_{NN}^{inel})^{AB} \right] \quad (1)$$

$$\simeq \int 2\pi b \, db \left[1 - \exp[-ABT_{AB}(\mathbf{b})\sigma_{NN}^{inel}] \right] \quad (2)$$

Here, $T_{AB}(\mathbf{b})$ is the nuclear overlap function and σ_{NN}^{inel} denotes the nucleon-nucleon inelastic cross-section. For such nucleus-nucleus collisions, the total number of binary collisions is given as:

$$N_{coll}^{AB}(\mathbf{b}) = \sum_{n=1}^A nP(n, \mathbf{b}) = ABT_{AB}(\mathbf{b})\sigma_{NN}^{inel}, \quad (3)$$

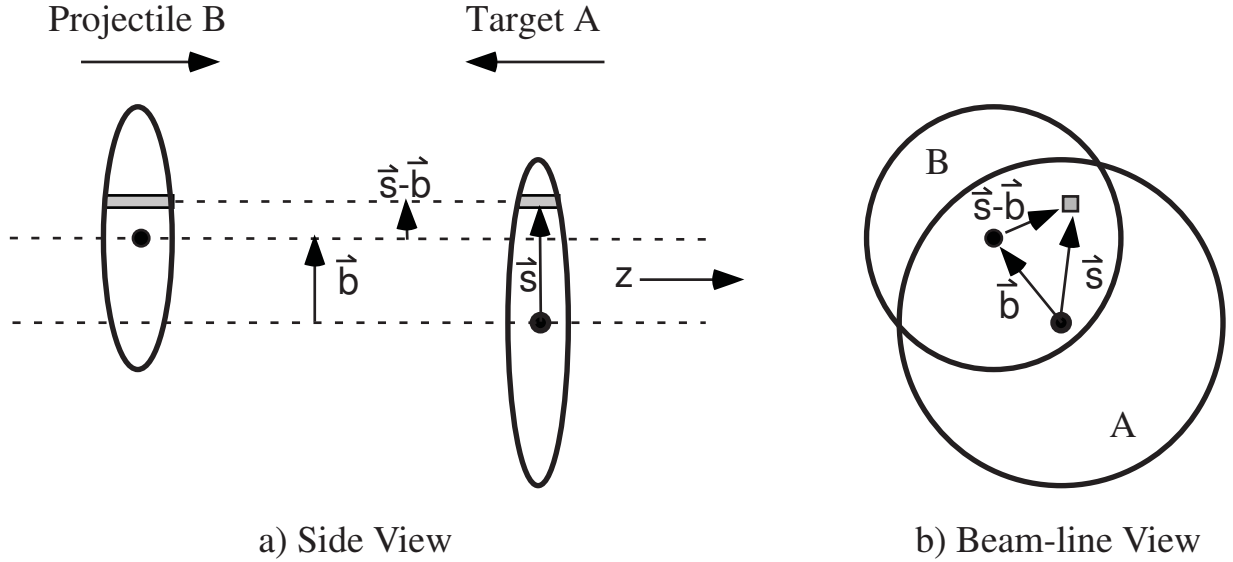


FIG. 5. Schematic representation of the Optical Glauber Model geometry, with transverse (a) and longitudinal (b) views. Figure taken from Ref. [86]

where $P(n, \mathbf{b})$ is the total probability of an interaction between nuclei A and B . For a given impact parameter, \mathbf{b} , the number of participants (or wounded nucleons) of nucleus A is given by

$$N_{\text{part}}^A(\mathbf{b}) = B \int T_B(\mathbf{s} - \mathbf{b}) \left\{ 1 - [1 - T_A(\mathbf{s}) \sigma_{\text{NN}}^{\text{inel}}]^A \right\} d^2s. \quad (4)$$

The number of participants in nucleus A is proportional to the nuclear profile function at transverse positions \mathbf{s} , $T_{AB}(\mathbf{s})$, weighted by the sum over the probability for a nucleon-nucleon collision at transverse position $(\mathbf{s} - \mathbf{b})$ in nucleus B . Thus at a given \mathbf{b} , the number of participants is given by

$$N_{\text{part}}(\mathbf{b}) = N_{\text{part}}^A(\mathbf{b}) + N_{\text{part}}^B(\mathbf{b}). \quad (5)$$

In heavy-ion physics, theoretical calculations use \mathbf{b} as an input to compare theoretical results to the experimental measurements. Both $N_{\text{part}}(\mathbf{b})$ and $N_{\text{coll}}(\mathbf{b})$ are calculated using Glauber model at a given \mathbf{b} , which are subsequently related to final state particle multiplicities [90].

In pp collisions, one cannot define impact parameter and centrality as they are point-like collisions of two nucleons. Thus, in experiments, the final state charged particle multiplicity is used to divide the event classes, which we discuss in more detail in the next subsection.

C. Charged-particle multiplicity (N_{ch})

One of the most fundamental observables to probe the system size of high-energy collisions is charged-particle multiplicity. In the ALICE experiment at the LHC, the charged-particle multiplicity is estimated at mid- and

forward-pseudorapidity regions. The charged-particle multiplicity at the mid-pseudorapidity region (*i.e.*, $|\eta| < 0.8$), denoted as $N_{\text{ch}}^{\text{mid}}$, is measured by the silicon pixel detector (SPD) and the time projection chamber (TPC). Contrary, the measurement of charged-particle multiplicity at the forward pseudorapidity region, denoted as $N_{\text{ch}}^{\text{fwd}}$, is performed by the V0 (V0A+V0C) detectors having the pseudorapidity coverage of $-3.7 < \eta < -1.7$ (V0C) and $2.8 < \eta < 5.1$ (V0A). The left and right panels of Fig. 6 show the self-normalised charged-particle multiplicity distributions obtained in mid and forward rapidity, respectively, at $\sqrt{s} = 13$ TeV using PYTHIA8. The distributions are further divided into different percentiles and specified as multiplicity classes.

Apart from the SPD, TPC, and V0 detectors discussed above, with the recent upgradation of ALICE in Run 3, the global detector named Fast Interaction Trigger (FIT) is used to estimate the collision centrality and the charged-particle multiplicity. FIT consists of three sub-detectors, namely, FT0, FV0, and FDD. The detailed description of the FIT detector can be found in Ref. [91]. The newly built Muon Forward Tracker (MFT) at forward rapidity ($-3.6 < \eta < -2.45$) can also be used to estimate the charged-particle multiplicity in Run 3 of ALICE [92]. Additionally, the CMS experiment at the LHC uses pairs of pixel clusters (known as tracklets) from two different layers (disks) of the silicon pixel detector to measure the charged-particle multiplicity produced in the range $|\eta| < 2.6$. These pairs have clusters with relatively small differences in η and ϕ . The correlation between η and ϕ can be used to select tracklets corresponding to primary charged hadrons. The detailed description of tracklets and vertex reconstruction algorithms can be found in Ref. [93–95]. The ATLAS experiment at the LHC uses tracking detectors such as the Inner Detector

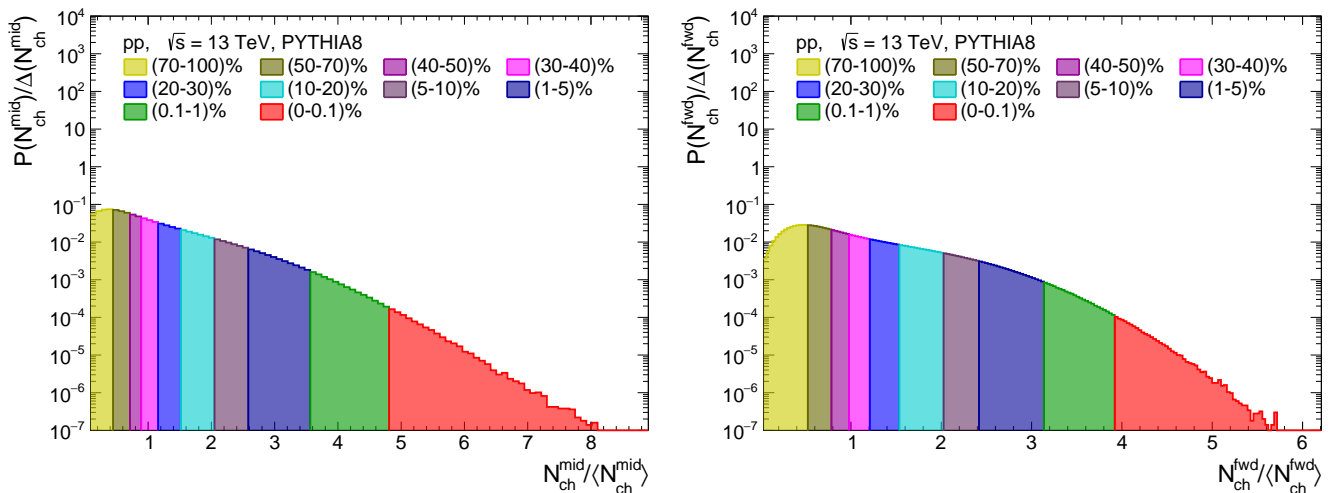


FIG. 6. Self-normalised Charged-particle multiplicity distributions measured in mid (left panel) and forward (right panel) rapidities at $\sqrt{s} = 13$ TeV using PYTHIA8.

(ID) and the trigger detectors to measure the charged-particle multiplicity. The ID consists of a silicon pixel detector (Pixel), a silicon microstrip detector (SCT), and a transition radiation tracker (TRT) with almost full coverage in ϕ , and $|\eta| < 2.5$. The detailed description of trigger selection and track reconstruction algorithms can be found in Ref. [96–98]. These three (ALICE, CMS, and ATLAS) are the major experiments at the LHC, and their measurement of final-state charged particle multiplicity as an event classifier is discussed.

D. Number of multi-partonic interactions (N_{mpi})

Hadronic collisions at RHIC and LHC produce a large number of particles in the final state. The fundamental description of particle production in hadronic collisions, such as pp , can be understood using the QCD-inspired parton model. [99]. In this model, the hadrons are treated as a collection of elementary constituents – quarks and gluons, collectively referred to as partons – bound together by the strong interaction. In minimum-bias hadronic collisions, multiple partonic interactions are inevitable due to the composite structure of hadrons [99, 100], with these MPIs typically being soft in nature. Additionally, in a hard pp collision, which is used for testing the Standard Model (SM) to high accuracy or sometimes to hunt for physics beyond the SM, a hard scattering is accompanied by a number of additional soft interactions, known as underlying event activity (UE). The comprehension and accurate modelling of these additional soft interactions are thus crucial for properly interpreting these hard interactions. Due to the non-perturbative nature, large numbers, and interplay among these interactions, the current approximation of these additional scattering can only be modelled in the

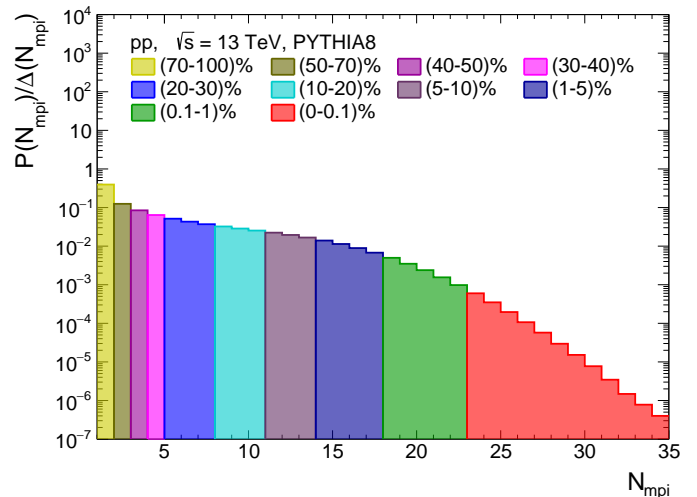


FIG. 7. Distribution of number of multi-partonic interactions (N_{mpi}) in pp collisions at $\sqrt{s} = 13$ TeV using PYTHIA8.

context of Monte Carlo (MC). Here, for an event with a fixed final state invariant mass, with the increase in the collision energy of the hadronic species, one can probe to a lower momentum fraction x , leading to a higher partonic flux and an increase in the multiple-partonic scattering cross-section [99, 100]. Consequently, events with a lower invariant mass in the final state can have influence from larger multiple hard scatterings [100]. In addition, most inelastic events in hadronic collisions contain several perturbatively calculable interactions when the pQCD theory is extended to the low- p_T regime with some distance above Λ_{QCD} [99]. Such interactions in inelastic hadronic collisions, even though soft and contributing to

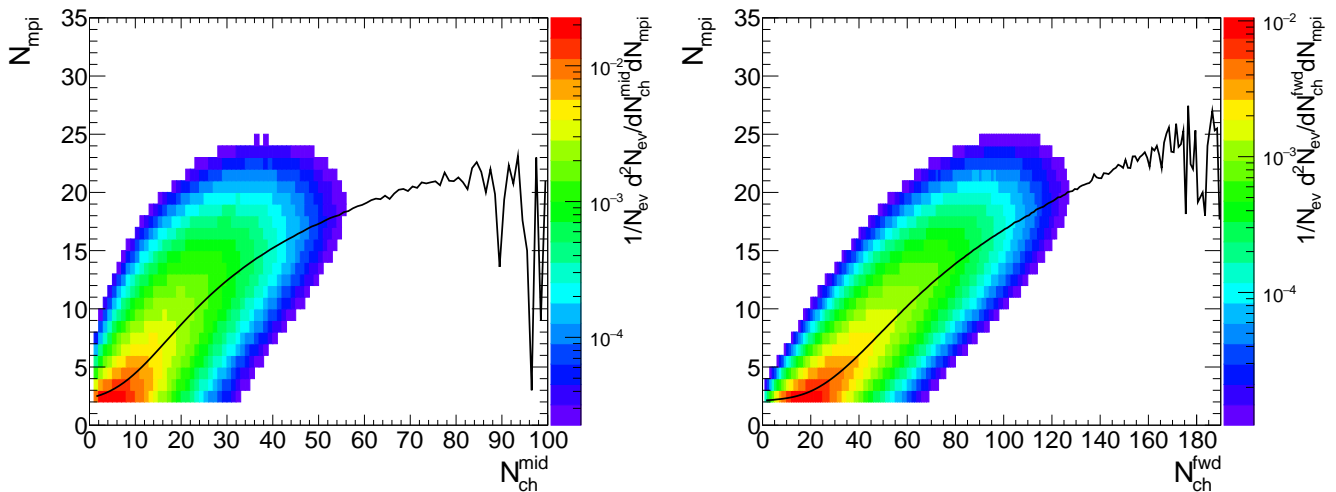


FIG. 8. Correlation of mid (left panel) and forward (right panel) rapidity charged-particle multiplicity with number of MPI in pp collisions at $\sqrt{s} = 13$ TeV using PYTHIA8.

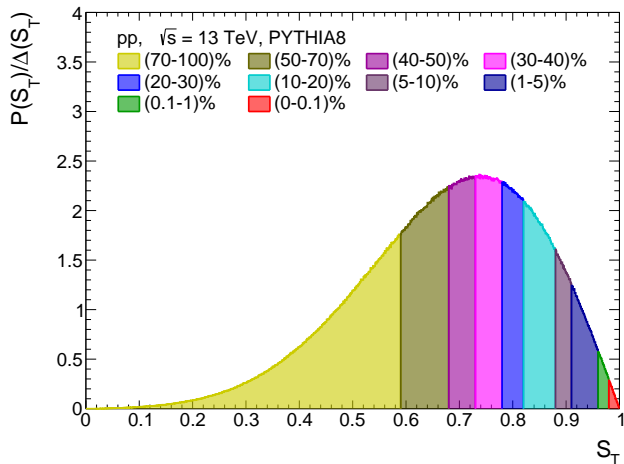


FIG. 9. Transverse sphericity distributions measured in pp collisions at $\sqrt{s} = 13$ TeV using PYTHIA8.

MPIs abundantly, are of much significance as they can significantly affect the particle multiplicity in the final state [99]. Thus, with an increase in the soft event activity, one expects the corresponding N_{mpi} to rise. In other words, an event with a large value of N_{mpi} is most likely to be a softer event.

At the LHC, recent measurements of heavy-ion-like signatures for high multiplicity pp collisions can be explained qualitatively with perturbative QCD-based event generators such as PYTHIA8 [19]. These heavy-ion-like features are well reproduced when one probes high MPIs with color reconnection. However, the estimation of N_{mpi} in experiments is difficult. Thus, one looks for event shape observables that can be proportional to N_{mpi} . This

makes the studies of the correlation of MPI with event-shape observables crucial in MC simulations. Figure 7 shows the distribution of N_{mpi} obtained in pp collisions at $\sqrt{s} = 13$ TeV using PYTHIA8. Different colour representations in the figure denote different percentile cuts of the distribution, specified as different multiplicity classes.

Figure 8 shows the correlation of mid-rapidity charged-particle multiplicity ($N_{\text{ch}}^{\text{mid}}$) (left panel) and forward rapidity charged-particle multiplicity ($N_{\text{ch}}^{\text{fwd}}$) (right panel) with the number of N_{mpi} in pp collisions at $\sqrt{s} = 13$ TeV using PYTHIA8. The solid line shows the mean value of N_{mpi} , i.e., $\langle N_{\text{mpi}} \rangle$, for a given multiplicity value on the x -axis. As one notices, both mid- and forward-charged-particle multiplicity retain a fair degree of correlation with N_{mpi} . From the figure, it is clear that irrespective of the pseudorapidity region, as the charged-particle multiplicity increases, the corresponding $\langle N_{\text{mpi}} \rangle$ also increases, indicating that the events having higher value of N_{mpi} tend to produce a large number of particles at the final state and are softer as compared to the events having lower N_{mpi} value. However, a saturation behavior of the correlation of N_{mpi} with $N_{\text{ch}}^{\text{mid}}$ is seen for higher values of $N_{\text{ch}}^{\text{mid}}$. This indicates that beyond $N_{\text{ch}}^{\text{mid}} \simeq 50$, the increase in multiplicity in the mid-rapidity region probes the events with similar N_{mpi} , i.e., $\simeq 20$. In addition, one notices that using $N_{\text{ch}}^{\text{fwd}}$ one can reach higher value of $\langle N_{\text{mpi}} \rangle$ as compared to the usage of $N_{\text{ch}}^{\text{mid}}$.

E. Transverse sphericity (S_T)

Transverse sphericity, one of the oldest event shape observables, was used at the Stanford Linear Accelerator Center (SLAC) to test the existence of jets in e^+e^- processes at collision energies up to 7.4 GeV [101]. Transverse sphericity is defined in terms of the eigenvalues of

the transverse momentum matrix (S_{xy}^Q), given as [44]:

$$S_{xy}^Q = \frac{1}{\sum_i p_{Ti}} \sum_i \begin{pmatrix} p_{xi}^2 & p_{xi}p_{yi} \\ p_{yi}p_{xi} & p_{yi}^2 \end{pmatrix} [\text{GeV}/c]. \quad (6)$$

Here, (p_{xi}, p_{yi}) are the projections of transverse momentum (p_{Ti}) of i th particle in (x, y) directions and i runs over all the charged hadrons. Q denotes the quadrature property of the particle momenta, which makes the transverse momentum matrix in Eq. 6, S_{xy}^Q is non-collinear safe. To make it collinear-safe, Eq. 6 can be linearized as follows,

$$S_{xy}^L = \frac{1}{\sum_i p_{Ti}} \sum_i \frac{1}{p_{Ti}} \begin{pmatrix} p_{xi}^2 & p_{xi}p_{yi} \\ p_{yi}p_{xi} & p_{yi}^2 \end{pmatrix} \quad (7)$$

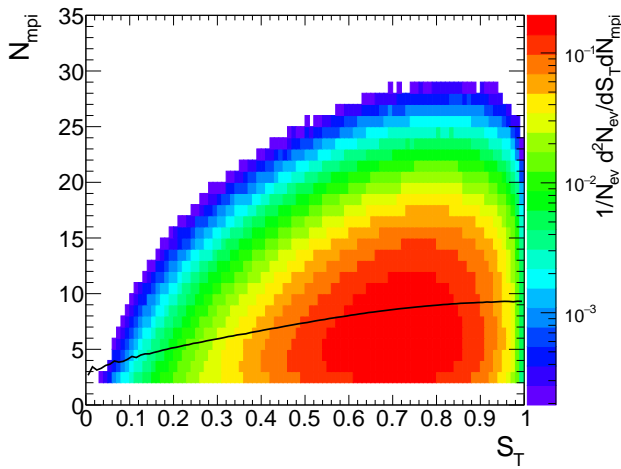


FIG. 10. Correlation of S_T with number of MPI.

Transverse sphericity can be defined in terms of the eigenvalues, λ_1 , and λ_2 of the linearized transverse momentum matrix S_{xy}^L such that $\lambda_1 > \lambda_2$, and defined as follows.

$$S_T = \frac{2\lambda_2}{\lambda_1 + \lambda_2} \quad (8)$$

By construction, the value of S_T lie between 0 and 1. Here, the extreme limits, i.e., $S_T \rightarrow 0$ selects the jetty or pencil-like events, while $S_T \rightarrow 1$ indicates that the events are isotropic, which are dominated by the soft production of particles. In this work, S_T has been estimated with the charged particles in the mid-pseudorapidity region, i.e., $|\eta| < 0.8$ having $p_T > 0.15$ GeV/c. Figure 9 shows the distribution of transverse sphericity measured in pp collisions at $\sqrt{s} = 13$ TeV using PYTHIA8. In addition, different percentile slices are shown in the S_T distribution, referred to as sphericity classes, which are shown with different colours. Figure 10 shows the corre-

lation of transverse sphericity with the number of multipartonic interactions in pp collisions at $\sqrt{s} = 13$ TeV using PYTHIA8, where the solid line shows the mean value of N_{mpi} for each bin in S_T . From Fig. 10, it is clear that the transverse sphericity possesses a finite positive correlation with the number of multi-partonic interactions.

F. Transverse sphericity (S_0)

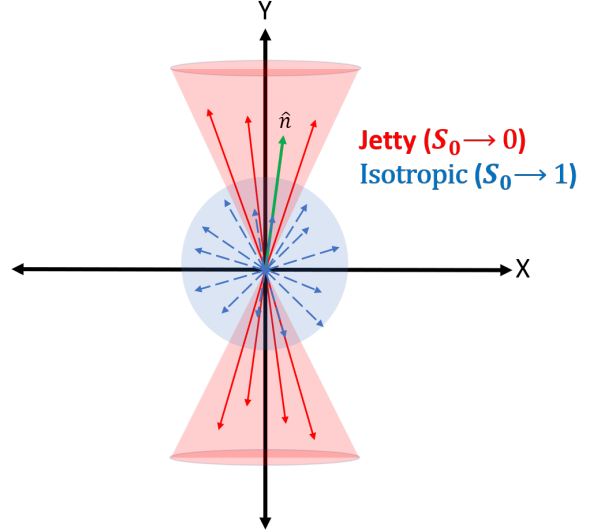


FIG. 11. Depiction of isotropic and jetty events based on the transverse sphericity selection [58].

Similar to transverse sphericity, transverse sphericity is another event shape observable extensively used at the LHC energies to separate the soft versus hard QCD-dominated events. Transverse sphericity is defined for a unit vector $\hat{n}(n_T, 0)$ in the transverse plane, which follows a minimization criterion as shown in the following equation [58, 102–104]

$$S_0 = \frac{\pi^2}{4} \min_{\hat{n}} \left(\frac{\sum_{i=1}^{N_{\text{had}}} |\vec{p}_{Ti} \times \hat{n}|}{\sum_{i=1}^{N_{\text{had}}} |\vec{p}_{Ti}|} \right)^2 \quad (9)$$

As previously mentioned, along with the transverse sphericity, most of the discussed observables are infrared and collinear safe quantities. In the next subsections, we discuss the collinear and infrared safety for transverse sphericity as an example.

1. Infrared Safety

In particle physics, infrared refers to the limit of the low-energy (large-wavelength) quanta, i.e., soft photons in QED and soft gluons in QCD. In high-energy collider experiments, soft gluons are frequently produced through

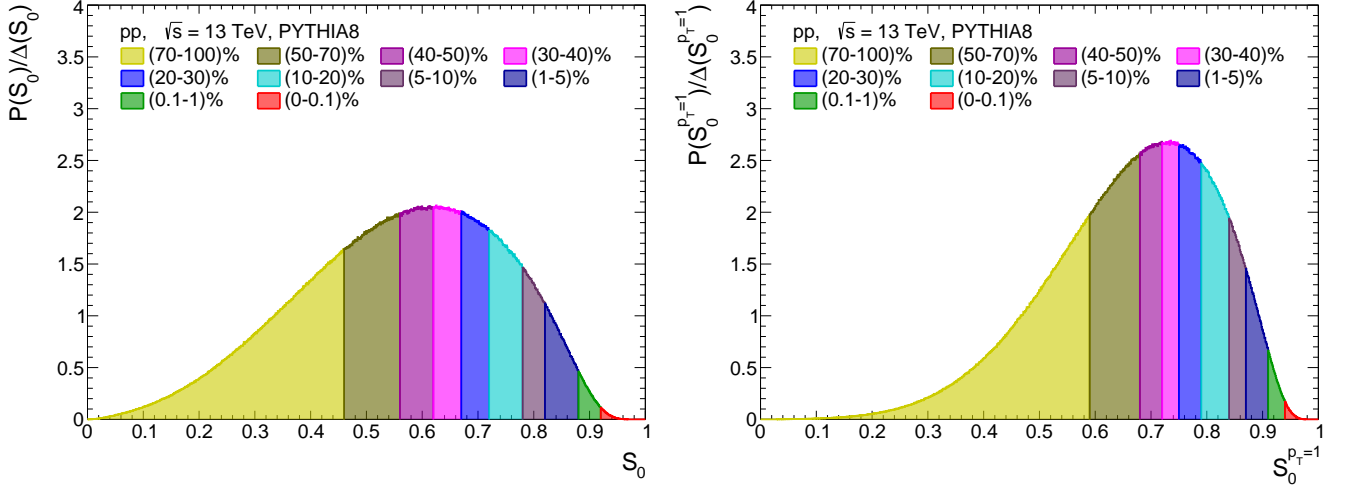


FIG. 12. Weighted and unweighted transverse sphericity distributions measured in pp collisions at $\sqrt{s} = 13$ TeV using PYTHIA8.

parton radiation and showering. These gluons subsequently hadronise, giving rise to soft (low- p_T) hadrons in the final state. The invariance of a quantity in the presence of these soft hadrons is called infrared safety.

Let us consider a soft hadron with transverse momentum \vec{p}_{T_s} is emitted along with other hadrons such that $|\vec{p}_{T_s}| = \varepsilon \rightarrow 0$. Here, the subscript ‘s’ stands for soft. New value of transverse sphericity modifies to:

$$S'_0 = \frac{\pi^2}{4} \min_{\hat{n}} \left(\frac{\sum_{i=1}^{N_{\text{had}}} |\vec{p}_{T_i} \times \hat{n}| + |\vec{p}_{T_s} \times \hat{n}|}{\sum_{i=1}^{N_{\text{had}}} |\vec{p}_{T_i}| + |\vec{p}_{T_s}|} \right)^2. \quad (10)$$

If the angle between \vec{p}_{T_s} and \hat{n} is θ_s , then the above equation can be re-written as:

$$S'_0 = \frac{\pi^2}{4} \min_{\hat{n}} \left(\frac{\sum_{i=1}^{N_{\text{had}}} |\vec{p}_{T_i} \times \hat{n}| + \varepsilon \sin \theta_s}{\sum_{i=1}^{N_{\text{had}}} |\vec{p}_{T_i}| + \varepsilon} \right)^2. \quad (11)$$

In the infrared limit, i.e., $\varepsilon \rightarrow 0$, Eq. (11) modifies to:

$$S'_0 = \frac{\pi^2}{4} \min_{\hat{n}} \left(\frac{\sum_{i=1}^{N_{\text{had}}} |\vec{p}_{T_i} \times \hat{n}|}{\sum_{i=1}^{N_{\text{had}}} |\vec{p}_{T_i}|} \right)^2 = S_0. \quad (12)$$

Thus, a soft (infrared) emission of particles renders transverse sphericity unchanged, making it infrared safe.

2. Collinear Safety

Let us consider a hadron with transverse momentum p_{T_k} splits into two collinear particles with transverse momenta $p_{T_{k1}}$ and $p_{T_{k2}}$, such that:

$$p_{T_{k1}} = z p_{T_k} \quad \text{and} \quad p_{T_{k2}} = (1-z) p_{T_k}. \quad (13)$$

Here, z and $(1-z)$ stand for the fractions of the momentum of the hadron in a collinear splitting and $0 < z < 1$ and \vec{p}_{T_k} , $\vec{p}_{T_{k1}}$, and $\vec{p}_{T_{k2}}$ are parallel to each other. For any direction of \hat{n} ,

$$|\vec{p}_{T_{k1}} \times \hat{n}| + |\vec{p}_{T_{k2}} \times \hat{n}| = z |\vec{p}_{T_k} \times \hat{n}| + (1-z) |\vec{p}_{T_k} \times \hat{n}| = |\vec{p}_{T_k} \times \hat{n}|. \quad (14)$$

Thus, a collinear splitting of a particle keeps the numerator of Eq. (9) unchanged. Similarly, one can show for the denominator as follows.

$$|\vec{p}_{T_{k1}}| + |\vec{p}_{T_{k2}}| = z |\vec{p}_{T_k}| + (1-z) |\vec{p}_{T_k}| = |\vec{p}_{T_k}|. \quad (15)$$

The contribution of the original particle is the same as the sum of the collinear fragments in both the numerator and denominator of Eq. (9). Hence, transverse sphericity remains unchanged for a collinear fragmentation of a particle, which makes it collinear safe.

S_0 is usually calculated using charged-particle tracks that lie in the mid-pseudorapidity ($|\eta| < 0.8$) region and possess $p_T > 0.15$ GeV/c. To ensure a statistically meaningful concept of a topology, transverse sphericity is calculated for the events having more than 10 charged-particle tracks in the kinematic region mentioned above. These events are often referred to as S_0 -integrated events. In Eq. (9), N_{had} is the total number of charged hadrons in the event, and the multiplication of $\pi^2/4$ ensures S_0 to lie between 0 and 1. The two extreme limits of sphericity correspond to the two different configurations of event topology. Events with $S_0 \rightarrow 0$ consist of single back-to-back jets, while events with $S_0 \rightarrow 1$ are isotropic particle production dominated events. The different limits are depicted in Fig. 11. Usually in experimental measurements, the events located in the bottom 20% of the S_0 distribution are referred to as jetty events, while the top 20% of the S_0 distribution are referred to as isotropic

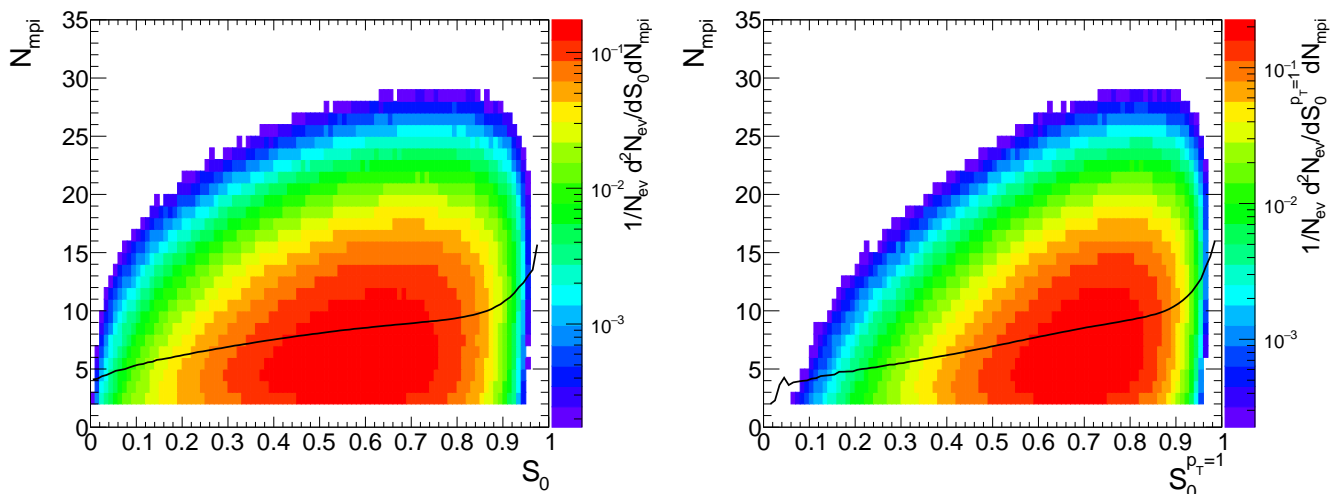


FIG. 13. Correlation of S_0 (left panel) and $S_0^{p_T=1}$ (right panel) with number of MPI in pp collisions at $\sqrt{s} = 13$ TeV using PYTHIA8.

events.

It is worth emphasizing that Eq. (9) is p_T weighted and introduces neutral jet bias. This jet bias can be fixed by setting the $p_T = 1$ for all the charged tracks in Eq. (9). Thus, one can write unweighted transverse sphericity ($S_0^{p_T=1}$) as follows.

$$S_0^{p_T=1} = \frac{\pi^2}{4} \min_{\hat{n}} \left(\frac{\sum_{i=1}^{N_{\text{had}}} |\hat{p}_T \times \hat{n}|}{N_{\text{had}}} \right)^2. \quad (16)$$

As the biases towards high- p_T particles in Eq. (16) is removed by setting $p_T = 1$, the denominator in Eq. (9), i.e., $\sum_i p_{T_i}$ is now replaced by the number of charged hadrons, i.e., N_{had} .

Figure 12 shows the distribution of weighted transverse sphericity (S_0) (left) and unweighted transverse sphericity ($S_0^{p_T=1}$) (right) for minimum bias pp collisions at $\sqrt{s} = 13$ TeV using PYTHIA8. The transverse sphericity distributions are further divided into different percentiles and specified as different transverse sphericity classes. Figure 13 shows the correlation of weighted (S_0) (left panel) and unweighted ($S_0^{p_T=1}$) (right panel) transverse sphericity with N_{mpi} . The solid line guides the mean values of N_{mpi} , i.e., $\langle N_{\text{mpi}} \rangle$, for each bin on the x -axis. The measurements shown in Fig. 13 are performed in pp collisions at $\sqrt{s} = 13$ TeV using PYTHIA8. From Fig. 13, it is conclusive that both S_0 , and $S_0^{p_T=1}$ retains a fair degree of correlation with N_{mpi} , where the higher values of S_0 , and $S_0^{p_T=1}$ corresponds to a large number of multi-partonic interactions, i.e., soft events. When compared to Fig. 10, the correlation of S_T with N_{mpi} appears to be smaller in magnitude as compared to the correlation of transverse sphericity and charged-particle multiplicity with N_{mpi} , especially for extreme

isotropic events.

Figure 14 shows the correlation of S_0 and $S_0^{p_T=1}$ with N_{mpi} . A similar correlation of S_0 and $S_0^{p_T=1}$ with N_{mpi} is also shown for the highest (0-1)% multiplicity class in the mid and forward pseudorapidity regions. Both S_0 and $S_0^{p_T=1}$ possess a fair degree of positive correlation with N_{mpi} , where events having sphericity value close to one have higher $\langle N_{\text{mpi}} \rangle$ value. When no multiplicity selection is applied, S_0 probes higher values of $\langle N_{\text{mpi}} \rangle$ as compared to $S_0^{p_T=1}$ in the intermediate values of sphericity. The difference of $\langle N_{\text{mpi}} \rangle$ for both weighted and unweighted transverse sphericity for the minimum bias case starts to vanish as one goes close to their extreme values, i.e., 0 and 1. In addition, by applying charged-particle event selection, the transverse sphericity achieves a higher value of $\langle N_{\text{mpi}} \rangle$. For the top 1% multiplicity class based on both $N_{\text{ch}}^{\text{mid}}$ and $N_{\text{ch}}^{\text{fwd}}$ we observe that S_0 probes a higher value of N_{mpi} than $S_0^{p_T=1}$ towards lower values of sphericity. As the value of sphericity approaches '1', $\langle N_{\text{mpi}} \rangle$ from both $S_0^{p_T=1}$ and S_0 approach each other and the difference in $\langle N_{\text{mpi}} \rangle$ vanishes for $S_0 \gtrsim 0.8$. Furthermore, both weighted and unweighted values of transverse sphericity for (0-1)% $N_{\text{ch}}^{\text{mid}}$ class acquired a higher value of $\langle N_{\text{mpi}} \rangle$ and a lower slope, relative to (0-1)% $N_{\text{ch}}^{\text{fwd}}$ class. The lower slope of S_0 and $S_0^{p_T=1}$ vs $\langle N_{\text{mpi}} \rangle$ for the (0-1)% class of $N_{\text{ch}}^{\text{mid}}$, may arise due to estimation of both sphericity and $N_{\text{ch}}^{\text{mid}}$ in the similar pseudorapidity region.

G. Relative transverse activity classifier (R_T)

In relativistic collisions, the partonic interactions are characterized by pQCD or non-pQCD processes. Initial hard scattering in such collisions is a pQCD process due to the large energy and momentum transfers involved

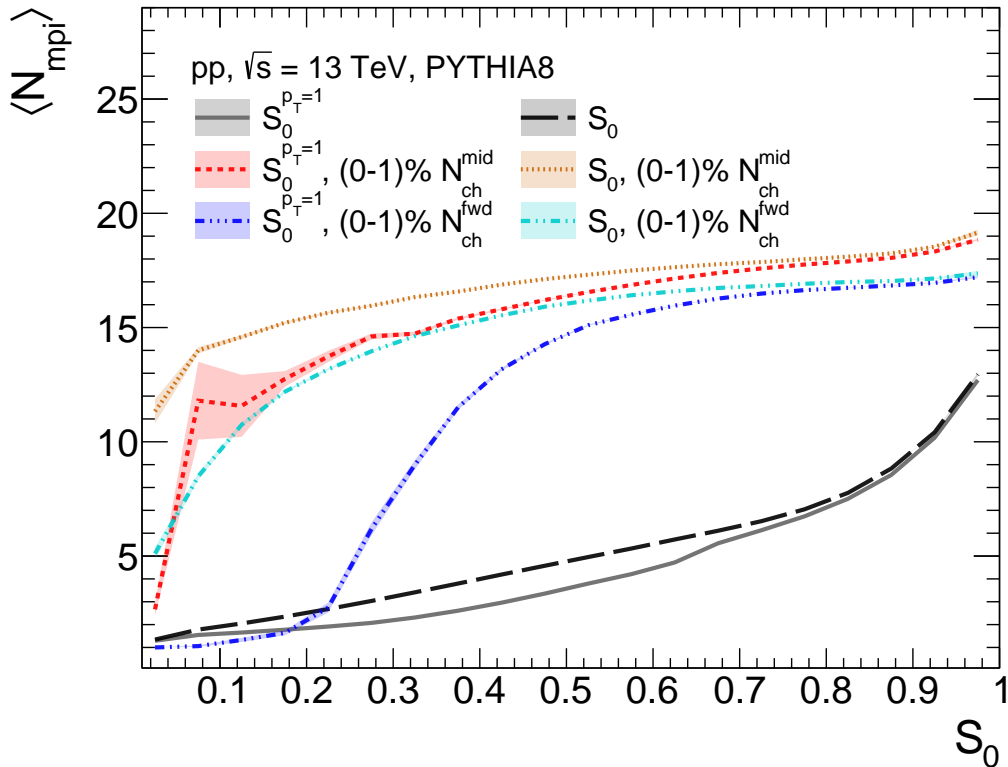


FIG. 14. Correlation of S_0 and $S_0^{p_T=1}$ with average number of MPI in minimum bias and high-multiplicity pp collisions at $\sqrt{s} = 13$ TeV using PYTHIA8.

in such collisions. On the other hand, multi-partonic interactions, initial and final state radiations, and beam remnants are non-pQCD in nature. The partons involved in the multi-partonic interactions, initial and final state radiations, and the beam remnant collectively contribute to the underlying event. The particles contributing to UE do not originate from the fragmentation of partons produced in the hardest scattering. Underlying event (UE) activity is one of the efficient tools theorised to affect particle production and can lead to observed QGP-like signatures in pp collisions.

To classify the events based on the contribution from the UE events, one can define different topological regions based on the contribution from the jet fragmentation and the UE. Figure 15 depicts different topological regions, *viz.*, toward, transverse and away, defined with respect to the highest p_T particle, also called the leading particle, and the corresponding momentum is p_T^{leading} . The toward region, as the name indicates, consists of the particles with an azimuthal angle less than $\pi/3$ relative to the leading particle, *i.e.*, $|\Delta\phi| < \pi/3$ and has the largest contribution from the fragmentation of jets. The away region contains all the charged particles with $|\Delta\phi| \geq 2\pi/3$ while the transverse region is defined to be within $\pi/3 \leq |\Delta\phi| < 2\pi/3$. Since the transverse region is perpendicular to the leading jet axis, it is expected to

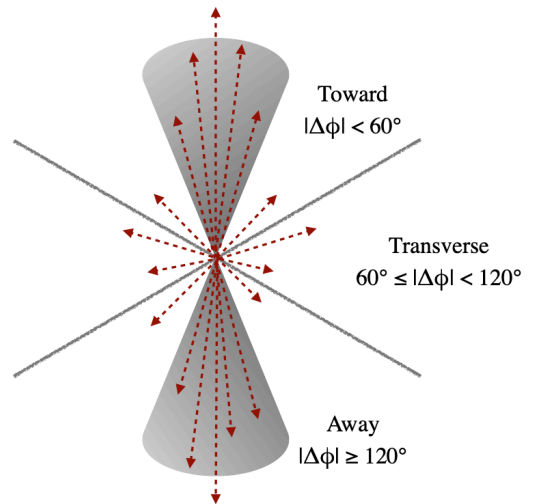


FIG. 15. Depiction of different topological regions with respect to the trigger jet particle.

have the least contribution from the jet and must be dominated by the underlying event activity. To estimate the value of the relative transverse activity classifier (R_T),

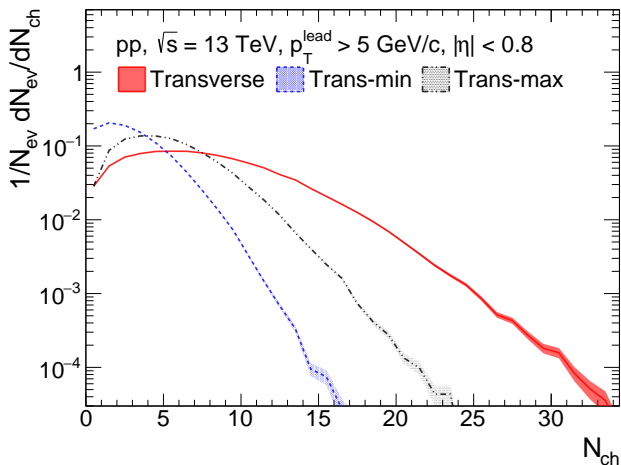


FIG. 16. N_{ch} distributions for transverse, trans-min and trans-max regions

the number of charged hadrons in the transverse regions is determined, denoted as $N_{\text{ch}}^{\text{trans}}$. Thus, one obtains the value of R_T using the following expression.

$$R_T = \frac{N_{\text{ch}}^{\text{T}}}{\langle N_{\text{ch}}^{\text{T}} \rangle} \quad (17)$$

Similarly, for R_T^{min} , and R_T^{max} , the transverse region is again subdivided into $\pi/3 < \Delta\phi < 2\pi/3$ and $-\pi/3 > \Delta\phi > -2\pi/3$. The charged-particle multiplicity in these two regions is determined. For each event, the region with higher multiplicity (trans-max) contributes to $N_{\text{ch}}^{\text{T-max}}$ while the region with less multiplicity (trans-min) contributes to $N_{\text{ch}}^{\text{T-min}}$. Thus, one obtains, R_T^{min} and R_T^{max} as follows [41].

$$R_T^{\text{min}} = \frac{N_{\text{ch}}^{\text{T-min}}}{\langle N_{\text{ch}}^{\text{T-min}} \rangle} \quad (18)$$

$$R_T^{\text{max}} = \frac{N_{\text{ch}}^{\text{T-max}}}{\langle N_{\text{ch}}^{\text{T-max}} \rangle} \quad (19)$$

In Equations (17), (18), and (19), the angular brackets represent the event-average value of the observables. Figure 16 shows the distribution of charged-particle yields in the transverse (N_{ch}^{T}), trans-min ($N_{\text{ch}}^{\text{T-min}}$), and trans-max ($N_{\text{ch}}^{\text{T-max}}$) regions. The charged hadrons are measured in the mid-pseudorapidity region, i.e., $|\eta| < 0.8$, with $p_T^{\text{lead}} > 5$ GeV/c in pp collisions at $\sqrt{s} = 13$ TeV using PYTHIA8. As expected, in Fig. 16, trans-min region has the lowest multiplicity yield, followed by trans-max. It is important to note that $N_{\text{ch}}^{\text{T}} = N_{\text{ch}}^{\text{T-min}} + N_{\text{ch}}^{\text{T-max}}$, which is also held by the distribution shown in Fig. 16.

Figure 17 shows the distribution of R_T (upper left), R_T^{min} (upper right) and R_T^{max} (lower) in pp collisions at $\sqrt{s} = 13$ TeV, and corresponding percentile slices.

In Fig. 18, we show the correlation of R_T (upper left), R_T^{min} (upper right), and R_T^{max} (lower) with N_{mpi} . Here, the solid line represents the mean values of N_{mpi} for the corresponding bin in the x -axis. The measurements shown in Fig. 18 are performed in pp collisions at $\sqrt{s} = 13$ TeV using PYTHIA8. All the classifiers, R_T , R_T^{max} , and R_T^{min} show a fair amount of correlations with N_{mpi} . The correlation shown in Fig. 18 is significantly larger as compared to the correlation of transverse sphericity and transverse sphericity with N_{mpi} . In other words, using the relative transverse activity classifiers, one can probe to higher values of N_{mpi} compared to S_0 , $S_0^{p_T=1}$, and S_T .

H. Charged-particle flattenicity (ρ_{ch})

Isotropic events are expected to have a uniform distribution of p_T throughout the $(\eta - \phi)$ region. To quantify the uniformity of p_T distribution event-by-event, the $(\eta - \phi)$ region is divided into a (10×10) grid. p_T in each cell (p_T^{cell}) can be measured, and corresponding mean ($\langle p_T^{\text{cell}} \rangle$) and standard deviation ($\sigma_{p_T^{\text{cell}}}$) can be estimated. Keeping the ALICE3 tracking capabilities in mind, the charged particles in $|\eta| < 4.0$ and $p_T > 0.15$ GeV/c are considered for the estimation of $\langle p_T^{\text{cell}} \rangle$ and $\sigma_{p_T^{\text{cell}}}$. Thus, for an event, flattenicity (ρ) is defined as the relative standard deviation as follows [105],

$$\rho_{\text{ch}} = \frac{\sigma_{p_T^{\text{cell}}}}{\langle p_T^{\text{cell}} \rangle} \quad (20)$$

Events with both jet signals and underlying event activity are expected to have a larger spread, and correspondingly, $\sigma_{p_T^{\text{cell}}}$ will be higher. In contrast, events having only soft production of particles will have a narrower distribution of p_T^{cell} , and therefore corresponding $\sigma_{p_T^{\text{cell}}}$ will be smaller. It is important to note that the presence of jet signals in the jetty events can also enhance $\langle p_T^{\text{cell}} \rangle$ in the denominator of Eq. (20); however, the increase in $\langle p_T^{\text{cell}} \rangle$ will be overshadowed by the corresponding rise in $\sigma_{p_T^{\text{cell}}}$ in the numerator. Thus, the value of ρ is expected to be smaller for isotropic events, while a large value of $\sigma_{p_T^{\text{cell}}}$ corresponds to a jetty event.

However, the current PID and tracking capabilities at ALICE (LHC) and the STAR experiment (RHIC) are limited to $|\eta| < 1.0$. As a result, using the above definition, one can not estimate the value of ρ at these experiments. Moreover, the measurement of both the event shape and the particle of interest in the same pseudorapidity region induces a bias. The bias can be mitigated by choosing the event shape estimator in the forward rapidity region, which ensures it is in a different pseudorapidity region compared to the particle of interest. Most of the present detectors can measure particle multiplicity in the forward rapidity. Thus, a redefinition of

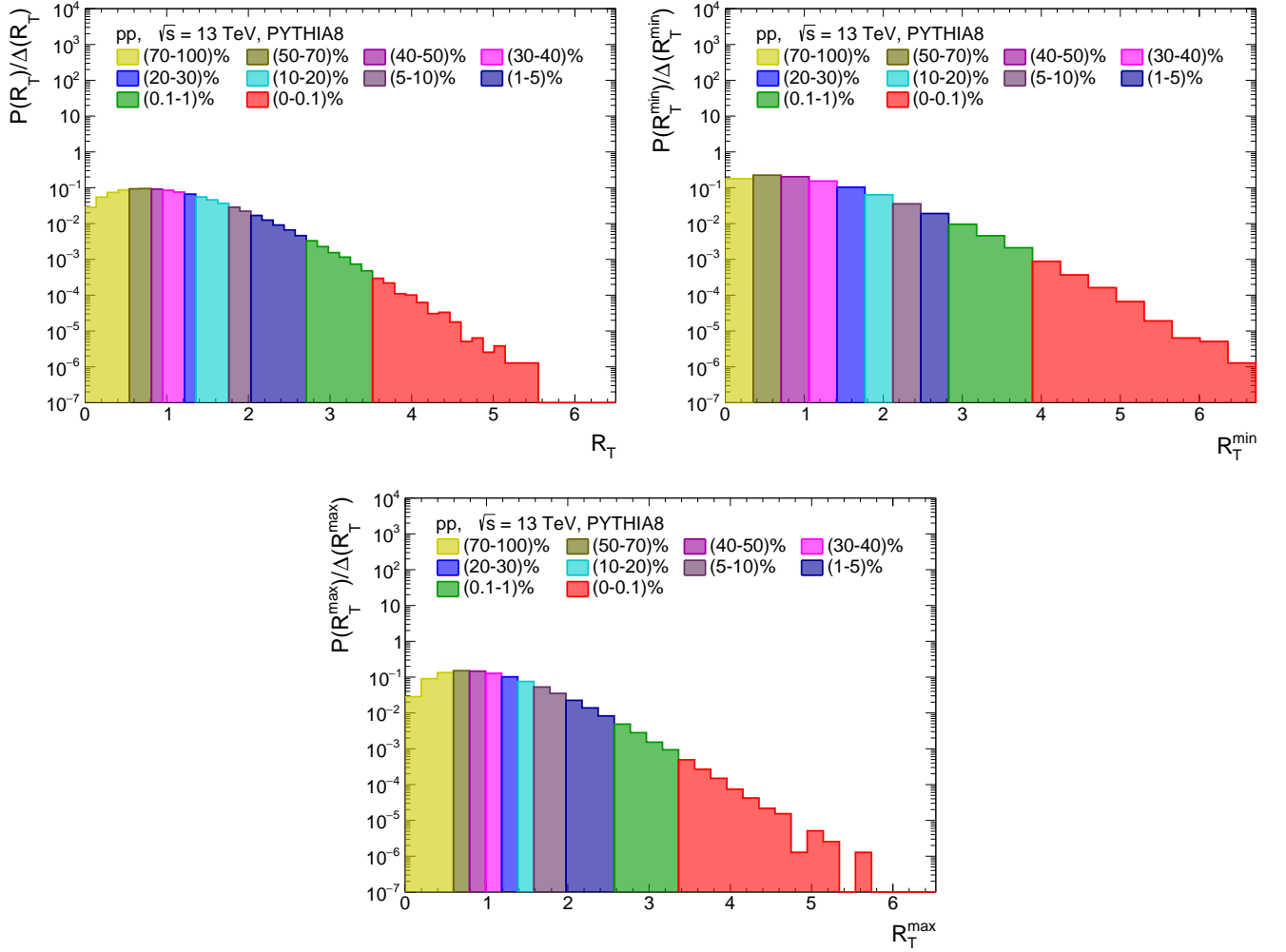


FIG. 17. Distribution of R_T measured in the transverse, trans-min and trans-max regions in pp collisions at $\sqrt{s} = 13$ TeV using PYTHIA8.

flattening is necessary to account for the issues mentioned above, which would consider the charged-particle multiplicity in each cell at the forward rapidity instead of p_T^{cell} . Flattening (ρ_{ch}) is determined in the forward-rapidity region, where the $(\eta - \phi)$ space is divided into (8×8) cells and charged particles in each cell ' i ' ($N_{\text{ch}}^{\text{cell},i}$) is estimated. Thus, ρ_{ch} can be estimated using the following equation [106].

$$\rho_{\text{ch}} = \frac{\sqrt{\sum_i (N_{\text{ch}}^{\text{cell},i} - \langle N_{\text{ch}}^{\text{cell}} \rangle)^2 / N_{\text{cell}}^2}}{\langle N_{\text{ch}}^{\text{cell}} \rangle} \quad (21)$$

Here, $\langle N_{\text{ch}}^{\text{cell}} \rangle$ is the mean number of charged particles in the cells. By construction, ρ_{ch} ranges from 0 to 1, where the lower limit, $\rho_{\text{ch}} \rightarrow 0$ indicates isotropic events and $\rho_{\text{ch}} \rightarrow 1$ indicates jetty events. To be consistent with other event-shape observables, here, throughout the manuscript, we use $(1 - \rho_{\text{ch}})$ instead of ρ_{ch} , where events

with $(1 - \rho_{\text{ch}}) \rightarrow 1$ are likely to be isotropic while $(1 - \rho_{\text{ch}}) \rightarrow 0$ indicates to a jetty event.

Figure 20 shows the correlation of charged-particle flattening, $(1 - \rho_{\text{ch}})$, with N_{mpi} . ρ_{ch} is measured using the charged particles having $p_T > 0$ the V0 acceptance region of ALICE, i.e., $-3.7 < \eta < -1.7$ and $2.8 < \eta < 5.1$, where $(\eta - \phi)$ space is divided into a (8×8) grid. The correlation of $(1 - \rho_{\text{ch}})$ with N_{mpi} remains almost flat at 0 till $(1 - \rho_{\text{ch}}) < 0.6$, then starts to rise rapidly, where most of the events lie.

It is noteworthy to mention that the charged-particle flattening distribution depends on the detector acceptance range from which the charged-particle multiplicity is measured. In this review, we discuss the flattening distribution that is obtained by using the multiplicity from the V0M acceptance. In Run 3, a preliminary study has been performed using the FV0A detector to study the flattening dependence of strangeness production [107]. However, in the future, it would be interesting to in-

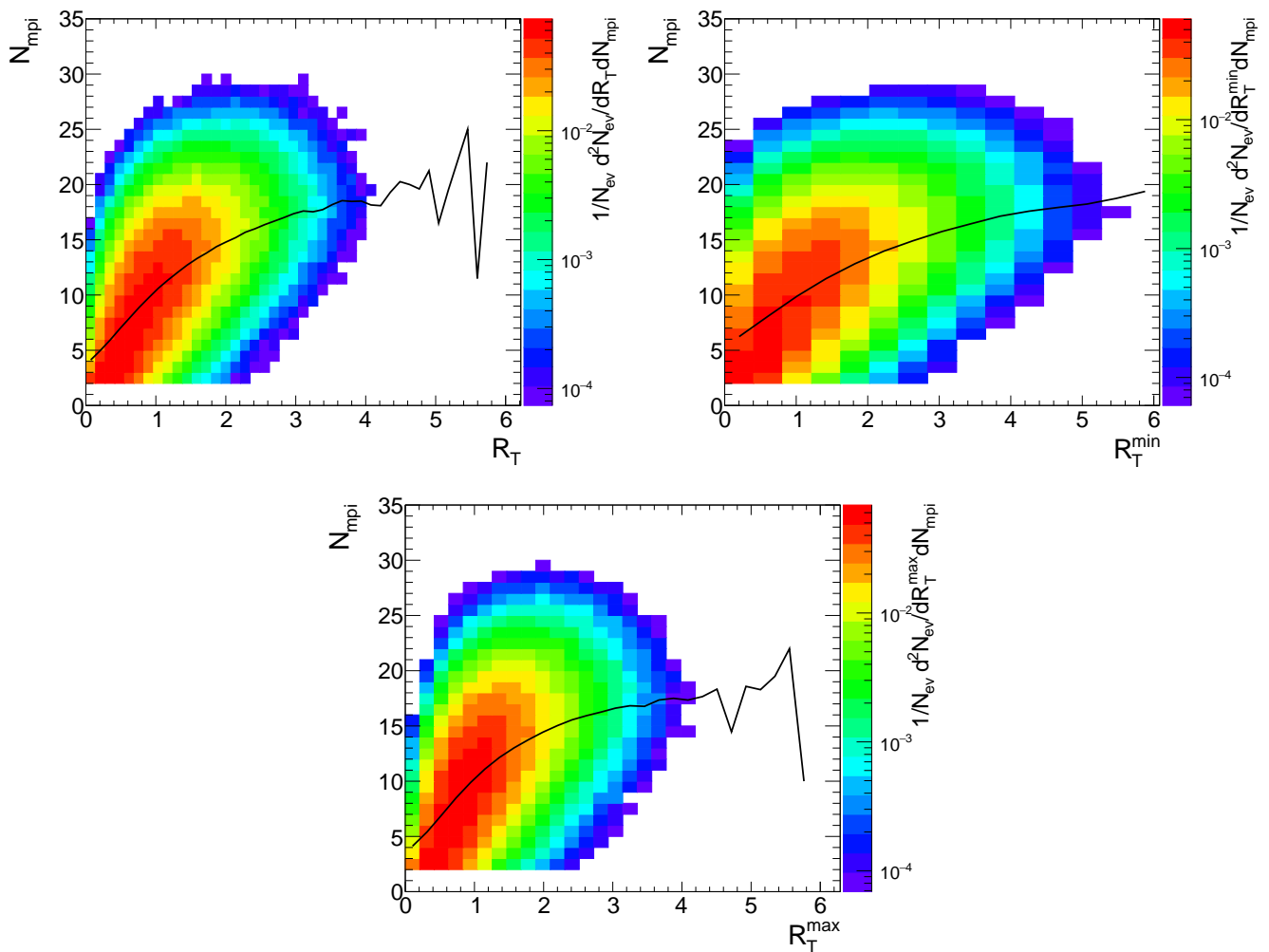


FIG. 18. Correlation of R_T measured in the transverse, trans-min and trans-max regions with number of MPI in pp collisions at $\sqrt{s} = 13$ TeV using PYTHIA8.

investigate charged-particle flattenicity distribution and the studied observables as a function of charged-particle flattenicity, considering the charged-particle multiplicity from the newly built FTOM and MFT forward detectors of ALICE in Run 3. It is worth mentioning that, to make the studies coherent and detector/experiment independent, one needs to employ an unfolding procedure to retrieve a true flattenicity distribution from the folded distributions with the detector effects.

I. Flow vectors (q_n)

In heavy-ion collisions, the initial configuration of the collision overlap region can affect the final state azimuthal distribution of charged particles. In non-central collisions, the collision overlap region is elliptic in the transverse plane, and thus, the final state azimuthal distributions of particles are elliptic, leading to a larger

value of elliptic flow in the mid-central collisions as compared to the most-central collisions. Further, the density fluctuations can lead to observations of higher-order flow coefficients. Interestingly, one can make classifications of events based on the azimuthal distribution of particles in the final state using the reduced flow vectors (q_n), defined as follows [38, 108]:

$$q_n = \frac{|Q_n|}{\sqrt{M}}, \quad (22)$$

where

$$Q_n = \sum_{j=1}^M e^{in\phi_j}. \quad (23)$$

Here, M is the total number of charged hadrons, and ϕ_j is the azimuthal angle of the j th hadron. n denotes the order of the reduced flow vectors. Here, q_2 can separate

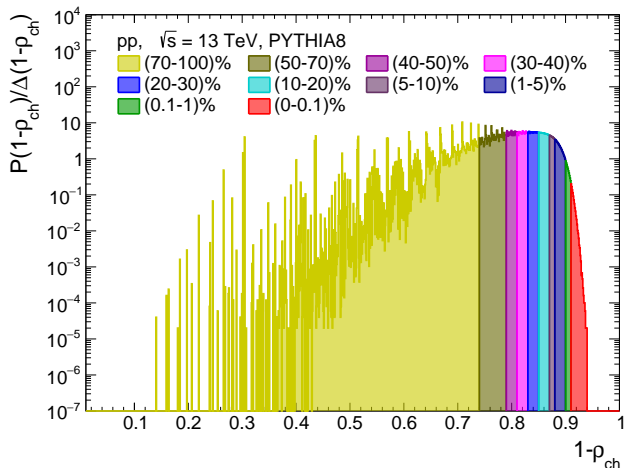


FIG. 19. charged-particle flattenicity distributions measured in pp collisions at $\sqrt{s} = 13$ TeV using PYTHIA8.

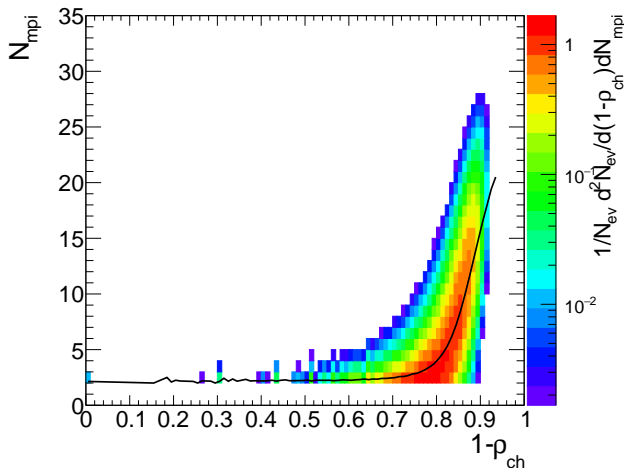


FIG. 20. Correlation of flattenicity with number of MPI

events based on the elliptic distribution of the hadrons in the transverse plane. Similarly, q_3 isolates events based on the triangular distribution of the hadrons in the transverse plane. For $M \rightarrow \infty$, the reduced flow vectors are proportional to anisotropic flow coefficients of similar order [108]. However, this proportionality becomes weaker as M is reduced [108]. Thus, q_n are not good observables for the low multiplicity events [108].

J. Aplanarity (A)

Aplanarity is another interesting event shape observable that characterizes the shape of the underlying event (UE) based on the momentum of the charged hadrons. Aplanarity is estimated from the linearized sphericity

tensor $S^{\mu\nu}$, and defined as [44, 101, 109];

$$S^{\mu\nu} = \frac{\sum_{i=1}^{N_{\text{ch}}} p_i^\mu p_i^\nu / |p_i|}{\sum_{i=1}^{N_{\text{ch}}} |p_i|}. \quad (24)$$

Here, the index i runs over all the charged hadrons in a given event. μ and ν indices refer to one of the (x, y, z) components of the momentum of a particle. The individual eigenvalues $\lambda_1, \lambda_2, \lambda_3$ of the momentum tensor $S^{\mu\nu}$ are normalized and ordered such that $\lambda_1 > \lambda_2 > \lambda_3$ and by definition $\lambda_1 + \lambda_2 + \lambda_3 = 1$. Using these eigenvalues, one can construct various event shape observables such that;

- **Aplanarity:** $A = \frac{3}{2}\lambda_3$ measures the amount of transverse momentum in or out of the plane formed by the two leading order eigenvectors, λ_1 and λ_2 . Theoretically, A lies between $0 \leq A < 1/2$; however, the typical measured values fall between $0 \leq A < 0.3$. The value of A close to zero indicates a relatively planar event, while $A \rightarrow 1/2$ indicates the isotropic events.
- **Sphericity:** $S = \frac{3}{2}(\lambda_2 + \lambda_3)$ quantifies the total transverse momentum with respect to the sphericity axis defined by the four momenta used in event shape measurement (usually, the first eigenvector). The theoretical values fall between $0 \leq S < 1$. However, the inclusion of the smallest eigenvalue λ_3 , the typical maximum value achieved in the experiment is close to $S \simeq 0.8$. $S \rightarrow 0$ indicates a dijet kind of event, while $S \rightarrow 1$ indicates the isotropic events.
- $Y = \frac{\sqrt{3}}{2}(\lambda_2 - \lambda_3)$. Events with both S and Y values are small are cigar-shaped, and collinear, while events with $Y = \frac{1}{\sqrt{3}}S$ (that implies $\lambda_3 = 0$) are disc-shaped and coplanar.
- $C = 3(\lambda_1\lambda_2 + \lambda_1\lambda_3 + \lambda_2\lambda_3)$ measures the events with three jets. $C \rightarrow 0$ indicates dijet events.
- $D = 27\lambda_1\lambda_2\lambda_3$ measures the events with four jets. $D \rightarrow 0$ for dijet or trijet events.

K. Thrust, major and minor, oblateness

Apart from the directly global observables discussed so far, there are other sets of global observables that exist in the literature, such as transverse thrust (τ_\perp), and are defined in terms of the so-called thrust axis for each event. This thrust axis is defined in such a way that the total transverse momentum of the jets used in the measurement is minimized. Mathematically,

$$T = \max_{\hat{n}_\perp} \frac{\sum_i |\vec{p}_i \cdot \hat{n}_\perp|}{\sum_i |\vec{p}_i|} \quad (25)$$

$$T_{\perp} = \max_{\hat{n}_{\perp}} \frac{|\vec{p}_{Ti} \cdot \hat{n}_{\perp}|}{\sum_i |p_{Ti}|} \quad (26)$$

$$\tau_{\perp} = 1 - T_{\perp} \quad (27)$$

where sum runs over all the hadrons produced in the final state with total momentum p_i , transverse momentum p_{Ti} , and the unit vector \hat{n}_{\perp} is used to maximize the sum. The variable τ_{\perp} is defined in terms global transverse thrust T_{\perp} in order to keep the common-event shape definition. The allowed values for τ_{\perp} lies in between the ranges $0 < \tau_{\perp} < 1/3$. This is due to the fact that the allowed values of T_{\perp} fall within the range $0 < T_{\perp} < 2/3$. The smaller the value of τ_{\perp} , denotes for extreme two-jet (i.e cigar-like) events, whereas the higher value denotes spherical events. Here, T is the global event-shape variable thrust. The value of T can vary between 0.5 for spherical events to 1.0 for narrow jet events. Since the thrust variable is linear in momentum, it is more sensitive to low-momentum particles than sphericity.

A plane through the origin and perpendicular to the thrust axis divides the event into two hemispheres H_1 and H_2 as shown in Fig. 21. To obtain the thrust major T_{maj} , the maximization of Eq. 25 is performed within that plane [111]. Furthermore, the thrust minor T_{min} is given by the argument of Eq. 25 and estimated in the direction perpendicular to both thrust major and thrust axes. It is defined as;

$$T_{\text{min}} = \frac{\sum_i |\vec{p}_i \times \hat{n}_{\perp}|}{\sum_i |p_i|} \quad (28)$$

The observable T_{min} is called directly global thrust minor, which measures the out-of-event-plane energy flow.

Using the thrust major T_{maj} and thrust minor T_{min} one can define oblateness (O) as [111]

$$O = T_{\text{maj}} - T_{\text{min}} \quad (29)$$

L. Heavy-jet mass (M_H)

The invariant mass of the particle in each hemisphere, H_1 and H_2 , is calculated, and the heavy-jet mass M_H is defined as the larger of the two [112]. For a given center of mass energy \sqrt{s} , one can define the scaled heavy jet mass ρ_H as follows;

$$\rho = \frac{M_H^2}{s} \quad (30)$$

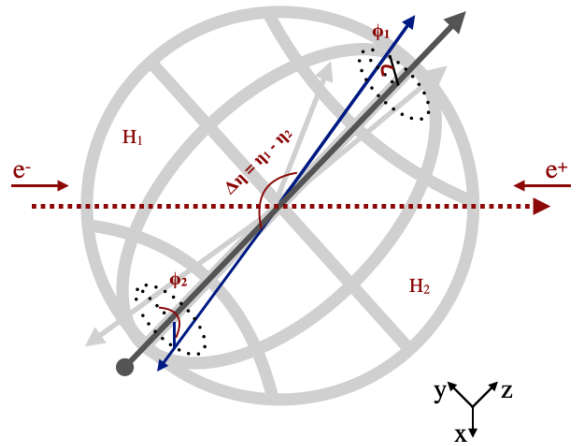


FIG. 21. Depiction of thrust axis used as reference to study the final state particles.

M. Jet broadening variables B_T and B_W

Jet broadening variables measure of the fraction of energy that is perpendicular to the thrust axis. For each of the two hemispheres H_k , one can define [121]

$$B_k = \frac{\sum_{i \in H_k} |\vec{p}_i \times \hat{n}_{\perp}|}{2 \sum_i |p_i|}. \quad (31)$$

Using the definition of B_k , two variables are constructed, such that [122]

$$B_T = B_1 + B_2 \quad \text{and} \quad B_W = \max(B_1, B_2) \quad (32)$$

where B_T is the total jet broadening and B_W is the wide-jet broadening.

These observables τ_{\perp} , ρ , B_T , and B_W are most commonly used in QCD studies in e^+e^- collisions because QCD calculations including the resummation of leading and next-to-leading logarithm (NLLA calculations) terms to all order exist for these observables [122, 123]. The distribution of thrust variable T , scaled heavy jet mass ρ_H , total jet broadenings B_T , and wide-jet broadenings B_W , C , and D parameters in e^+e^- collisions at center of mass energy $\sqrt{s} = 91.2$ GeV is shown in Fig. 22. The experimental data are compared with QCD-based models such as JETSET PS, HERWIG, ARIADNE, and JETSET ME [78, 113–120]. A qualitative agreement between experimental data and model prediction is observed. Furthermore, Fig. 23 shows the first order moment of these same event shape variables as a function of the center of mass energy dependence in e^+e^- collisions. Figure 23 shows that these event shape variables are dominant at the lower center of mass energy and may have a negligible contribution towards the higher center of mass energy, which is the main focus of this review.

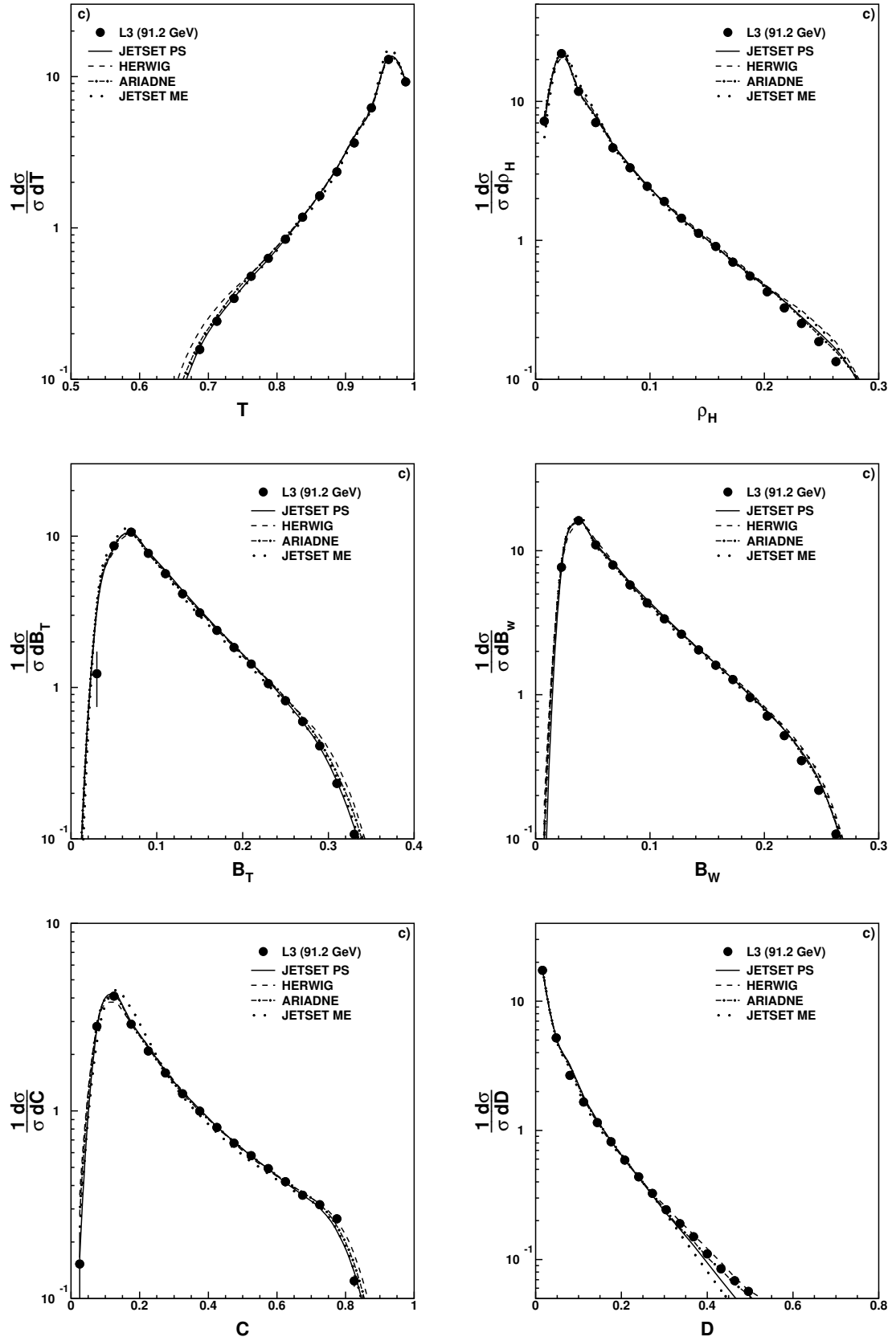


FIG. 22. The distribution of thrust T , heavy jet mass ρ , total and wide-jet broadenings B_T and B_W , C , and D parameters at $\sqrt{s} = 91.2$ GeV in comparison with various QCD model prediction [78, 113–120]

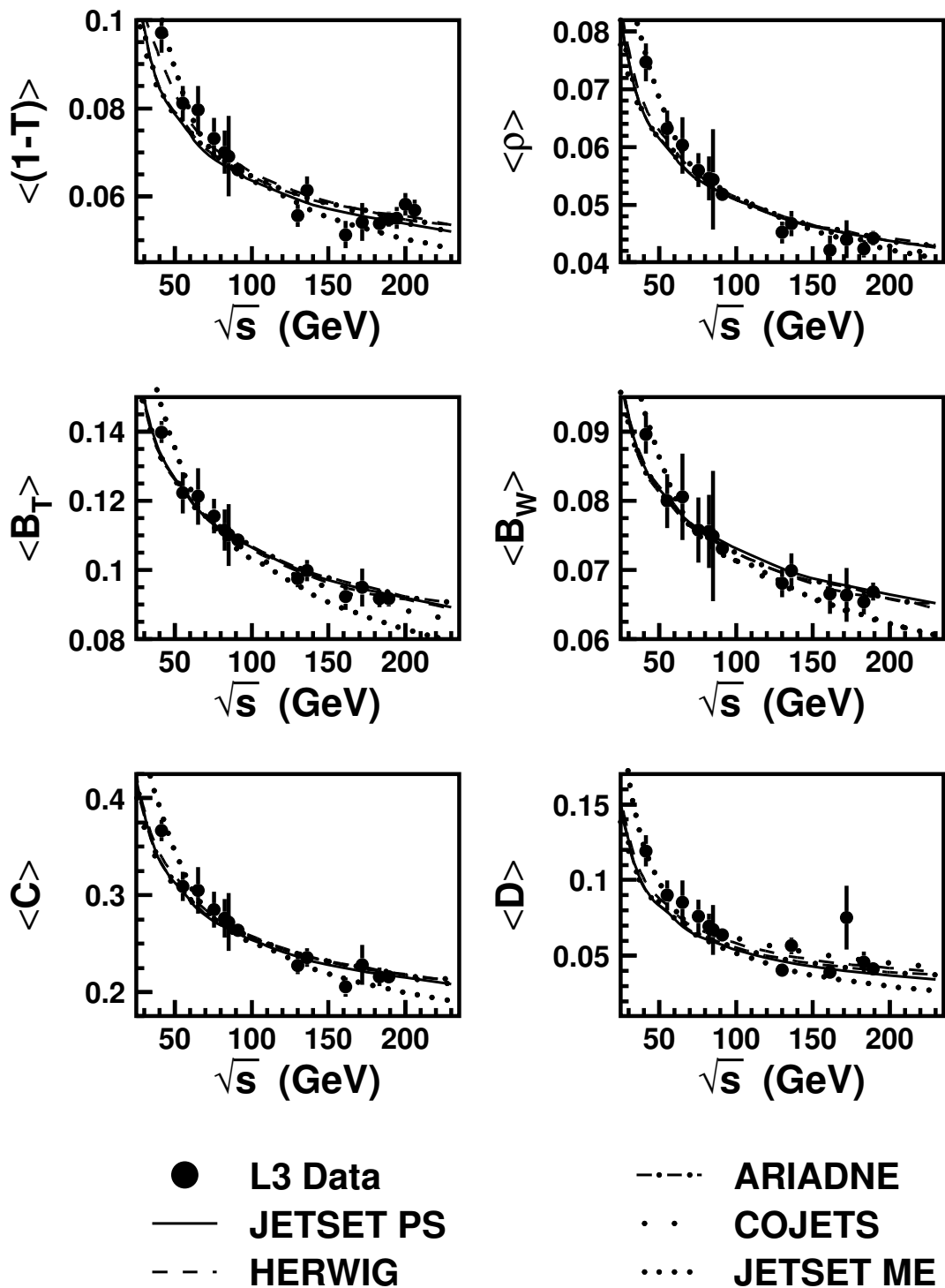


FIG. 23. The first moment of the event shape variables thrust T , heavy jet mass ρ , total and wide-jet broadenings B_T and B_W , C , and D parameters as a function of center of mass energy \sqrt{s} , compared with several QCD model prediction [78, 113–120]

III. MODEL CALCULATIONS

Event generators are the most crucial computational tools used in contemporary high-energy physics phe-

nomenology, enabling to bridge the gap between theoretical models and experimental data. These act as the most effective substitutes for realistic experiments involv-

ing hadronic and nucleus-nucleus collisions (AA). These generators are based on the Monte Carlo techniques for simulating the collisions using physics processes to better understand the nature of the events. Based on the kind of colliding species involved and underlying known physics processes, there are several event generators like AMPT, PYTHIA, EPOS LHC, EPOS4, and HERWIG etc, modeled for hadronic and nuclear collisions. In this study, we employ PYTHIA8 and AMPT models as event generators to explore the possible correlation between all event shape classifiers discussed in Sec. II. The detailed mechanism and event generation using these models are described below.

A. For pp collisions: PYTHIA 8

PYTHIA is a pQCD-inspired general-purpose Monte Carlo event generator used to simulate relativistic hadronic, leptonic, and heavy-ion collisions from RHIC to LHC energies. In PYTHIA8, models and theories are incorporated for a number of physics aspects, such as parton distributions, hard and soft interactions, initial- and final-state parton showers, multiparton interactions, fragmentation, partonic and hadronic decays [124, 125]. A detailed explanation of all physics processes involved in PYTHIA8 can be found in Ref. [126, 127].

In the present study, we use PYTHIA 8.308, an improved version of PYTHIA6, which includes the multipartonic interactions scenario as one of the important improvements. Using the standard Monash 2013 Tune (Tune:pp = 14) [128], we generate 60 million events in pp collisions at $\sqrt{s} = 13$ TeV for this analysis. In this analysis, the inelastic and soft QCD events (Soft-QCD:inelastic=on) are simulated, as a result, the total scattering cross section includes the contribution from all the single, double, and central diffractive components. We have considered the MPI (PartonLevel:MPI = on) along with mode 1 of color reconnection (Colour-Reconnection:mode = 1) and Beam Remnants (Beam-Remnants:remnantMode = 1). The mode 1 of CR is a newer QCD-based scheme which builds on the dipole formation via the QCD color rules as well as the minimization of the string length. This scheme introduces the junction structure, as a result of which junctions are produced between three or four dipoles. A detailed mechanism can be found in Ref. [127]. Additionally, along with the CR mechanism, we employ another hadronization mechanism for color strings known as rope hadronization (RH). The physical description of CR and RH can be found below.

1. Color Reconnection

The hadronisation through the fragmentation-based models, such as Lund's string fragmentation model [129], can be envisaged as a stretched color flux tube between

two partons originating from individual partonic scatterings leading to linear confinements through a massless relativistic string. With the increase in the potential energy of the strings, the quark-antiquark pair moves apart till a new quark-antiquark pair is formed. The hadrons can be formed by combining these quarks and antiquarks. The hadronisation through fragmentation in this scenario is independent of each individual scattering, also shown in Fig. 2 (a). However, in the presence of color reconnection, the strings connecting the partonic endpoints from each individual scattering can color reconnect [130]. This is clearly depicted in Fig. 2 (b). Therefore, the fragmentation of two individual scatterings is dependent on each other when the color reconnection is considered, which induces a rise in average transverse momentum with an increase in the number of individual scatterings or the number of multi-partonic interactions.

2. Rope Hadronisation

In relativistic collisions at LHC energies, a large number of multi-partonic interactions can lead to the production of several strings connecting the partonic endpoints in a smaller transverse region. Within the framework of rope hadronisation, these overlapping strings can act coherently to form a color rope having a large effective string tension. These string-overlap regions usually have a higher energy density as compared to the nearby regions, which can result in the production of a pressure gradient. In the overlap regions, this pressure gradient can push the strings in the outward direction. The pushing of strings outward is called string shoving, which mimics the flow-like pattern observed in heavy-ion collisions. Further, the breaking of strings with a higher effective tension can lead to the production of strange quarks and diquarks, leading to the enhanced production of baryons and strange hadrons in events having a large number of multi-partonic interactions.

The RH mechanism of PYTHIA8 has various tuning parameters. In this study, we use similar settings to the string-shoving mechanism introduced in PYTHIA8. The values of the parameters used for rope hadronization are shown in Table I. Furthermore, the flag partonvertex (PartonVertex:setVertex = on) is used to set impact-parameter plane vertices for partonic production by ISR, FSR, MPI, and beam remnants. In the simulated events, the hadronic level decay mode (HadronLevel:Decay = on) is enabled for all the resonances except the ones used in our study.

To check the compatibility of PYTHIA8 with experimental data, we have used the same tuning as used in one of our previous works described in Ref [60], where we have compared the transverse momentum and pseudorapidity spectra obtained from PYTHIA8 with the ALICE experimental data for all charged particles in pp collisions at $\sqrt{s} = 13$ TeV and found them to be comparable within uncertainties.

Rope Hadronization	Values
Ropewalk:RopeHadronization	on
Ropewalk:doShoving	on
Ropewalk:doFlavour	on
Ropewalk:r0	0.5
Ropewalk:m0	0.2
Ropewalk:beta	1.0
Ropewalk:tInit	1.0
Ropewalk:deltat	0.05
Ropewalk:tShove	10.0

TABLE I. The parameter values of the rope hadronization model used with color reconnection mechanism.

B. For Pb–Pb collisions: AMPT

A Multi-Phase Transport (AMPT) is a hybrid model that combines both the initial partonic collisions and the final hadronic interactions effectively, as well as accounts for the transition between these two distinct phases of matter. It has four major components, namely, initial conditions, partonic interactions, conversion of partonic to hadronic matter through the hadronization mechanism, and hadron interactions. In the present study, we use the string melting (SM) mode of AMPT (version 2.26t9b) as the particle anisotropic flow coefficients and spectra are well described at the intermediate- p_T region by the quark coalescence mechanism for hadronization [131, 132].

1. Initial conditions: The AMPT model employs the heavy-ion jet interaction generator (HIJING)[133] for initial conditions. In the HIJING model, the differential scattering cross section of the energetic minijet partons and soft strings with excited strings, which are further converted to partons, are calculated in pp collisions and then parametrized into the heavy-ion collisions. These are incorporated via the nuclear overlap and shadowing function using an inbuilt Glauber model.
2. Parton transport: The produced partons are then transported into the parton transport part called Zhang’s Parton Cascade (ZPC) model [134]. In the String Melting version of AMPT (AMPT-SM), colored strings melt into low-momentum partons.
3. Hadronization: A spatial coalescence mechanism [84, 135] is used for the hadronization of the transported partons in AMPT-SM, whereas in the default AMPT version, a Lund string fragmentation mechanism is used for hadronization of the transported partons.
4. Hadron transport: The final evolution of produced hadrons is done using a relativistic transport mechanism through meson-meson, meson-baryon, and baryon-baryon interactions [136, 137].

The AMPT settings in the current study are the same as reported in Ref. [138]. The choice of centrality selection has been done using the geometrical slicing of the impact parameter distribution.

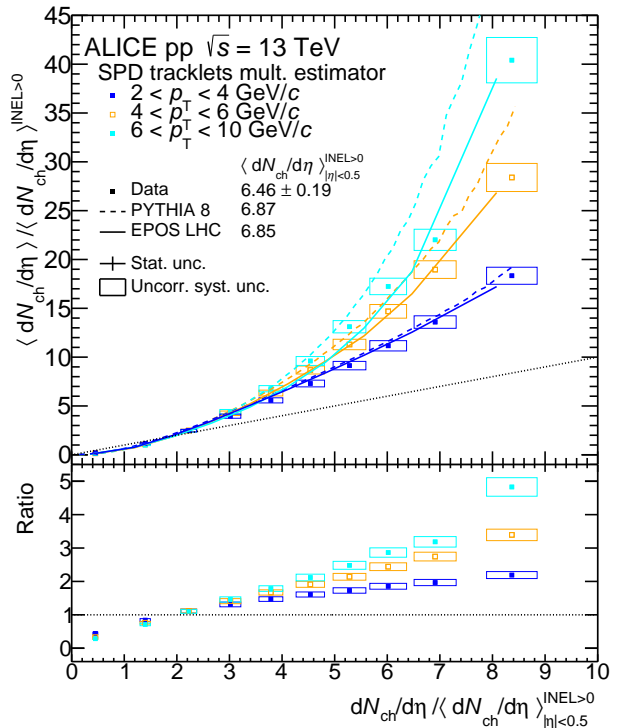


FIG. 24. Self-normalized yield of charged particles integrated over different p_T -intervals: $2 < p_T < 4$ GeV/c (blue), $4 < p_T < 6$ GeV/c (yellow) and $6 < p_T < 10$ GeV/c (cyan) as a function of p_T -integrated self-normalised charged-particle multiplicity density [25]. ALICE data are compared with measurements obtained with PYTHIA 8 and EPOS LHC.

IV. INTERPRETATION OF QGP-LIKE SIGNALS WITH EVENT CLASSIFIERS

A. Integrated yield and transverse momentum spectra

Let us now resume our discussion about selection and auto-correlation biases, which we started in Sec. I with the results of transverse momentum spectra. As discussed, to have a proxy for MPI in experiments, several measurements have been performed as a function of charged-particle multiplicity measured in mid- and forward-pseudorapidity regions, which, in MC studies, show significant correlations with N_{mpi} . However, measurements by event selections based only on mid-rapidity multiplicity have shown a stronger than linear increase of high- p_T particles in high multiplicity (HM) collisions relative to the yield in minimum-bias (MB) pp colli-

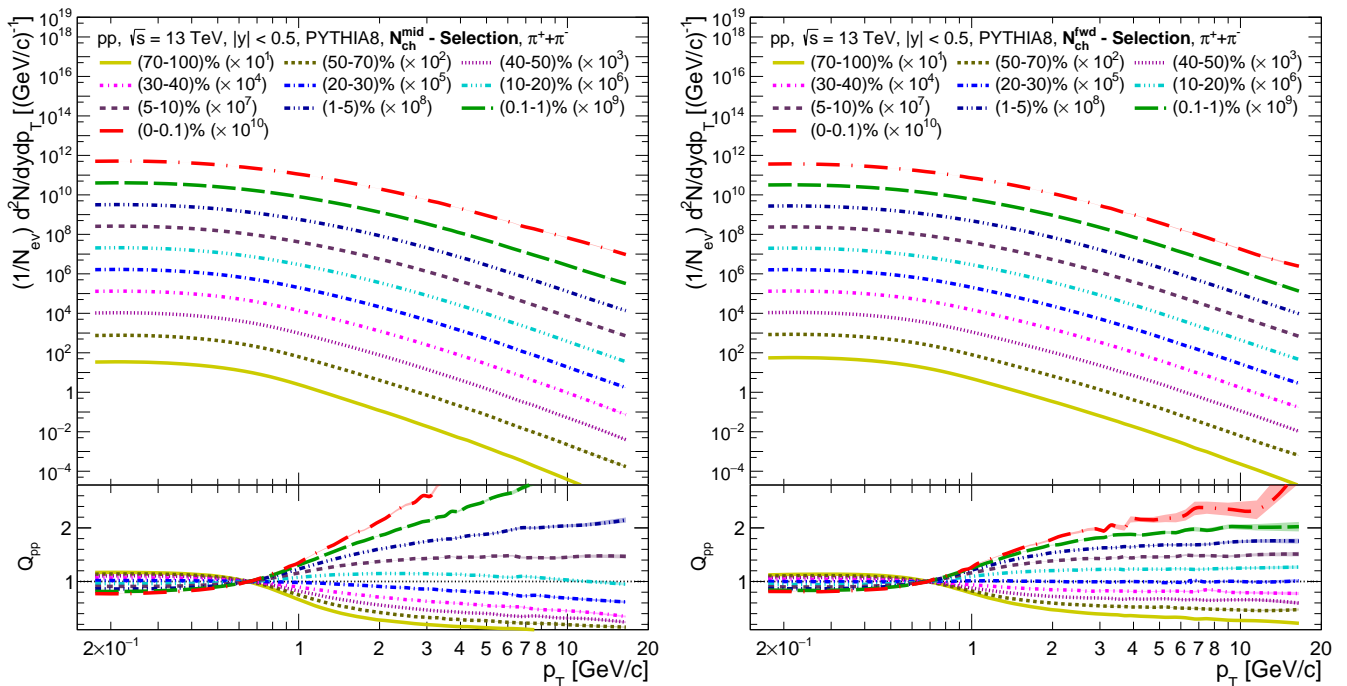


FIG. 25. Transverse momentum distribution of charged pions for different slices of midrapidity (left panel) and forward rapidity (right panel) charged-particle multiplicity in pp collisions at $\sqrt{s} = 13$ TeV using PYTHIA8. The bottom panels show the ratio with respect to the minimum bias (MB) events.

sions [17, 25], as illustrated in Fig. 24. This is also highlighted in the top panel of Fig. 25, where the transverse momentum distribution of charged pions for different slices of midrapidity charged-particle multiplicity in pp collisions at $\sqrt{s} = 13$ TeV is shown from PYTHIA8 simulations. The p_T -dependence of selection bias can be understood from the ratio panels with Q_{pp} , defined as follows [55, 59, 139].

$$Q_{pp} = \frac{d^2 N_{ch}^{ES} / \langle N_{ch}^{ES} \rangle d\eta dp_T}{d^2 N_{ch}^{ES-int} / \langle N_{ch}^{ES-int} \rangle d\eta dp_T} \quad (33)$$

Here, N_{ch}^{ES} and N_{ch}^{ES-int} denote the number of charged particles in a given percentile of event shape and the event shape integrated events. In the ratio plot with respect to the minimum bias collisions, one can clearly see that with increasing multiplicity, the particle production at high- p_T is biased towards the hard processes, which gives rise to a stronger than linear increase. This indicates a selection bias towards local fluctuations of choosing only hard pp collisions. Such biases can be diminished when the event selection is performed with the charged particle multiplicity estimated in a different pseudorapidity interval than the observable of interest. Bottom panel of Fig. 25 shows the transverse momentum distribution of charged pions for different slices of forward charged-particle multiplicity in pp collisions at $\sqrt{s} = 13$ TeV from PYTHIA8 simulations. It is found that these

measurements are affected by the hard processes at high- p_T [26], which is evident from the ratio to minimum bias collisions. Thus, such selection biases in measurements hinder the search for the origin of QGP-like behavior in small collision systems.

Let us now move our discussion to the event shape classifiers. As discussed so far, we are mostly interested in the soft-QCD sector to find out QGP-like effects, one needs to explore event classifiers that are sensitive to MPI with significant reduction of selection bias. Event shape observables are expected to be sensitive to MPI. Figure 26 shows a correlation between average number of multipartonic interactions ($\langle N_{mpi} \rangle$) and the average transverse momentum transfer of the hardest parton-parton interaction ($\langle \hat{p}_T \rangle$) as a function of different percentiles of event classifiers. It can be clearly seen that all the discussed event classifiers are sensitive to MPI. Among those, R_T probes higher p_T ranges due to high- p_T trigger selection. As there is an inherent multiplicity cut of 10 particles, the MPI-coverage for sphericity and sphericity selections is limited. Figure 27 shows the transverse momentum distribution of charged pions for different slices of N_{mpi} in pp collisions at $\sqrt{s} = 13$ TeV using PYTHIA8.

When studied as a function of sphericity, (un)weighted sphericity and R_T in Figs. 28, 29, 30, respectively, one observes a hint of selection bias similar to Fig. 25 for all these event shape selections. In particular, Figs. 28 and 29 show that low- p_T particles are insensitive to sphericity and sphericity selections. At high- p_T , the be-

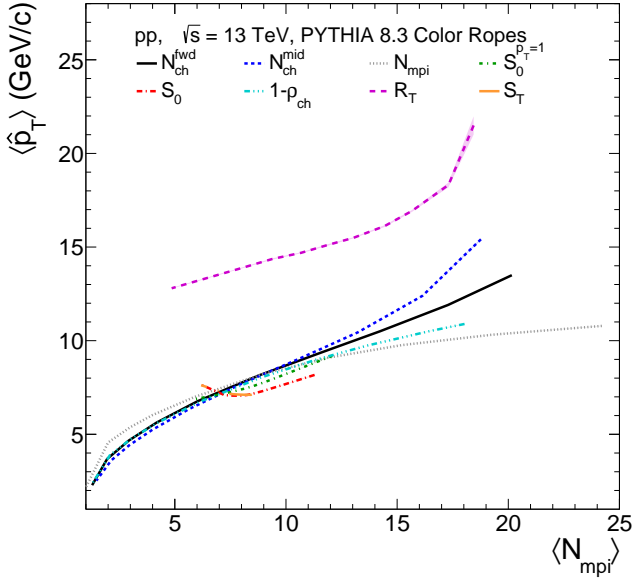


FIG. 26. Correlation between $\langle N_{\text{mpi}} \rangle$ and $\langle \hat{p}_T \rangle$ as a function of different percentiles of event classifiers. Comparisons are made for the Color Ropes tune of PYTHIA 8.

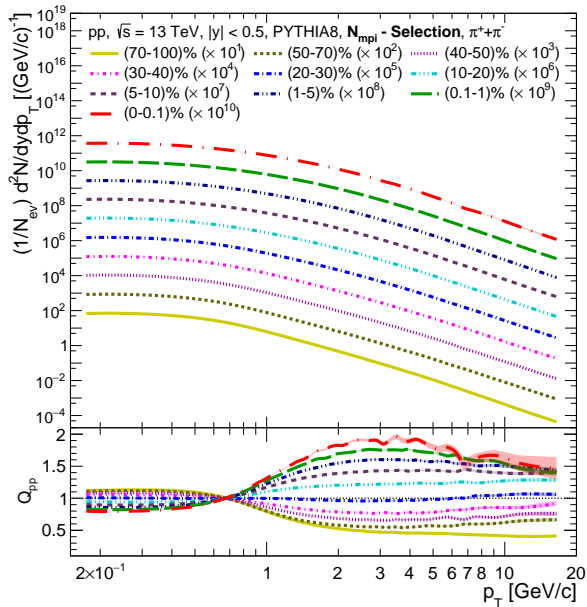


FIG. 27. Top panel shows the transverse momentum distribution of charged pions for different slices of the number of multi-partonic interactions (N_{mpi}) in pp collisions at $\sqrt{s} = 13$ TeV using PYTHIA8. The bottom panel shows the ratio with respect to the minimum bias (MB) events.

havior of Q_{pp} is opposite to that of N_{mpi} selection. As discussed above, this could be an artifact of the inherent multiplicity cut of 10 particles. Further, the events with smaller values of sphericity and sphericity are bi-

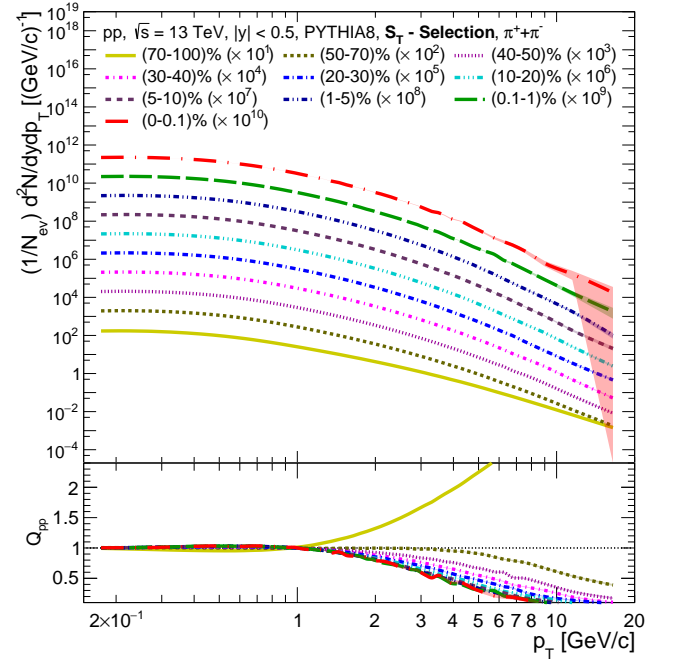


FIG. 28. Top panel shows the transverse momentum distribution of charged pions for different slices of transverse sphericity (S_T) in pp collisions at $\sqrt{s} = 13$ TeV using PYTHIA8. The bottom panel shows the ratio with respect to the minimum bias (MB) events.

ased towards jets, leading to an enhancement structure in high- p_T regions, which is otherwise absent. Similar features of Q_{pp} for sphericity selection are also shown in Ref. [59]. This can also be confirmed from Fig. 26, where event selections with S_0 , $S_0^{p_T=1}$ and S_T show a small rise in $\langle \hat{p}_T \rangle$ towards lower $\langle N_{\text{mpi}} \rangle$. Experimentally the effect of the auto-correlation bias in R_T is explicitly studied by ALICE via the measurement of charged particles' transverse momentum spectra in pp collisions for toward, away, and transverse regions the pion spectra in toward, away, and transverse regions as a function of R_T as shown in Fig. 31 [52].

Also, the measurement of pion spectra as a function of R_T in pp collisions at $\sqrt{s} = 13$ TeV with ALICE, shown in Fig. 32 [51]. Here, the lower panel shows the ratio with respect to the $R_T \geq 0$ case. Interestingly, for both charged-particle and pion spectra in the toward and away regions, with an increase in p_T , the spectra measured in different R_T values approach to $R_T \geq 0$ case, as can be seen in the lower panel. However, for the case of the transverse region, a deviation from the $R_T \geq 0$ case is observed as one approaches a higher value of p_T . As R_T is measured using the charged-particle multiplicity in the transverse regions, the deviation from $R_T \geq 0$ for the transverse case can be attributed to the auto-correlation in the measurement of charged pions where the event shape, R_T is defined. On the other hand, for the toward and away regions, where this auto-correlation

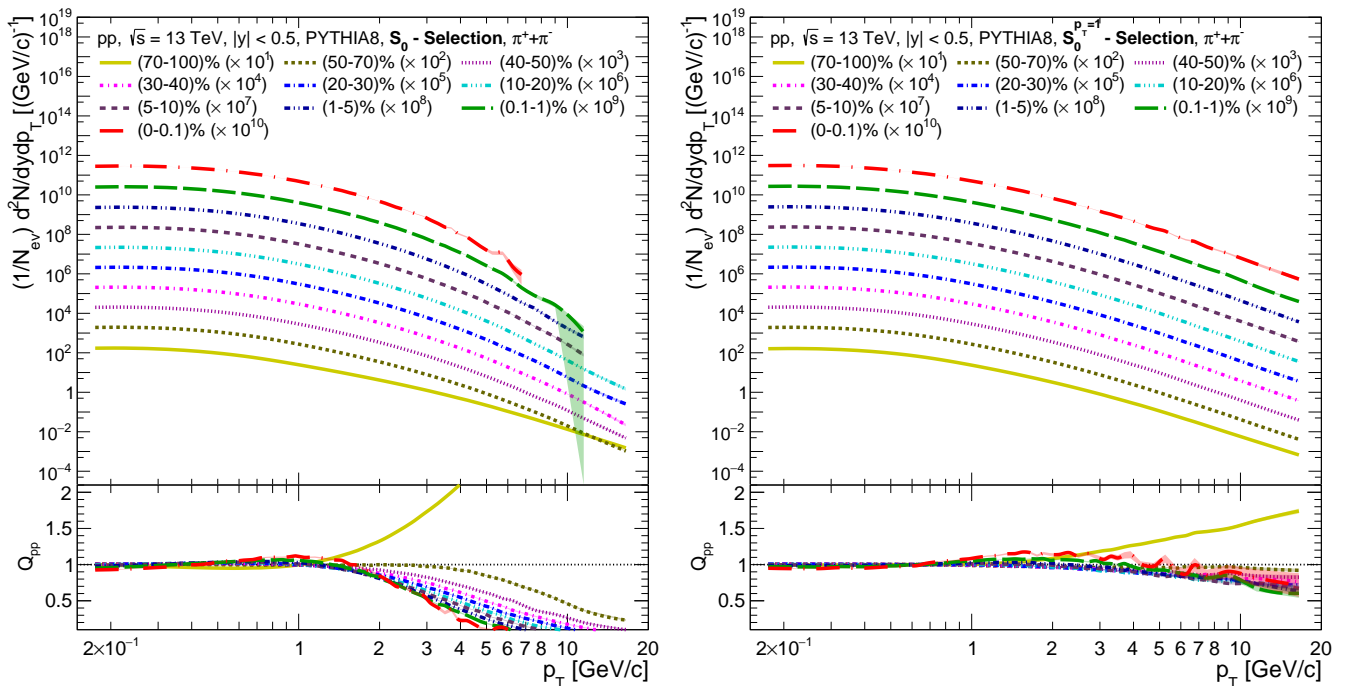


FIG. 29. Top panel shows the transverse momentum distribution of charged pions for different slices of S_0 (left) and $S_0^{p_T=1}$ (right) in pp collisions at $\sqrt{s} = 13$ TeV using PYTHIA8. The bottom panel shows the ratio with respect to the minimum bias (MB) events.

bias is absent and due to a large correlation of R_T with N_{mpi} , the pion spectra approach the $R_T \geq 0$ towards the higher p_T regions.

The closest to the trend of MPI selections (grey line) is the charged-particle flattonicity, which indicates that flattonicity is the robust observable against the selection bias of choosing high- p_T particles. This can also be concluded from model prediction in Fig. 33 and measured data in Fig. 34. The measured Q_{pp} versus p_T for different flattonicity event classes shows a similar behavior as shown in Fig. 27, where the event classes are defined based on the number of multiple partonic interactions.

B. Average transverse momentum

In a hydrodynamic expanding system, the presence of high energy density and outward pressure gives a radial boost to all the produced hadrons. The presence of this outward radial boost, or radial flow, gives an additional boost to the produced hadrons in addition to their thermal expansion. This results in an increase in the transverse momentum of the particles. Here, in the presence of such a radial boost, the hadrons with a larger mass are significantly affected as compared to the hadrons with a lower mass. This boost effect is usually reflected in the mean transverse momentum ($\langle p_T \rangle$) of the produced hadrons, where the presence of a higher radially boosted medium is reflected in the enhanced value of $\langle p_T \rangle$ of the

hadrons. Recently, such radial flow-like features are observed in pp collisions [140, 141], which were traditionally considered for baseline measurements for the signatures of quark-gluon plasma.

Interestingly, PYTHIA8 with color reconnection is able to qualitatively explain such radial flow-like features observed in pp collisions in experiments without taking the hydrodynamic evolution of partons into account [142]. In PYTHIA8, when a string connecting two partons moves, it gives a common boost to the string fragments. In the absence of CR, if a parton is emitted in the midrapidity, the other end of the string will be part of the proton moving forward, leading to a small boost [142]. However, in the presence of CR, the partons from two independent scatterings can color reconnect and lead to an enhanced boost [142]. In addition, this boosting effect is expected to be largely enhanced in the case of a large number of multi-partonic interactions [142]. Figure 35 shows $\langle p_T \rangle$ of charged, identified, and strange hadrons measured in midrapidity as a function of N_{mpi} in pp collisions using PYTHIA8. For any particle species, $\langle p_T \rangle$ is observed to rise to higher values with an increase in N_{mpi} till $N_{\text{mpi}} \lesssim 20$. This is because, with an increase in N_{mpi} , the partons can color reconnect easily, thus leading to a larger boost and an enhanced value of $\langle p_T \rangle$. However, since the total available energy for particle production is limited, N_{mpi} increases at the cost of the average value of the partonic momentum. Thus, for $N_{\text{mpi}} \gtrsim 20$ region, CR suffers from an increase in N_{mpi} and a drop

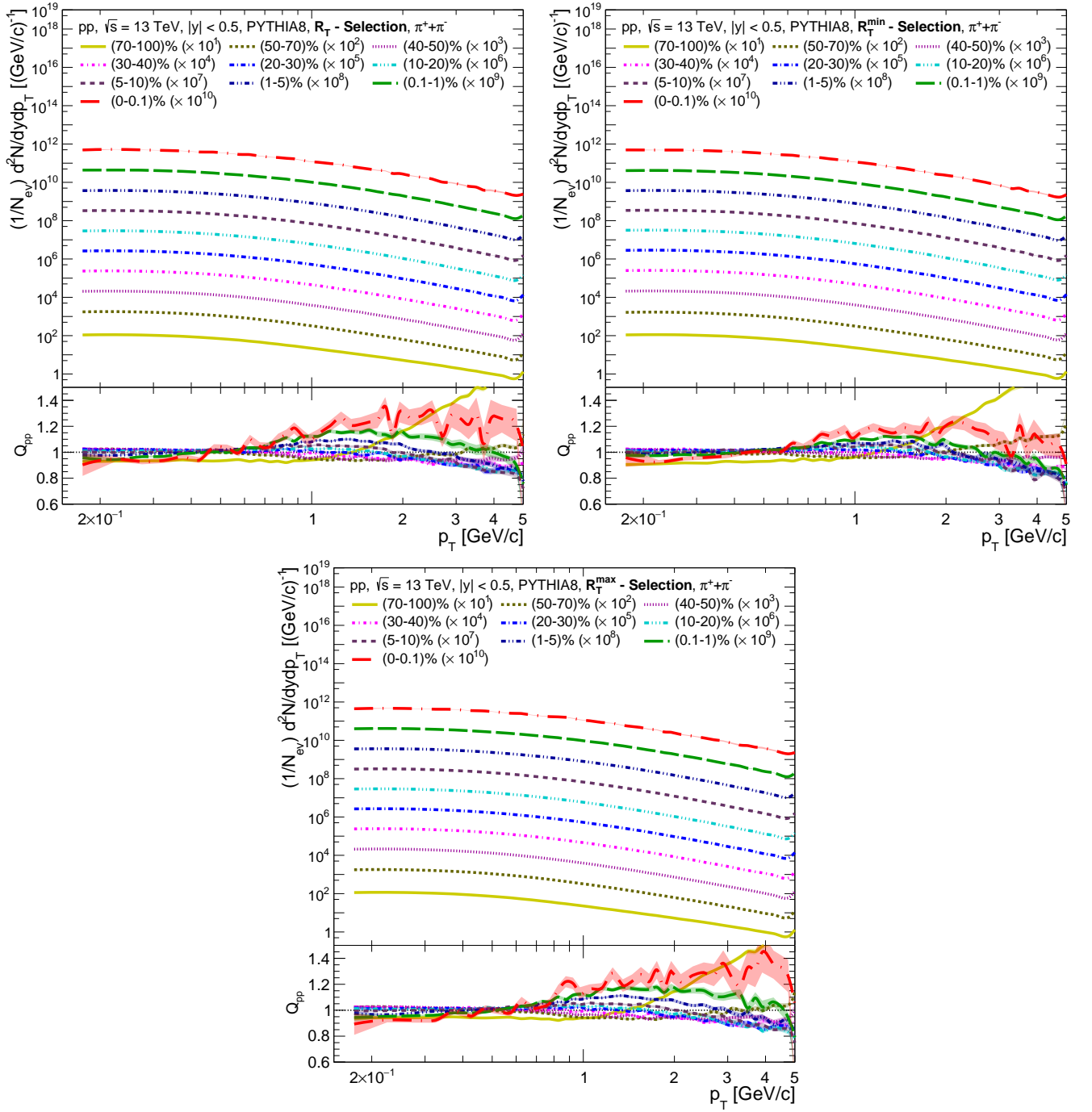


FIG. 30. Top panel shows the transverse momentum distribution of charged pions for different slices of R_T (left), R_T^{\min} (upper right), and R_T^{\max} (right) in pp collisions at $\sqrt{s} = 13$ TeV using PYTHIA8. The bottom panel shows the ratio with respect to the minimum bias (MB) events.

in partonic momentum, leading to a saturation behavior in hadron $\langle p_T \rangle$. Another remarkable observation can be made by looking at the rise of $\langle p_T \rangle$ with N_{mpi} for different species of hadrons. The increase of $\langle p_T \rangle$ with N_{mpi} becomes steeper when the particle mass increases, indicating a larger radial boost for particles with a higher

mass. In addition, a small rise in the low N_{mpi} region is also observed, which becomes more distinct with an increase in particle mass. This is expected to arise from the production of heavier particles from the initial hard interactions. As in PYTHIA8, CR with high N_{mpi} gives rise to enhanced radial flow-like effects, we try to probe

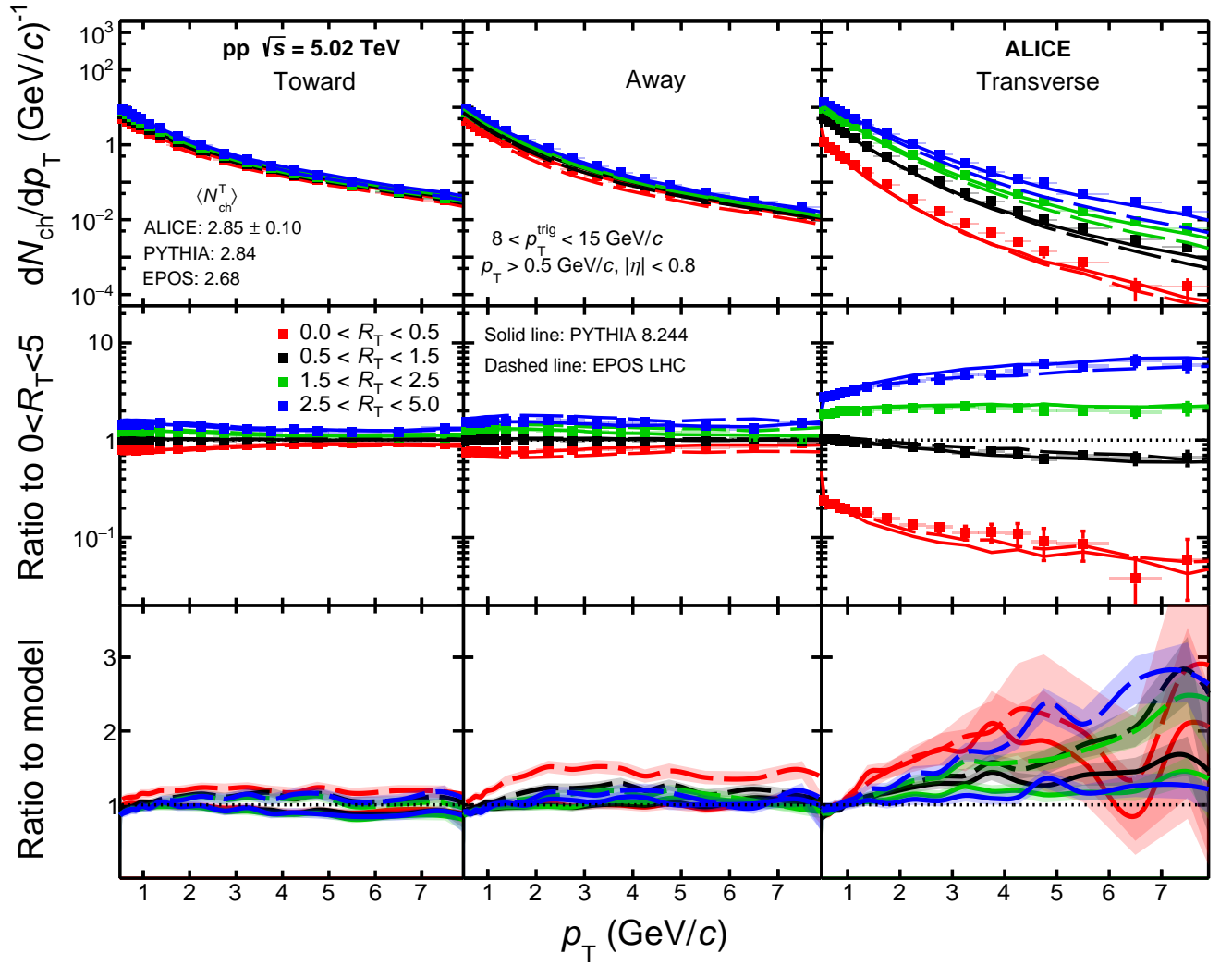


FIG. 31. Transverse momentum spectra of charged particles in toward, away, and transverse regions, from left to right for different events selected based on R_T in pp collisions at $\sqrt{s} = 5.02$ TeV with ALICE [52]. The upper right panel shows the ratio of pion spectra for different regions of R_T to the charged-particle spectra measured for the $R_T \geq 0$ case [52]. The bottom panel shows the ratio of data to models like PYTHIA 8 and EPOS LHC.

the effects of N_{mpi} selection on $\langle p_T \rangle$ with different event shape observables.

Figure 36 shows $\langle p_T \rangle$ of particles as a function of charged-particle multiplicity measured in the midrapidity ($N_{\text{ch}}^{\text{mid}}$) (left) and forward rapidity ($N_{\text{ch}}^{\text{fwd}}$) (right) in pp collisions at $\sqrt{s} = 13$ TeV using PYTHIA8. The $\langle p_T \rangle$ of particles as a function of both $N_{\text{ch}}^{\text{mid}}$ and $N_{\text{ch}}^{\text{fwd}}$ have a similar behavior going from low multiplicity to high multiplicity, as compared to $\langle p_T \rangle$ vs N_{mpi} shown in Fig. 35. However, we do not see the saturation behavior of $\langle p_T \rangle$ with the increase in multiplicity in the midrapidity and forward rapidity regions. Although $N_{\text{ch}}^{\text{mid}}$ and $N_{\text{ch}}^{\text{fwd}}$ have significant correlations with N_{mpi} , as shown in Fig. 8, due to a significant contribution of jet topologies in the high-multiplicity regions a continuous rise in $\langle p_T \rangle$ with multiplicity is observed. The rise of $\langle p_T \rangle$ with multi-

plicity shown in Fig. 36 are qualitatively consistent with experimental findings [19, 140]. Also, one observes a significant rise in the steepness of $\langle p_T \rangle$ vs N_{ch} with increasing particle mass. The steepness further increases when one considers the $N_{\text{ch}}^{\text{mid}}$ for the event selection compared to $N_{\text{ch}}^{\text{fwd}}$.

Figure 37 shows $\langle p_T \rangle$ of particles as a function of S_T in pp collisions at $\sqrt{s} = 13$ TeV using PYTHIA8. Here, the intrinsic mass dependence of $\langle p_T \rangle$ is observed. However, unlike N_{mpi} , $N_{\text{ch}}^{\text{mid}}$ or $N_{\text{ch}}^{\text{fwd}}$ the steepness of $\langle p_T \rangle$ towards the isotropic events is not observed. Furthermore, the event selection based on S_T is found to have a bias towards the charged particles. As can be seen in Fig. 37, the variation of $\langle p_T \rangle$ with S_T is negligibly small for the neutral particles, such as $\Lambda + \bar{\Lambda}$ and K_S^0 . In addition, $\langle p_T \rangle$ is observed to maintain a consistent value and slightly de-

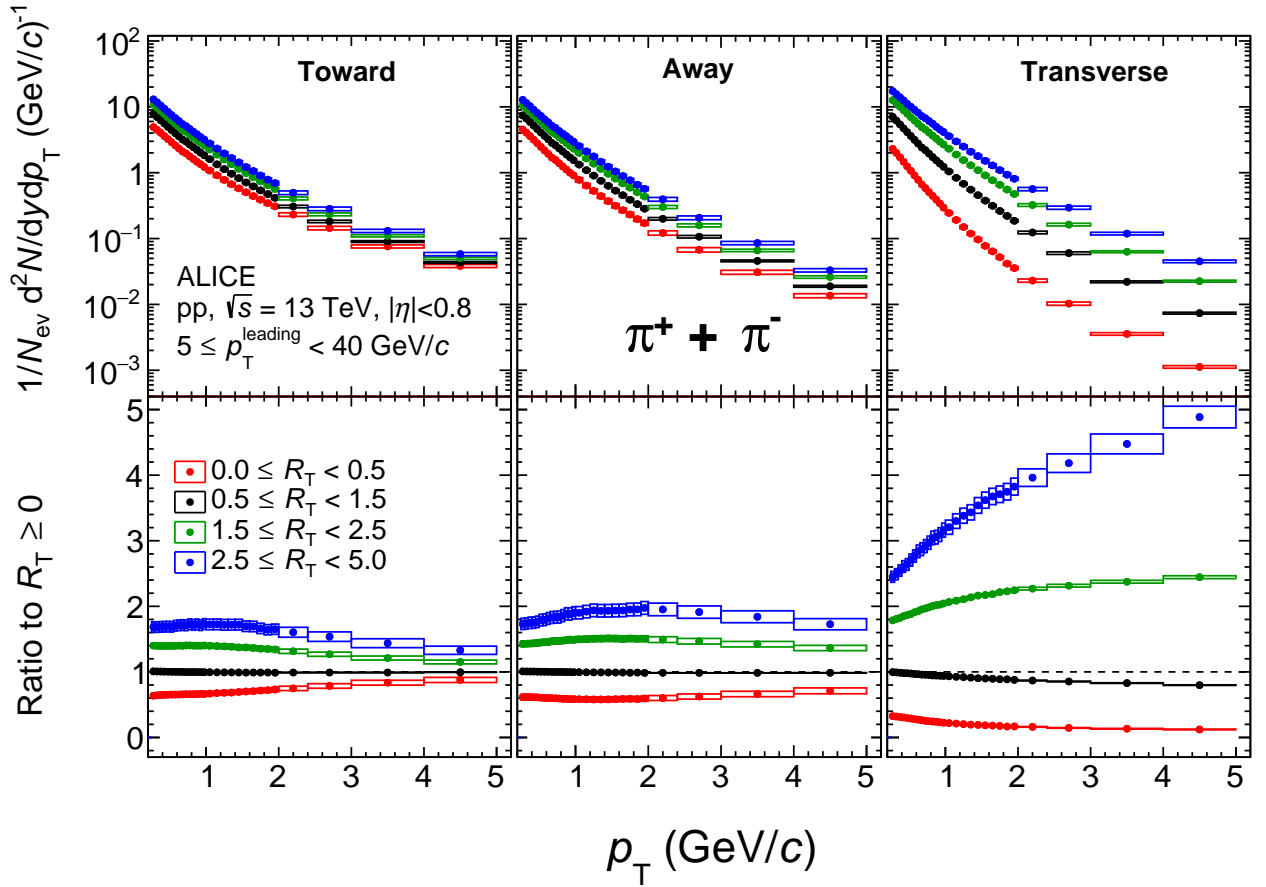


FIG. 32. Transverse momentum spectra of pions in toward, away, and transverse regions, from left to right for different events selected based on R_T in pp collisions at $\sqrt{s} = 13$ TeV with ALICE [51]. The lower panel shows the ratio of pion spectra for different regions of R_T to the pion spectra measured for $R_T \geq 0$ case [51].

crease when going towards the isotropic events. Due to the weak correlation of S_T with N_{mpi} , one observes little to no significant effects of event selection based on S_T in $\langle p_T \rangle$. Similarly, the $\langle p_T \rangle$ of all charged particles as a function of S_T in minimum bias pp collisions at $\sqrt{s} = 7$ TeV is shown in the top panel of Fig. 38 for two multiplicity bins, i.e. $3 \leq N_{\text{ch}} \leq 9$ (left), and $N_{\text{ch}} \geq 30$ (right) obtained using four different MC generators: PHOJET, ATLAS-CSC, PERUGIA-2011, and PYTHIA8. From Fig. 38 it is observed that a large dependence of $\langle p_T \rangle$ on sphericity event-shape is found at higher multiplicity regions. The bottom panel shows the contribution of each sphericity bin to the final $\langle p_T \rangle$, i.e., $\langle p_T \rangle$ weighted by the value $P(S_T)$. The contribution to $\langle p_T \rangle$ in the multiplicity bin is twice larger for PHOJET compared to ATLAS-CSC, although these two MC models have the same contribution to $\langle p_T \rangle$ [44].

Figure 39 shows $\langle p_T \rangle$ of particles measured in $|\eta| < 0.8$ and $p_T > 0.15$ GeV/c as a function of transverse sphericity in pp collisions at $\sqrt{s} = 13$ TeV using PYTHIA8. The top panel shows S_0 versus $\langle p_T \rangle$ and the bottom panel

represents $S_0^{p_T=1}$ versus $\langle p_T \rangle$. For all the particle species, a rise of $\langle p_T \rangle$ towards the lower value of S_0 is observed; this can be attributed to larger jet contributions in such events. For the charged particles, $\langle p_T \rangle$ decreases from lower to higher values of S_0 , which becomes clear for the heavier particles. However, event selection based on S_0 is found to affect neutral particle $\langle p_T \rangle$ differently. Here, $\langle p_T \rangle$ of lambda hyperons ($\Lambda + \bar{\Lambda}$) and K_S^0 first decreases and finally starts to increase as S_0 increases. This event selection bias based on S_0 for neutral and charged particles can be fixed when one considers $p_T = 1$ for the estimation of transverse sphericity. As can be seen in Fig. 39 bottom panel, all the particles, independent of the charge of the particle, retain a similar rising trend of $\langle p_T \rangle$ throughout $S_0^{p_T=1}$. The rise of $\langle p_T \rangle$ becomes prominent towards $S_0^{p_T=1} > 0.85$ as one goes from lower to higher values of $S_0^{p_T=1}$. This is because the low $S_0^{p_T=1}$ region gets higher contribution from the jets while high values of $S_0^{p_T=1}$ may show enhanced flow like effect leading to higher values of $\langle p_T \rangle$. The effect becomes clearer as the particle mass increases.

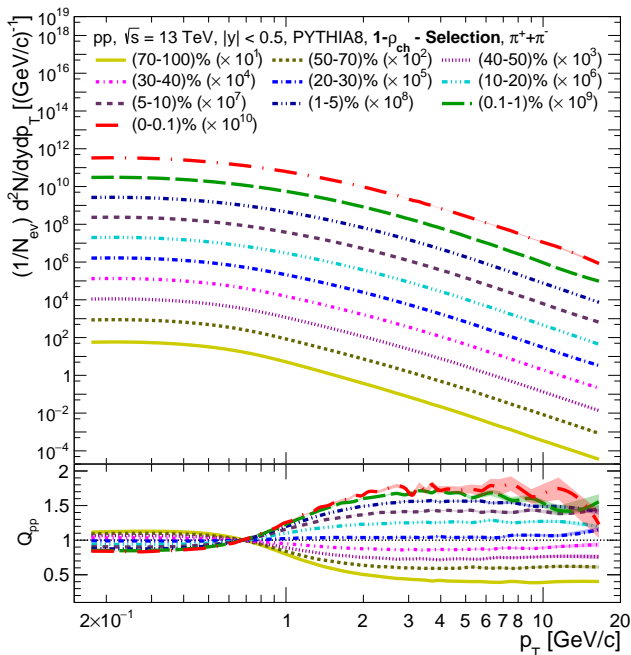


FIG. 33. Top panel shows the transverse momentum distribution of charged pions for different slices of charged-particle flattening (ρ_{ch}) in pp collisions at $\sqrt{s} = 13$ TeV using PYTHIA8. The bottom panel shows the ratio with respect to the minimum bias (MB) events.

Figure 40 shows $\langle p_T \rangle$ versus event multiplicity ($dN_{ch}/d\eta$) for different classes of S_0 in pp collisions at $\sqrt{s} = 13$ TeV with ALICE. With the increase in event multiplicity, $\langle p_T \rangle$ rises. In PYTHIA 8, this is explained by CR, also shown in Fig. 36. When S_0 -integrated data is compared with the isotropic case, a suppression in $\langle p_T \rangle$ is observed within systematics. In contrast, the jetty events show an enhanced value of $\langle p_T \rangle$ throughout the multiplicity region. This feature is captured by PYTHIA 8, as shown in Fig. 39 upper panel for all charged hadrons.

Figure 41 shows $\langle p_T \rangle$ for particles at $|\eta| < 0.8$ and $0.15 < p_T < 5$ GeV/c as a function of R_T (top), R_T^{\min} (upper right) and R_T^{\max} (bottom) in pp collisions at $\sqrt{s} = 13$ TeV using PYTHIA8. Since, for the estimation of R_T , R_T^{\min} and R_T^{\max} , only the events having $p_T^{\text{lead}} > 5$ GeV/c are selected, we restrict the estimation of $\langle p_T \rangle$ only for the particles having $0.15 < p_T < 5$ GeV/c. As one may notice, $\langle p_T \rangle$ shows an increasing trend with the increase in the value of R_T , R_T^{\min} and R_T^{\max} , where, the increment is enhanced for heavier particles. This enhancement of $\langle p_T \rangle$ with increasing R_T , R_T^{\min} and R_T^{\max} is qualitatively consistent with N_{mpi} based event selections. In addition, one may notice that the increment slope of $\langle p_T \rangle$ is higher for R_T compared to R_T^{\min} and R_T^{\max} . Further, a slight increment of $\langle p_T \rangle$ is seen for R_T , R_T^{\min} , $R_T^{\max} < 1$, similar to the events selected based on N_{mpi} , as shown in Fig. 35. As the events are selected based on a high momentum trigger, events with a lower underlying activity may have

a lower value of R_T , R_T^{\min} , and R_T^{\max} and are dominated with jets. This can contribute to enhanced $\langle p_T \rangle$ for the events with lower R_T , R_T^{\min} , and R_T^{\max} .

Figure 42 shows the average transverse momentum of charged protons, kaons and pions measured in toward, away, and transverse regions as a function of R_T in pp collisions at $\sqrt{s} = 13$ TeV with ALICE [51]. In the toward region, for the charged kaons and pions, as one moves from low R_T (low UE) to a higher R_T (large UE) region, $\langle p_T \rangle$ decreases. This represents the presence of jet-fragmentations, which are low-mass particles (pions and kaons) having large transverse momentum in the R_T (low UE) region. Further, with an increase in R_T , the UE contribution and due to the jet-dilution effect, a saturation of $\langle p_T \rangle$ with an increase in R_T is observed. Conversely, $\langle p_T \rangle$ for protons show a rise with R_T which can be attributed to enhanced radial flow effects with increasing R_T . The decrease of $\langle p_T \rangle$ with R_T for pions and kaons is well explained by all the considered models. However, the $\langle p_T \rangle$ for protons is correctly explained only with EPOS LHC.

In the away-side region, the particle production mechanism is similar to the toward regions and is dominated by the away-side jet. Here, for all the particle species, a rise in $\langle p_T \rangle$ is inferred with an increase in R_T . This is because, in the away-side region, the contribution from the particle fragmentation is smaller as compared to the toward region and with a rise in R_T , the UE dominated particle production leading to dominating-radial flow effects which causes a rise in $\langle p_T \rangle$ with R_T . The rise of $\langle p_T \rangle$ is smaller for pions than for kaons than for protons. Here, EPOS LHC explains the $\langle p_T \rangle$ for protons but underestimates $\langle p_T \rangle$ for pions and kaons.

In the transverse region, we see a clear mass ordering of $\langle p_T \rangle$ for different particle species. A strong rise in $\langle p_T \rangle$ with an increase in R_T is observed for all the particle species. The rise of $\langle p_T \rangle$ is stronger for protons and kaons than pions. A similar observation is made as a function of charged-particle multiplicity [18]. This behavior is an indication of auto-correlation bias caused by measuring both particles and R_T in a similar region of $\Delta\phi$. The high multiplicity requirement in the transverse region increases the probability of having a jet in the same region. Here, all the considered models give a qualitative description of $\langle p_T \rangle$ versus R_T for pions, kaons, and protons.

Figure 43 shows $\langle p_T \rangle$ of particles measured in $|\eta| < 0.8$ and $p_T > 0.15$ GeV/c as a function of charged-particle flattening (ρ_{ch}). In Fig. 43, with an increase in the value of ρ_{ch} corresponding value of $\langle p_T \rangle$ also increases for all the particle species shown in the figure. In addition, the value of $\langle p_T \rangle$ follows a clear mass dependence where the heavier mass particles possess a larger increasing slope with an increase in the value of ρ_{ch} compared to the particles with a lower mass. Further, a saturation behavior in $\langle p_T \rangle$ is observed towards $(1 - \rho_{ch}) \gtrsim 0.9$. Flattening is one of the observables that is found to closely follow the trend of increasing $\langle p_T \rangle$ for event selection based on N_{mpi} and

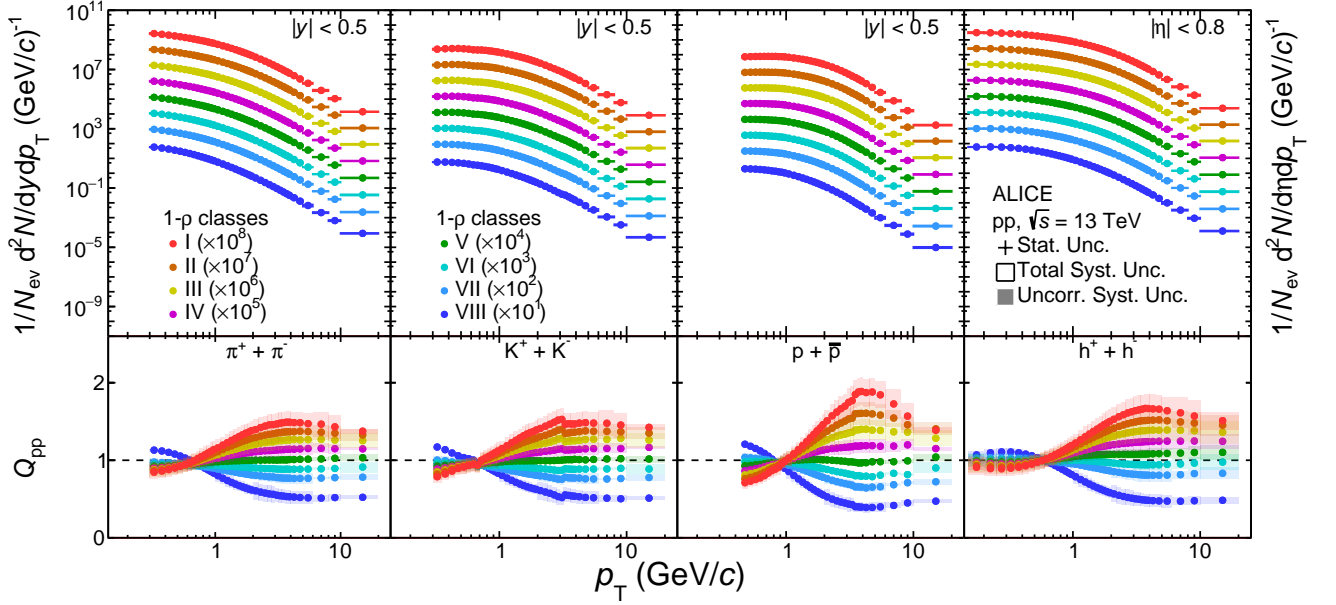


FIG. 34. The upper panel shows the transverse momentum distribution of charged pions, kaons, protons, and charged hadrons, from left to right, for different charged-particle flattonicity classes in pp collisions at $\sqrt{s} = 13$ TeV with ALICE. The lower panel shows Q_{pp} versus p_T for the corresponding flattonicity event class. The figure is taken from Ref. [55]

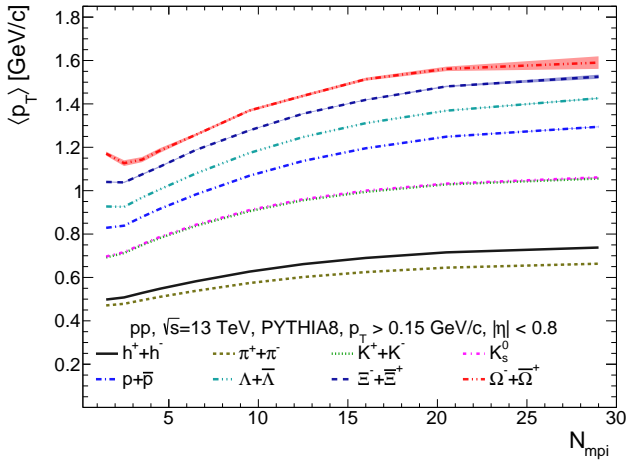


FIG. 35. Mean transverse momentum of all charged and identified hadrons as a function of the number of multi-partonic interactions (N_{mpi}) in pp collisions at $\sqrt{s} = 13$ TeV using PYTHIA8.

the qualitative enhancement feature of $\langle p_T \rangle$ is observed only in $0.75 < (1 - \rho_{ch}) < 0.9$, where the most of the events lie.

C. Strangeness enhancement

In this section, we explore the event shape observable dependence of particle production of primary strange (K_S^0 , Λ , $\bar{\Lambda}$) and multi-strange (Ξ^+ , Ξ^- , Ω^+ , Ω^-) hadrons in pp collisions at $\sqrt{s} = 13$ TeV using PYTHIA8. Recent experimental observation of pp collisions indicates a significant enhancement in the ratio of strange to non-strange particles as a function of charged-particle multiplicity, similar to those observed in heavy-ion collisions [17, 140]. This enhancement in pp collisions creates a spark in the heavy-ion community and puts a question mark on the assumption of considering pp as the reference system.

As discussed above, the charged-particle multiplicity serves as a probe to disentangle the hard and soft events. This motivates us to study the yield ratios of strange to non-strange hadrons as a function of other event shape classifiers such as the number of multi-partonic interactions, transverse sphericity, transverse sphericity, relative transverse activity classifier, charged-particle flattonicity, etc. Here, we mainly investigate $2K_S^0/(\pi^+ + \pi^-)$, $(\Lambda + \bar{\Lambda})/(\pi^+ + \pi^-)$, $(\Xi^+ + \Xi^-)/(\pi^+ + \pi^-)$, $2\phi/(\pi^+ + \pi^-)$, and $(\Omega^+ + \Omega^-)/(\pi^+ + \pi^-)$ ratios as a function of different event shape observables. For simplicity now onwards we refer these ratios as K_S^0/π , Λ/π , Ξ/π , ϕ/π , and Ω/π respectively.

Figure 44 shows a comparison of results from Monash, Monash NoCR, and Color Ropes tunes of PYTHIA 8

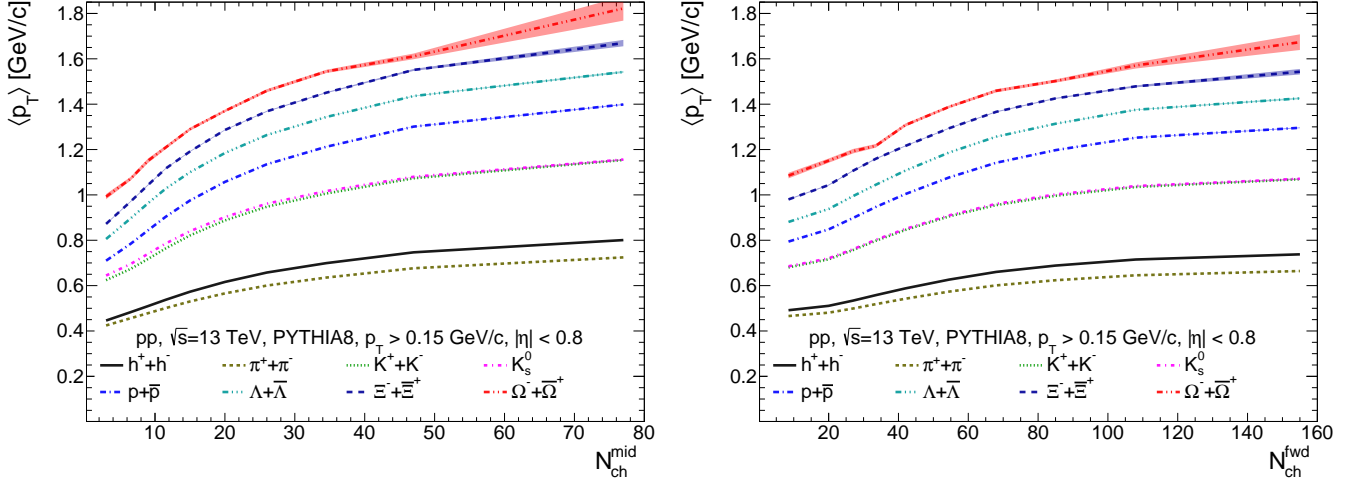


FIG. 36. Mean transverse momentum of all charged and identified hadrons as a function of charged-particle multiplicity in mid-pseudorapidity (left) and forward pseudorapidity (right) in pp collisions at $\sqrt{s} = 13$ TeV using PYTHIA8.

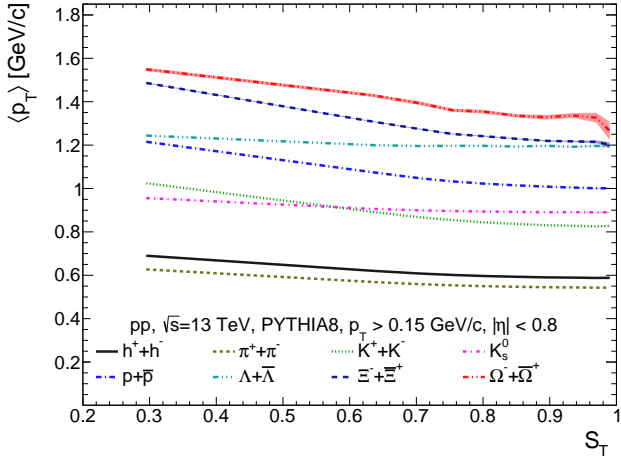


FIG. 37. Mean transverse momentum of all charged and identified hadrons as a function of transverse sphericity (S_T) in pp collisions at $\sqrt{s} = 13$ TeV using PYTHIA8.

with ALICE measurements of p_T -integrated strange hadrons to pion ratios measured in $|y| < 0.5$ as a function of charged-particle multiplicity density ($\langle dN_{ch}/d\eta \rangle$) obtained in $|\eta| < 0.5$ in pp collisions at $\sqrt{s} = 13$ TeV. The ALICE results show a rise in the ratios of strange hadrons to pions with the increase in $\langle dN_{ch}/d\eta \rangle$, which becomes significantly prominent for the hadrons with the higher number of valence strange quarks. Here, K_S^0/π does not show any rise with increase in $\langle dN_{ch}/d\eta \rangle$. In contrast, Ω/π , which has three valence strange quarks, shows the strongest rise with the increase in $\langle dN_{ch}/d\eta \rangle$. PYTHIA 8 with Color Ropes is able to reproduce the ALICE measurements of strange hadrons to pion ratios

quantitatively. On the contrary, PYTHIA 8 with Monash and Monash NoCR fail to explain the experimental measurements both qualitatively and quantitatively, except for K_S^0 . Henceforth, we shall limit our results for strange hadron to pion ratios only to PYTHIA 8 Color Ropes.

Figure 45 shows the relative production rate of particle containing strange quarks measured using the Λ/π , Ξ/π , Ω/π ratios as a function of charged-particle multiplicity measured in the mid-pseudorapidity (N_{ch}^{mid}) (left panel) and forward pseudorapidity (N_{ch}^{fwd}) (right panel) region in pp collisions at $\sqrt{s} = 13$ TeV using PYTHIA8. From Fig. 45, it is observed that these integrated yield ratios increase with charged-particle multiplicity. This effect is commonly called “strangeness enhancement” in the heavy-ion community.

One more intriguing observation is that the strangeness enhancement effect is proportional to the strangeness content of the hadrons. From Fig. 45 it is observed that the rate of enhancement of these ratios with multiplicity is higher for triply-strange Ω hyperons, and it gradually decreases for hadrons containing two and one strange quark quantum number, such as Ξ and Λ , etc. Although ϕ has no net strangeness quantum number, a slight increasing behavior of ϕ to pions ratios is observed at lower forward multiplicity classes, N_{ch}^{fwd} . This implies that the ϕ particle production can not be described solely by considering net strangeness or the number of strange quark constituents. In addition, the left panel of Fig. 45 indicates a decrease in the strange to non-strange ratios in the first charged-particle multiplicity bins. This could be attributed to the event selection bias developed while selecting charged-particle multiplicity in the mid-pseudorapidity region. Figure 45 depicts the enhancement effect reaches a saturation behavior towards $N_{ch}^{mid}/\langle N_{ch}^{mid} \rangle \geq 2$ for all considered hadrons ratios, while it is found to be particle species dependent

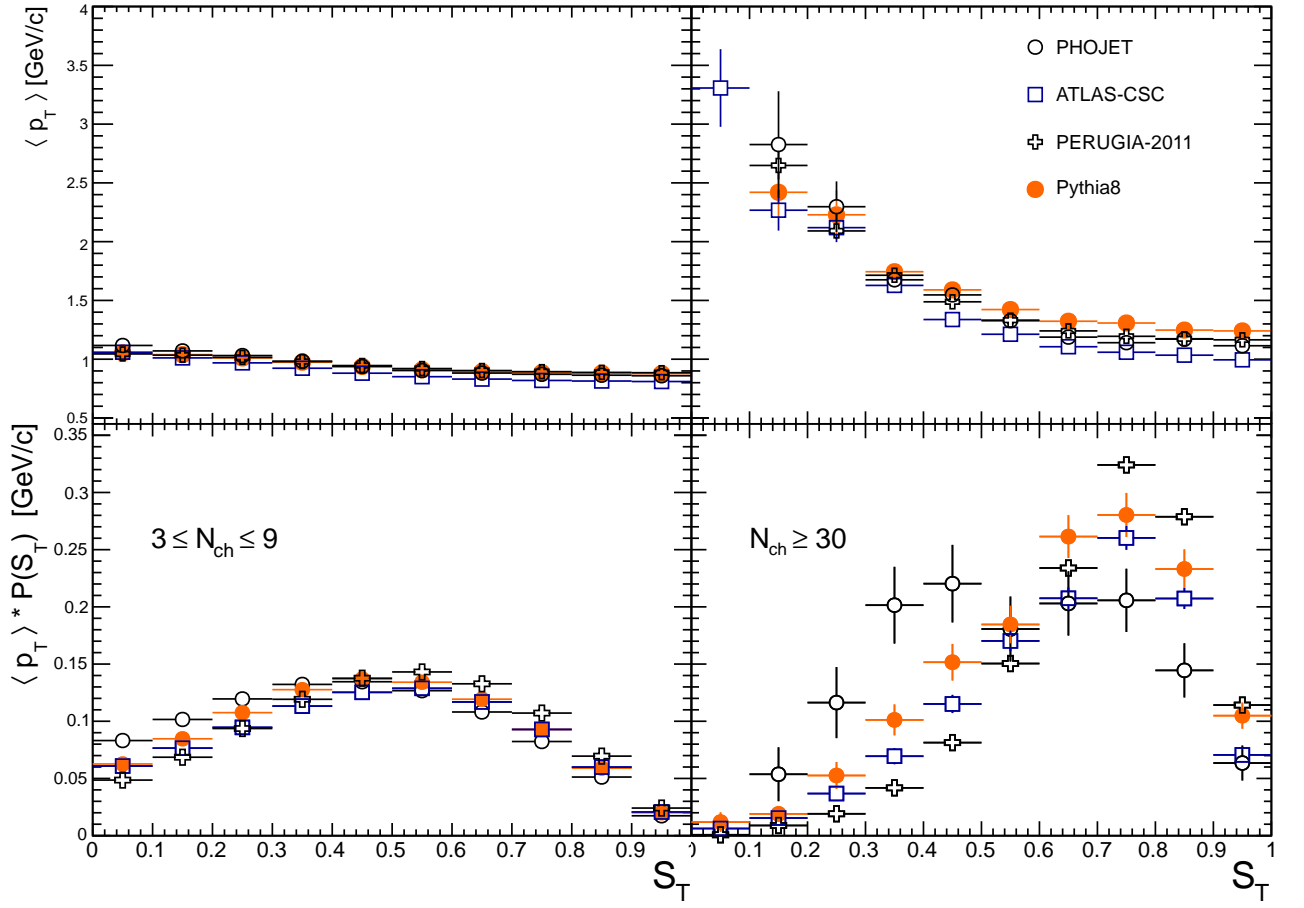


FIG. 38. Mean transverse momentum of all charged particles as a function of transverse sphericity (S_T) for two multiplicity bin $3 \leq N_{ch} \leq 9$ (left) and $N_{ch} \geq 30$ in minimum bias pp collisions at $\sqrt{s} = 7$ TeV obtained using four different MC generator: PHOJET, ATLAS-CSC, PERUGIA-2011, and PYTHIA8 is shown in the top panel. The bottom panel shows the contribution of each sphericity bin to the final $\langle p_T \rangle$ [44]

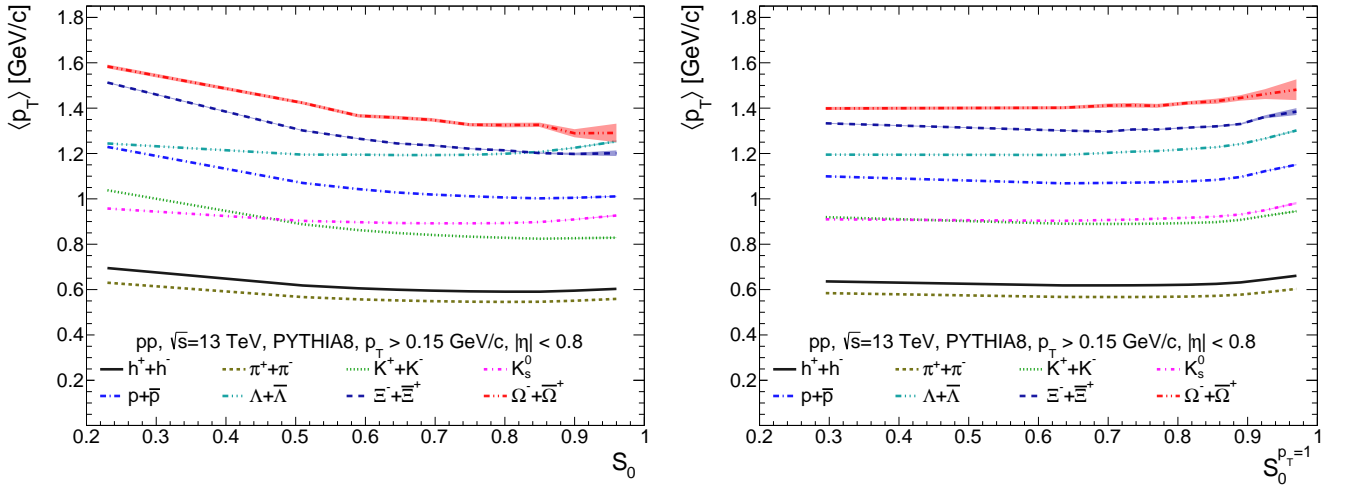


FIG. 39. Mean transverse momentum of all charged and identified hadrons as a function of p_T -weighted transverse sphericity (S_0) (left) and unweighted transverse sphericity ($S_0^{p_T=1}$) (right) in pp collisions at $\sqrt{s} = 13$ TeV using PYTHIA8.

for N_{ch}^{fwd} . Therefore, it can be inferred that the event selection with charged-particle multiplicity measured

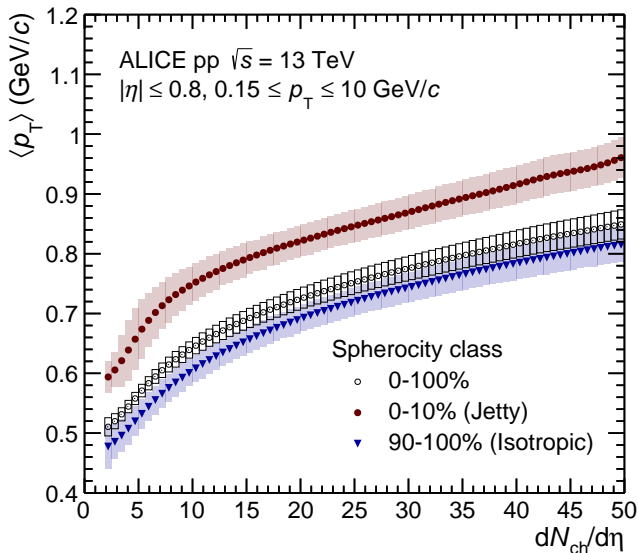


FIG. 40. Average transverse momentum ($\langle p_T \rangle$) as a function of event multiplicity for S_0 -integrated (0-100%), jetty (0-10%) and isotropic (90-100%) events in pp collisions at $\sqrt{s} = 13$ TeV with ALICE [25].

in different windows of pseudorapidity regions plays an important role in describing the dynamics of the strange hadron production. Furthermore, Fig. 46 shows the K_S^0/π , Λ/π , Ξ/π , ϕ/π , and Ω/π ratios as a function of number of multi-partonic interactions in pp collisions at $\sqrt{s} = 13$ TeV using PYTHIA8. From Fig. 46, it is observed that the strange production in PYTHIA8 using Color Ropes and CR is sensitive to MPI in pp collisions. Higher MPI refers to those events in pp collisions that have a larger number of final-state charged-particle multiplicities. Hence, the strange to non-strange ratios as a function of N_{mpi} show a similar trend as N_{ch}^{fwd} .

Figure 47 shows the strange to non-strange ratios as a function of S_0 (left panel) and $S_0^{p_T=1}$ (right panel) in pp collisions at $\sqrt{s} = 13$ TeV using PYTHIA8. From Fig. 47, it is observed that the K_S^0/π , Λ/π , Ξ/π , ϕ/π , and Ω/π ratios remain almost constant with S_0 and $S_0^{p_T=1}$. Furthermore, similar observation has also been observed for K_S^0/π , Λ/π , Ξ/π , ϕ/π , and Ω/π ratios as a function of S_T as shown in Fig. 48. So, in conclusion, we found that events having isotropic emission of particles have almost similar behavior of strange to non-strange ratios, with the events dominated by jets. The absence of S_0 , $S_0^{p_T=1}$ and S_T dependence on strangeness enhancement can be attributed to the application of $N_{ch}^{mid} > 10$ cut on the definitions of S_0 , $S_0^{p_T=1}$ and S_T . Therefore, the transverse sphericity, weighted and unweighted transverse sphericity event classifiers are inadequate to study the strangeness enhancement characteristics in pp collision using the PYTHIA8 model.

Figure 49 shows the p_T -integrated particle yield ra-

tios to pions normalized to corresponding value in high multiplicity (HM) events as a function of $S_0^{p_T=1}$ in pp collisions at $\sqrt{s} = 13$ TeV with ALICE. The high multiplicity events are determined based on the number of SPD tracklets ($N_{tracklets}^{|\eta| < 0.8}$) at midrapidity (left panel) and multiplicity in the V0 region (V0M) (right panel). In the left panel with the high multiplicity events selected based on $N_{tracklets}^{|\eta| < 0.8}$, within the systematic uncertainties, we observe an enhancement of particle yield ratios to pions as with the increase in $S_0^{p_T=1}$ which is absent in the right panel where the high-multiplicity events are selected based on V0M. Further, in the left panel, this enhancement is stronger for Ξ and weakest for protons. This indicates that, although the high multiplicity events have contributions from both isotropic events and multi-jet topologies, with $S_0^{p_T=1}$, one can choose isotropic events having large strange hadron production. However, this works well with event selection based on charged particles at midrapidity, where $S_0^{p_T=1}$ is estimated. This is because, $S_0^{p_T=1}$ selection on top (0-1)% N_{ch}^{mid} events probes a higher value of $\langle N_{mpi} \rangle$ as compared to similar $S_0^{p_T=1}$ selection on top (0-1)% N_{ch}^{fwd} events, as shown in Fig. 14.

Figure 50 shows the K_S^0/π , Λ/π , Ξ/π , ϕ/π , and Ω/π ratios as a function of R_T (upper left), R_T^{min} (upper right), and R_T^{max} (lower middle) in pp collisions at $\sqrt{s} = 13$ TeV using PYTHIA8. It is observed that these ratios remain almost constant with R_T , R_T^{min} , R_T^{max} . However, a slightly increasing trend is observed in the Ω/π ratios for R_T and $R_T^{max} \gtrsim 3.2$ within uncertainty. So, similar to sphericity and sphericity, the strangeness enhancement feature is also found to be marginal with the relative transverse activity classifiers.

The charged-particle flatnecity dependence of K_S^0/π , Λ/π , Ξ/π , ϕ/π , and Ω/π ratios is shown in Fig. 51 for pp collisions at $\sqrt{s} = 13$ TeV using PYTHIA8. It is interesting to note that these ratios tend to increase as a function of $(1-\rho_{ch})$ for all considered strange particles, except for K_S^0 . A rapid increase in the slope of the ratios is observed in Fig. 51 for the lower values of ρ_{ch} ($0.18 \lesssim \rho_{ch} \lesssim 0.36$) compared to the higher values of ρ_{ch} ($0.36 \lesssim \rho_{ch} \lesssim 0.7$). It is found that the rate of increase of the strange to non-strange particle ratios is strange quantum number dependent; the triple-strange baryons, such as Ω , have more slope compared to the single and double strange baryons, such as Ξ , and Λ .

The enhanced production of strangeness with different event classifiers can be further probed with a comparison of the double ratio of strange-to-non-strange hadrons, where the ratio is scaled with the same observable in minimum bias collisions. This study is explicitly performed in Ref. [60].

D. Baryon-to-meson ratios and radial flow

In this section, we present the event shape observable dependence of baryon to meson ratios as a function of p_T in pp collisions at $\sqrt{s} = 13$ TeV using PYTHIA8. The

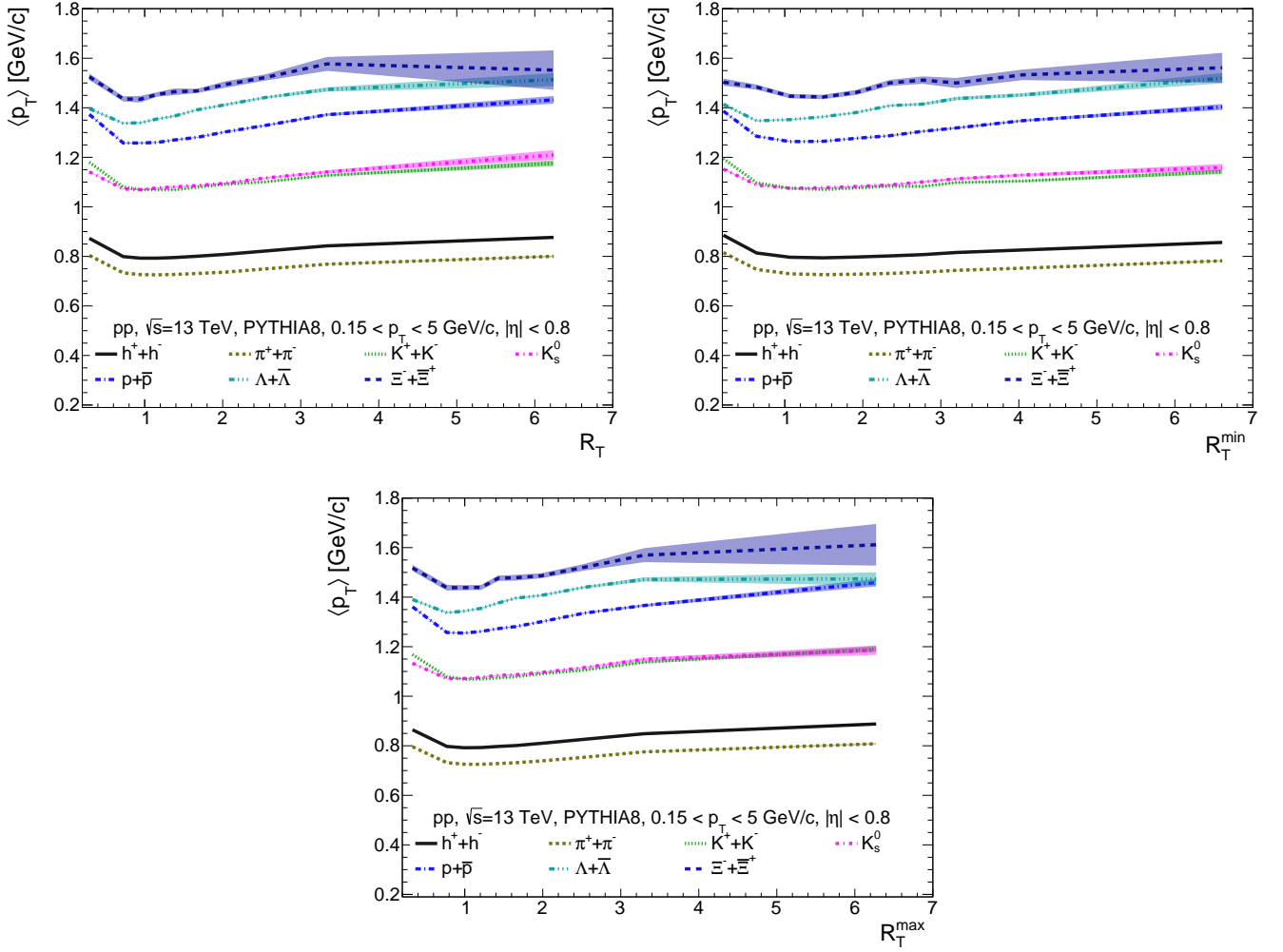


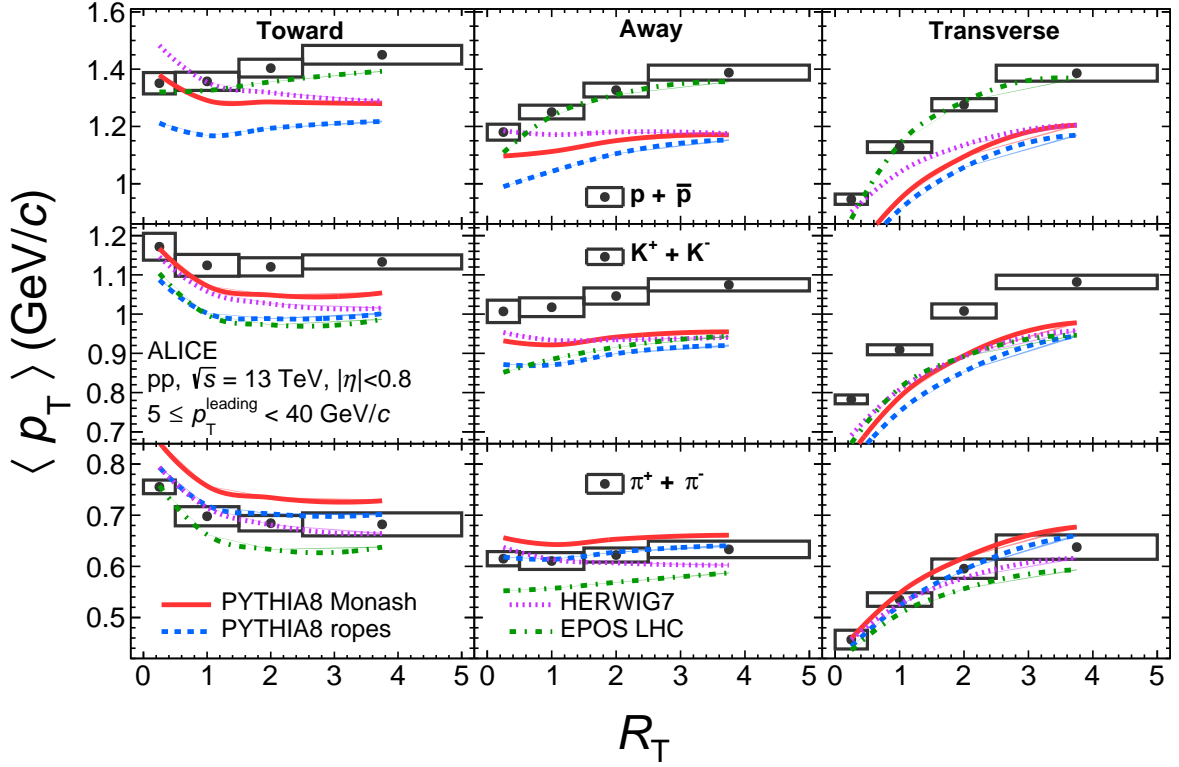
FIG. 41. Mean transverse momentum of all charged and identified hadrons as a function of R_T (top), R_T^{\min} (upper right), and R_T^{\max} (bottom) in pp collisions at $\sqrt{s} = 13$ TeV using PYTHIA8.

particle ratios as a function of p_T are the consequence of the transverse momentum spectra of the corresponding particle. Any modification that occurs in the particle ratios as a function of the event shape observables is simply due to the spectral shape modification as a function of the corresponding event shape. It is observed that in heavy-ion collisions, the enhancement in baryon-to-meson ratios at intermediate p_T can be explained due to the interplay between the collective motion of the system and the hadronization mechanism. Furthermore, the amplitude and the position of the peak observed in baryon-to-meson ratios indicate the strength of the radial flow [143]. However, such enhancement is also observed in pp collisions using PYTHIA8 due to the CR mechanism introduced in PYTHIA8 along with MPI. It is observed that the microscopic CR hadronization mechanism, along with MPI, suggests the flow-like features in pp collisions [142].

The charged-particle multiplicity dependence study of baryon-to-meson ratios provides information on radial flow as a function of charged-particle multiplicity. This motivates us to study baryon-to-meson ratios as a function of p_T for other event shape observables such as the number of multi-partonic interactions, transverse sphericity, sphericity, relative activity classifier, and charged-particle flattnicity. Thus, this study provides an understanding of the radial flow as a function of these event activities.

In the present study, in baryon-to-meson ratios we mainly investigate $(p + \bar{p})/(\pi^+ + \pi^-)$, $(\Lambda + \bar{\Lambda})/2K_S^0$, and $(p + \bar{p})/(\phi + \bar{\phi})$ ratios as a function of p_T . For simplicity now onwards we refer these ratios as p/π , Λ/K_S^0 , and p/ϕ respectively.

Figure 52 shows the p_T -differential p/π (upper left), Λ/K_S^0 (upper right), and p/ϕ (lower middle) ratios in



8

FIG. 42. Average transverse momentum ($\langle p_T \rangle$) for charged protons, kaons and pions, shown from upper to lower panels, measured in different topological regions as a function of R_T in pp collisions at $\sqrt{s} = 13$ TeV with ALICE [51]. Model comparisons for the corresponding measurements are shown using Ropes and Monash tunes of PYTHIA8 along with HERWIG7 and EPOS LHC [51].

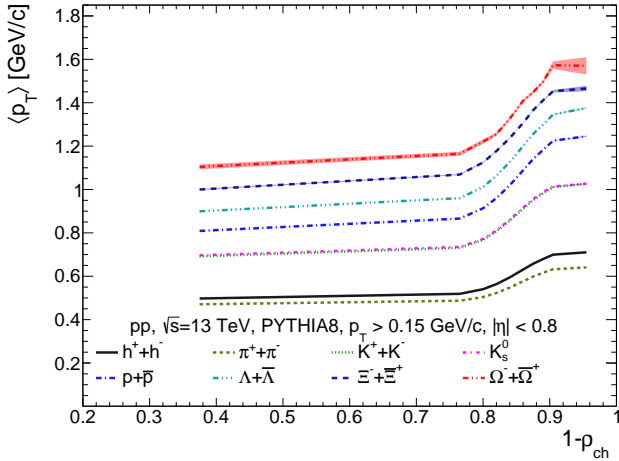


FIG. 43. Mean transverse momentum of all charged and identified hadrons as a function of charged-particle flatnecity (ρ_{ch}) in pp collisions at $\sqrt{s} = 13$ TeV using PYTHIA8.

inelastic pp collisions for different mid-pseudorapidity

charged-particle multiplicity classes at $\sqrt{s} = 13$ TeV using PYTHIA8. The mid-pseudorapidity charged-particle multiplicity class selections are shown in the top panel of Fig. 6. The p/π and Λ/K_S^0 ratios exhibits a bump structure in $1.5 \lesssim p_T \lesssim 8$ GeV/c. This bump structure gradually increases with increasing charged-particle multiplicity. It is observed that the position of the peak shifts towards higher momentum when one goes from the lowest multiplicity to the highest multiplicity classes. The peak reaches a maximum of about 0.28 for p/π and 0.4 for Λ/K_S^0 at $p_T \approx 3.5$ GeV/c for highest multiplicity class. Thus, Fig. 52 shows a mass effect in the baryon to meson ratios since the Λ/K_S^0 ratios exhibit a larger bump than p/π ratios for the highest multiplicity classes. Further, the distinction in the baryon-meson ratios for different multiplicity classes is visible towards high p_T , i.e., $p_T \gtrsim 3.0$ GeV/c as shown in Fig. 52.

However, no such bump structure at intermediate p_T is observed in p/ϕ ratios using PYTHIA8 with the same MPI and CR tune. Thus, we found that particles having similar masses but different quark content have different particle ratios. The lower middle panel of Fig. 52 shows the p/ϕ ratios decrease as a function of p_T . The p/ϕ

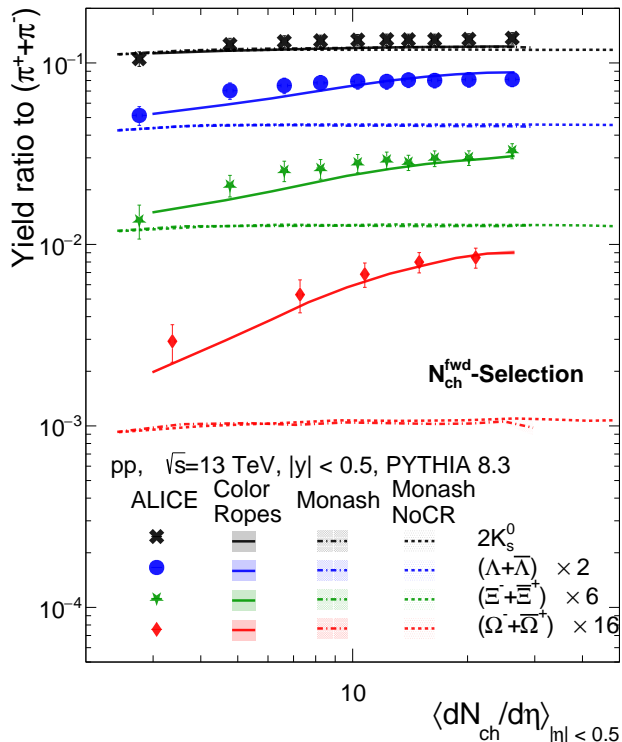


FIG. 44. p_T -integrated yield ratios of strange hadrons to pions measured in $|y| < 0.5$ versus average charged-particle multiplicity density ($\langle dN_{ch}/d\eta \rangle$) measured at $|\eta| < 0.5$ in pp collisions at $\sqrt{s} = 13$ TeV using Monash, Monash NoCR and Color Ropes tunes of PYTHIA 8 [60]. The results from PYTHIA 8 are compared with similar measurements at ALICE [140].

ratios greater than 1 indicate more protons are produced as compared to the ϕ mesons. It is observed that there is a clear charged-particle multiplicity dependence effect present in the p/ϕ ratios as a function of p_T . The p/ϕ ratios increase with an increase in charged-particle multiplicity classes in pp collisions. Moreover, we found that in the highest charged-particle multiplicity classes the p/ϕ ratios are almost independent of p_T . This indicates that spectral shapes only depend upon the particle mass, which is the main variable for determining the spectral shapes in most of the hydrodynamic models. This could be a possible signature of radial flow present in the system. It is important to note that although the spectral shape may change with the interactions present in the hadronic phase and it could modify the picture differently. However, it is believed that it will affect differently for protons and ϕ mesons as compared to the short-lived resonances.

Figure 53 shows the p/π (upper left), Λ/K_S^0 (upper right), and p/ϕ (lower middle) ratios as a function of p_T in pp collisions for different forward pseudorapidity

charged-particle multiplicity classes. In Fig. 53, the forward pseudorapidity charged-particle multiplicity selections are according to the V0 detector acceptance, and class selections are displayed in the right panel of Fig. 6. Since the charged-particle multiplicity at mid rapidity (N_{ch}^{mid}) follows a linear correlation with the charged-particle multiplicity at forward rapidity (N_{ch}^{fwd}), it is expected, the baryon to meson ratios in N_{ch}^{fwd} follows the similar behavior with N_{ch}^{mid} . It is observed that although the p/π ratios at N_{ch}^{fwd} has similar trend with N_{ch}^{mid} , a slight variation is observed towards the low p_T ($p_T \lesssim 0.8$ GeV/c). The p/π ratios for N_{ch}^{mid} at low p_T are higher for the lowest multiplicity class, and they decrease with charged-particle multiplicity as shown in Fig. 52. While p/π ratios have nearly the same value for forward multiplicity classes at low p_T . We observe that strange-hadron sector Λ/K_S^0 ratios follow a similar trend as p/π ratios. However, the increasing trend of baryon-to-meson ratios with charged-particle multiplicity is clearly observed for all p_T bins. Furthermore, the p/ϕ ratios in forward pseudorapidity charged-particle multiplicity show a decreasing trend as a function of the p_T . However, the charged-particle multiplicity dependence in p/ϕ ratios is a bit diluted in the forward pseudorapidity region, whereas a clear multiplicity dependence was observed for mid-pseudorapidity charged-particle multiplicity classes.

Figure 54 shows the p/π (upper left), Λ/K_S^0 (upper right), and p/ϕ (lower middle) ratios as a function of p_T for different N_{mpi} classes. The N_{mpi} class selections for the minimum bias sample are displayed in Fig. 7. It is observed that events with the highest number of multi-partonic interactions show higher p/π ratios at intermediate p_T and the ratio decreases with a decrease in N_{mpi} . Since N_{mpi} has a positive correlation with the N_{ch}^{mid} and N_{ch}^{fwd} , it is expected the evolution of baryon-to-meson ratios with the number of MPI will be qualitatively similar to the charged-particle multiplicity. However, it is evident to note that the events with less number of multi-partonic interactions (i.e., (70-100)% class) do not exhibit the bump structure at intermediate p_T , it stays almost constant with p_T . Thus, events with less MPI activity do not show flow-like patterns in pp collisions. Furthermore, the lower middle panel of Fig. 54 shows p/ϕ ratios decrease as a function of p_T for different N_{mpi} classes. It is observed that the p/ϕ ratios as a function of a N_{mpi} are similar to N_{ch}^{fwd} , except the evolution follows a different trend in the lower MPI classes.

Apart from charged-particle multiplicity and MPI activity, we also investigate the p_T -dependent baryon to meson ratios for the other event classifiers such as transverse sphericity (S_T), transverse spherocity (S_0), relative activity classifier (R_T) and charged-particle flattenicity (ρ_{ch}).

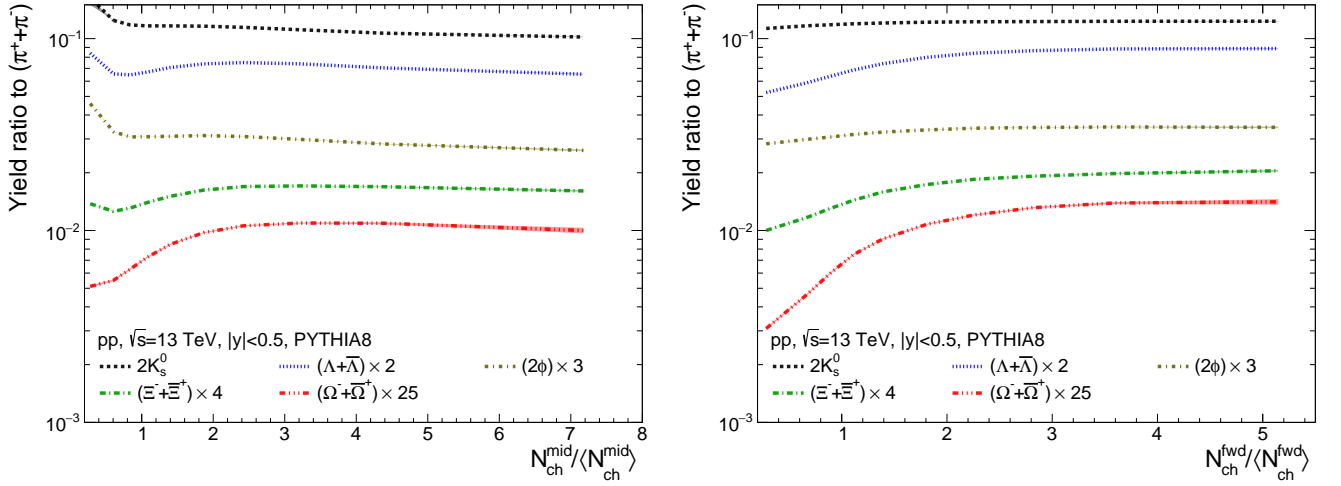


FIG. 45. p_T -integrated yield ratios to pions ($\pi^+ + \pi^-$) measured in $|y| < 0.5$ as a function of charged-particle multiplicity measured in the mid-pseudorapidity ($N_{\text{ch}}^{\text{mid}}/\langle N_{\text{ch}}^{\text{mid}} \rangle$) (left panel) and forward pseudorapidity ($N_{\text{ch}}^{\text{fwd}}/\langle N_{\text{ch}}^{\text{fwd}} \rangle$) (right panel) in pp collisions at $\sqrt{s} = 13$ TeV using PYTHIA8 [60].

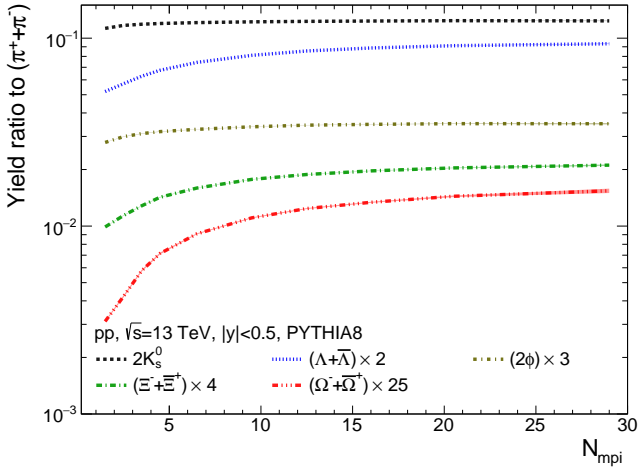


FIG. 46. p_T -integrated yield ratios to pions ($\pi^+ + \pi^-$) measured in $|y| < 0.5$ as a function of number of multi-partonic interactions (N_{mpi}) in pp collisions at $\sqrt{s} = 13$ TeV using PYTHIA8 [60].

Figure 55 presents the p/π (upper left), Λ/K_S^0 (upper right), and p/ϕ (lower middle) ratios as a function of p_T for different S_T classes. The S_T class selections are shown in the left panel of Fig. 12. From Fig. 12 it is observed that the isotropic events p/π ratios show an enhancement feature at the intermediate p_T , while jetty events p/π ratios are flat as a function of p_T . However, unlike the charged-particle multiplicity and/or the number of multi-partonic interactions, the dependence of transverse sphericity classes on p/π ratios is found to be weak. Similar observation is also seen for Λ/K_S^0 with p_T for dif-

ferent S_T classes. Moreover, the lower middle panel of Fig. 55 shows p/ϕ ratios decrease as a function of p_T for various S_T classes. Interestingly, it is observed that for (70-100)% S_T class the p/ϕ ratios have a minimum value with $p_T \lesssim 2.0$ and it reaches a maximum value for $p_T \gtrsim 2.0$ among all S_T classes.

Figure 56 highlights p/π (upper left), Λ/K_S^0 (upper right), and p/ϕ (lower middle) as a function of p_T for different S_0 classes. The S_0 class selections are shown in the left panel of Fig. 12. The p_T -differential baryon-to-meson ratios show higher enhancement for isotropic events compared to jetty events at intermediate p_T in the minimum bias sample. We found that the p/π and Λ/K_S^0 ratios decrease rapidly for the highest (0-0.1)% sphericity class towards high p_T . The lower middle panel of Fig. 56 shows p/ϕ ratios decrease as a function of p_T for various S_0 classes. Interestingly, it is observed that for top central S_0 classes the p/ϕ ratios are constant with $p_T \lesssim 1.0$ within uncertainties and then it decreases with p_T . In addition, it is observed that events with jetty type are found to have higher p/ϕ value for $p_T \gtrsim 2.0$, while it is minimum for $p_T \lesssim 2.0$. Thus, with the transverse sphericity event classifiers, one can separate the events which have flow-like behavior. Figure 57 shows p/π (upper left), Λ/K_S^0 (upper right), and p/ϕ (lower middle) ratios as a function of p_T for different $S_0^{p_T=1}$ classes. The $S_0^{p_T=1}$ class selections are shown in the right panel of Fig. 12. The p_T -differential baryon to meson ratios show higher enhancement for isotropic events compared to jetty events at intermediate p_T in the minimum bias sample. However, it is important to note that unlike S_0 , $S_0^{p_T=1}$ the rapid decrease of the p/π ratios at (0-0.1)% sphericity class is towards high p_T is not observed. In addition, the p/ϕ ratios decrease with p_T and overall all sphericity event classes predict the

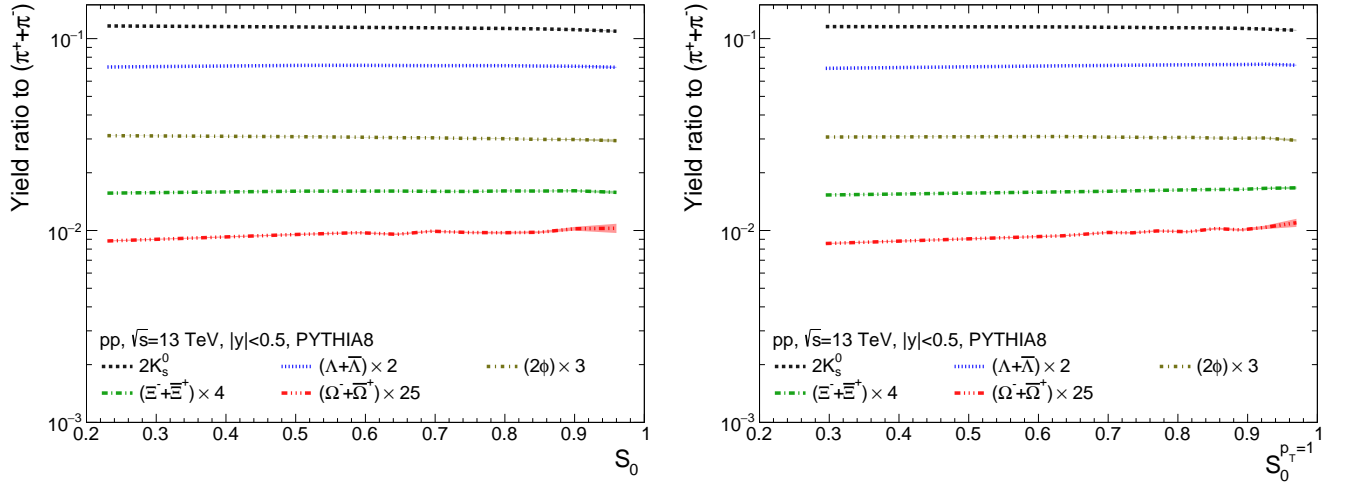


FIG. 47. p_T -integrated yield ratios to pions ($\pi^+ + \pi^-$) measured in $|y| < 0.5$ as a function of p_T -weighted transverse sphericity (S_0) (left panel) and unweighted transverse sphericity ($S_0^{p_T=1}$) (right panel) in pp collisions at $\sqrt{s} = 13$ TeV using PYTHIA8 [60].

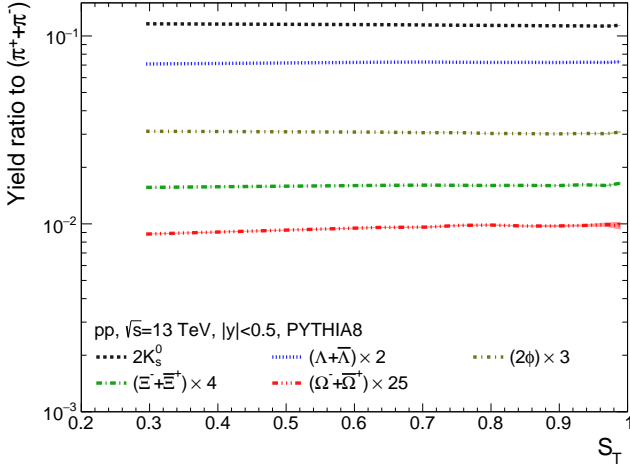


FIG. 48. p_T -integrated yield ratio to pions ($\pi^+ + \pi^-$) measured in $|y| < 0.5$ as a function of transverse sphericity (S_T) in pp collisions at $\sqrt{s} = 13$ TeV using PYTHIA8 [60].

same p/ϕ ratios as a function of p_T .

In Fig. 58, we show that ALICE measurements for the p_T -differential p/π , Λ/K_S^0 , and Ξ/ϕ ratios for the extreme classes of $S_0^{p_T=1}$ of top 0-1% multiplicity class measured by $N_{\text{tracklets}}^{|\eta|<0.8}$ in pp collisions at $\sqrt{s} = 13$ TeV. A clear impact of $S_0^{p_T=1}$ selection can be observed for the p/π ratios. In contrast, for Λ/K_S^0 , and Ξ/ϕ ratios, the impact of $S_0^{p_T=1}$ selection can only be observed within the systematic uncertainties. PYTHIA 8 Monash results qualitatively reproduce the data, while Ropes shows both

qualitative and quantitative agreement with the experimental data.

Now, using the charged-particle multiplicity information we investigate the p_T -dependent the baryon to meson ratios for another underlying event activity called relative transverse activity classifier (R_T) in the transverse region as depicted in Fig. 15. The upper left panel of Fig. 59 shows the p/π ratios as a function of p_T for different R_T classes. The R_T class selections are shown in the upper left panel of Fig. 17. From Fig. 59 it is observed that p/π ratios does not exhibit the characteristics enhancement at intermediate p_T in events with large R_T ($R_T \gtrsim 3.5$) and very small R_T ($R_T \lesssim 1.0$) in minimum bias pp collisions. This effect could be due to the selection bias attributed to wide-angle gluon emissions, which creates jets that populate the transverse region. However, a small hint of enhancement can be found at the intermediate R_T values ($1.0 \lesssim R_T \lesssim 3.5$). The upper right panel of Fig. 59 shows the Λ/K_S^0 ratio as a function of p_T for the transverse region. It is interesting to note that unlike p/π , Λ/K_S^0 shows the characteristics enhancement at intermediate p_T in events with all values of R_T ($R_T \gtrsim 0.8$) except the lowest relative activity classifier class ($R_T \lesssim 0.8$). The lower middle panel of Fig. 59 shows the p/ϕ ratios as a function of p_T for the transverse region. Here, the slope of p/ϕ ratios is smaller for all R_T classes compared to other event shape estimators discussed above. The evolution of p/ϕ ratios with p_T for various R_T classes changes around $p_T \approx 2.0$ GeV/c.

Moreover, the p/π , Λ/K_S^0 , and p/ϕ ratios for R_T^{max} , R_T^{min} regions is shown in Fig. 60 and 61, respectively. The R_T^{max} , R_T^{min} class selections are shown in the upper right and lower middle of Fig. 17, respectively. Similar to R_T , the behavior of p/π , Λ/K_S^0 , and p/ϕ ratios have similar behavior for R_T^{max} and R_T^{min} .

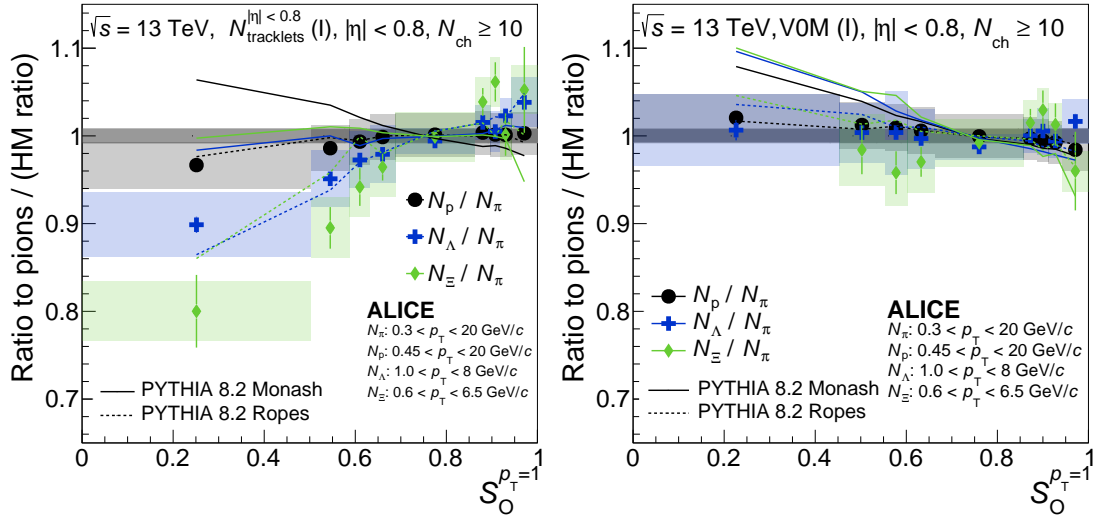


FIG. 49. Ratio of particle yield to pions as a function of unweighted transverse sphericity in high multiplicity events based $N_{\text{tracklets}}^{|η|<0.8}$ (left panel) and VOM (right panel) in pp collisions at $\sqrt{s} = 13$ TeV with ALICE [53].

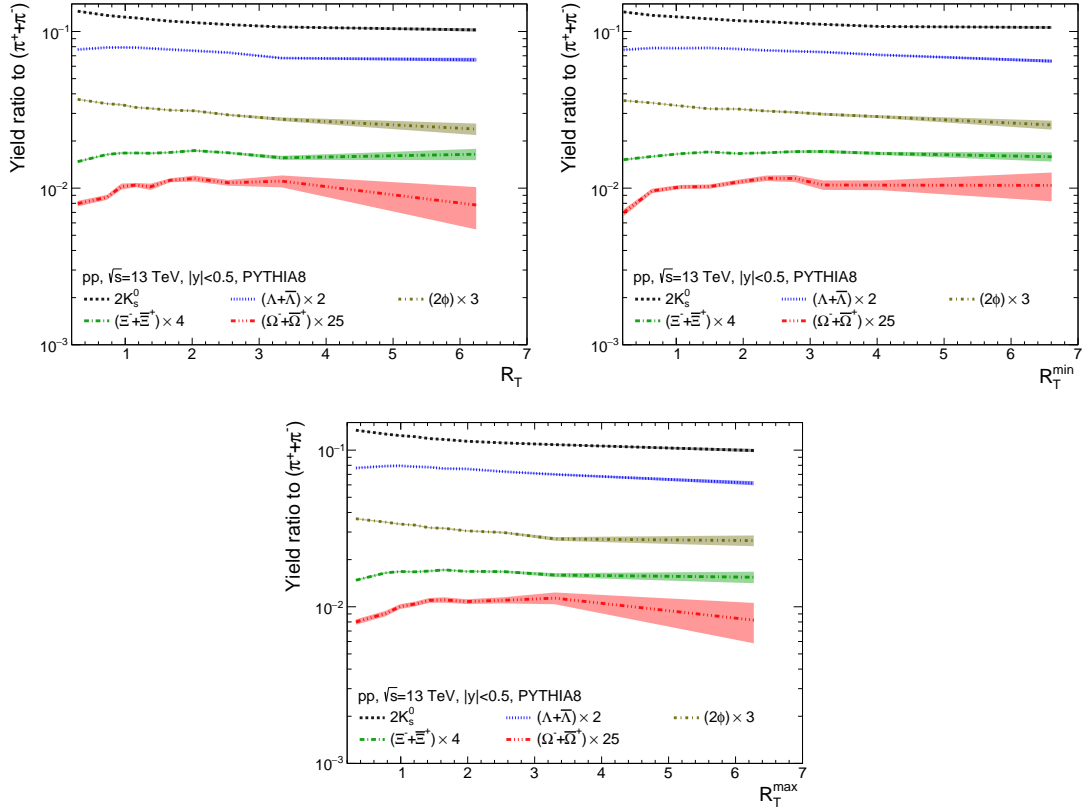


FIG. 50. p_T -integrated yield ratio to pions ($\pi^+ + \pi^-$) measured in $|y| < 0.5$ as a function of R_T (upper left), R_T^{\min} (upper right), and R_T^{\max} (lower middle) in pp collisions at $\sqrt{s} = 13$ TeV using PYTHIA8 [60].

Figure 62 shows the p_T dependence of K/π (upper panel) and p/π (lower panel) ratios as a function of R_T

in pp collisions at $\sqrt{s} = 13$ TeV with ALICE along with comparisons from EPOS LHC and HERWIG7. The K/π ratios show similar behavior in both toward and away

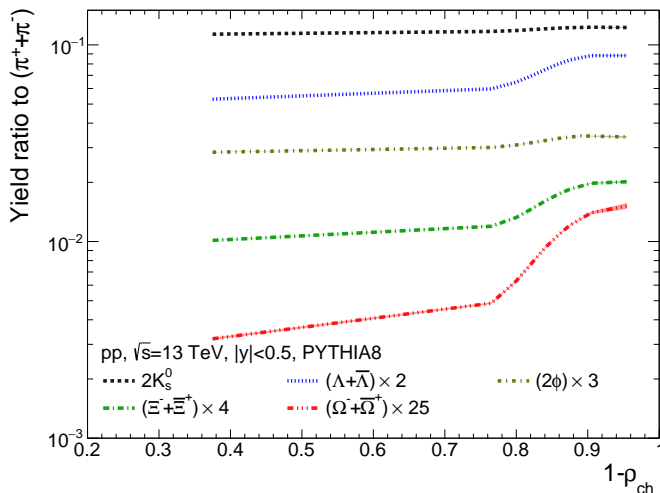


FIG. 51. p_T -integrated yield ratio to pions ($\pi^+ + \pi^-$) measured in $|y| < 0.5$ as a function of charged-particle flattnicity (ρ_{ch}) in pp collisions at $\sqrt{s} = 13$ TeV using PYTHIA8 [60].

regions, which increases with an increase in R_T . However, the K/π ratios increase with a decrease in R_T or UE activity in the transverse region. In the lower panel, one finds that with an increase in R_T , the contribution of UE activity in both toward and away regions for $p_T > 1$ GeV/c increases, leading to a rise in p/π ratios. This increase in p/π ratios with the increase in UE activity can be attributed to a growth in collective radial flow. Further, the p/π ratios in the transverse regions have a mild dependence on R_T . Here, towards the lower p_T region, an impression of proton production with respect to pions is observed for the events with larger UE activity. This can be attributed to the radial flow effects, which boost the protons towards higher p_T regions. Further, a jet hardening effect with an increase in transverse multiplicity is also visible for the high- R_T events which shifts the peak of p/π ratios of high R_T events towards a higher p_T as compared to the events with low R_T events [144].

The definition of flattnicity (Eq. (21)) indicates that such an event classifier strongly depends upon the selection of charged-particle multiplicity in the forward pseudorapidity region. The limit $(1 - \rho_{ch}) \rightarrow 1$ correspond to high multiplicity events and $(1 - \rho_{ch}) \rightarrow 0$ correspond to low multiplicity events. The correlation of charged-particle flattnicity event shape observable with N_{mpi} is shown in Fig. 20. One interesting point is to note the correlation between $(1 - \rho_{ch})$ rises sharply with N_{mpi} after 0.7 indicating the flattnicity serves as a better tool among all event classifiers to separate the isotropic (soft) and jetty (hard) events. Figure 63 illustrates the p/π (upper left), Λ/K_S^0 (upper right), and p/ϕ (lower middle) ratios as a function of p_T using $(1 - \rho_{ch})$ classes. All these ratios for different $(1 - \rho_{ch})$ classes present a similar feature with a decreasing trend

after $p_T \gtrsim 2 - 3$ GeV/c. It is observed that for the top central $(1 - \rho_{ch})$ classes we see an enhancement at intermediate p_T both for p/π and Λ/K_S^0 ratios. These characteristics of enhancement decrease towards the lowest $(1 - \rho_{ch})$ classes. The value of Λ/K_S^0 ratios is higher than p/π ratios for $(1 - \rho_{ch})$ classes. The lower middle panel of Fig. 63 shows the p/ϕ ratios decrease as a function of p_T , and a charged-particle flattnicity dependence effect is present in the p/ϕ ratios. The p/ϕ ratios increase with increase in the $(1 - \rho_{ch})$ classes. Moreover, we found that at low p_T ($\lesssim 1.0$ GeV/c) of highest charged-particle flattnicity classes, the p/ϕ ratios are almost independent of p_T indicating a possible signature of radial flow in the system. The (0-0.1)% $(1 - \rho_{ch})$ class in minimum bias pp samples selects events with an isotropy event topology, and (70-100)% selects events having more jets. Thus, from Fig. 63 it is observed that using the charged-particle flattnicity event classifier, we can separate the isotropic and jetty events.

Figure 64 shows the p_T dependence of proton to pion (p/π) (upper) and kaon to pion (K/π) (lower) ratios for different classes of flattnicity in minimum bias (left) and (0-1)% V0M class (right) in pp collisions at $\sqrt{s} = 13$ TeV with ALICE [55]. In the lower panel, K/π increases with p_T , and event selection based on charged-particle flattnicity does not seem to play any role for both the minimum bias and (0-1)% V0M classes. However, for p/π , a clear distinction for the lowest and highest percentiles of flattnicity is observed for the minimum bias case, which is absent when the flattnicity-based event selection is performed for the (0-1)% V0M class. PYTHIA 8 with Monash is found to give a good qualitative agreement with the experimental data.

E. Particle correlations and anisotropic flow

So far, we have discussed the sources of collective radial expansion, also known as the radial flow, of the system formed in collider experiments. In this section, we discuss anisotropic flow, which is one of the major contributors to the collectivity of the system and is mostly driven by the geometry and fluctuations of the collision overlap region. The anisotropic flow of the system can be quantified by the coefficients of the Fourier expansion of the azimuthal distribution of particles in the final state, given as follows [145].

$$\frac{dN}{d\phi} \propto 1 + 2 \sum_{n=1}^{\infty} v_n \cos[n(\phi - \psi_n)] \quad (34)$$

Here, v_n and ψ_n are the n th order anisotropic flow coefficients and symmetry plane angles, respectively. v_1 , v_2 , and v_3 , etc., are called directed, elliptic, and triangular flow, respectively. As the name suggests, the directed flow (v_1) quantifies the collective sideward deflection of

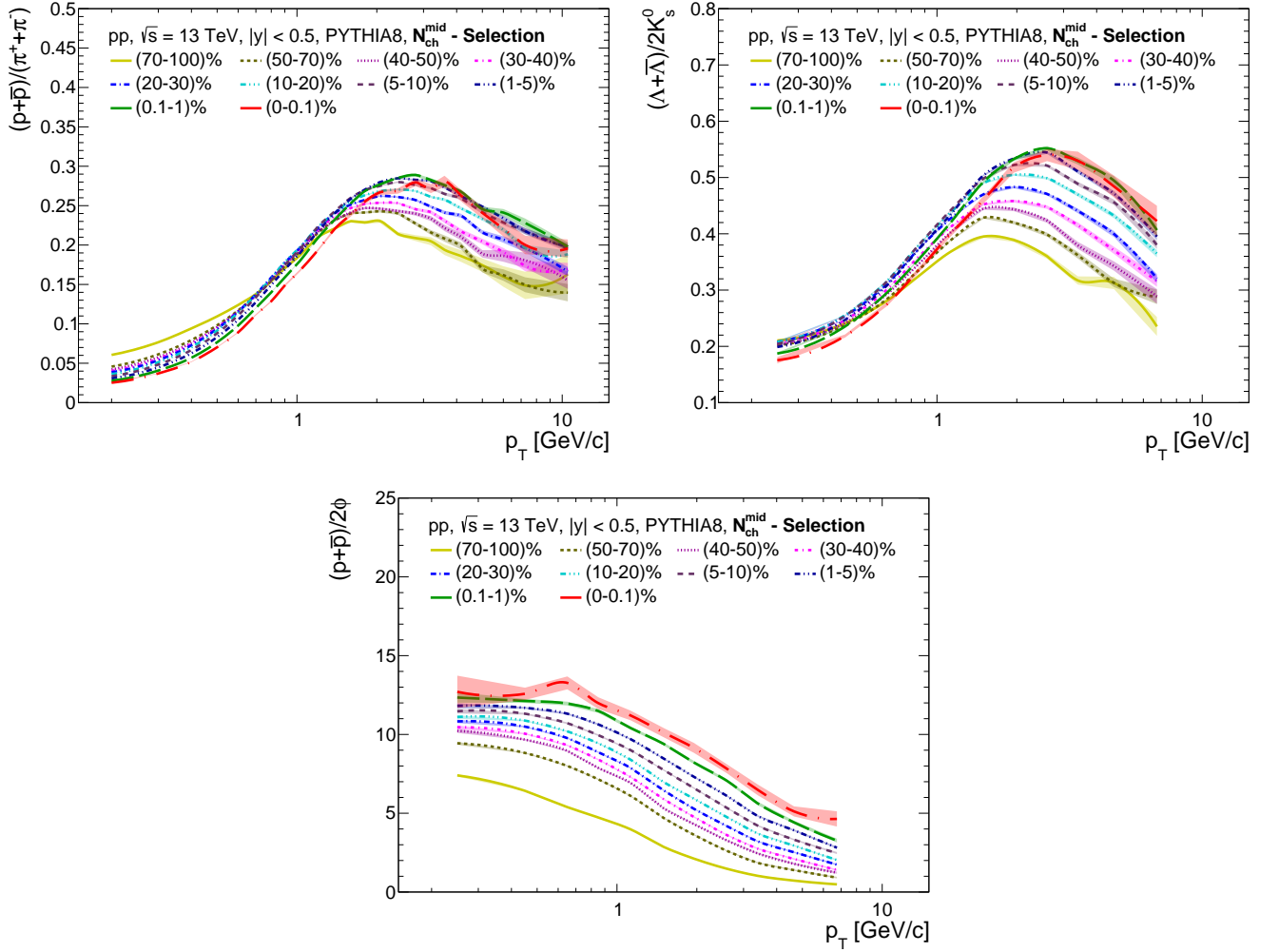


FIG. 52. p_T -differential p/π (upper left) and Λ/K_S^0 (upper right) and p/ϕ (lower middle) ratios measured in $|y| < 0.5$ for different mid-pseudorapidity charged-particle multiplicity (N_{ch}^{mid}) classes in pp collisions at $\sqrt{s} = 13$ TeV using PYTHIA8. The selection of events is based on N_{ch}^{mid} classes and shown in the right panel of Fig. 6.

particles with respect to the reaction plane [145, 146]. The contribution of v_1 in symmetric systems at the LHC energies is small [145]. In contrast, in non-central collisions, the collision overlap geometry is elliptic, leading to large values of v_2 in heavy-ion collisions. However, in small systems such as pp and p-Pb collisions, the density fluctuations dominate over the contribution of geometry in the final state flow. Further, the collectivity itself in small systems bears a big question mark, and thus, the study of anisotropic flow in pp and p-Pb collision systems is interesting. Figure 65 shows elliptic flow of mesons and (π^\pm , K^\pm , K_S^0) and baryons ($p+\bar{p}$, $\Lambda+\bar{\Lambda}$) with $|\eta| < 0.8$ in Pb-Pb, p-Pb and pp collisions [147]. The measurement is performed using a two-particle correlation method in different collision energies and multiplicity regions for the collision systems. The two-particle correlation method requires the estimation of the two-particle correlation function, which provides an estimation of the probability

of finding a pair of particles separated by a given pseudorapidity difference ($\Delta\eta$) and azimuthal angle difference ($\Delta\phi$). The one-dimensional two-particle correlation function can be defined as:

$$C(\Delta\phi) = \frac{dN_{pairs}}{d\Delta\phi} \propto \left[1 + 2 \sum_{n=1}^{\infty} v_{n,n}(p_T^a, p_T^b) \cos n\Delta\phi \right] \quad (35)$$

Here, $v_{n,n}$ is the two-particle flow coefficient. $v_{n,n}$ are symmetric with respect to p_T^a (transverse momentum of trigger particle) and p_T^b (transverse momentum of associated particle). $v_{n,n}$ can be calculated by the discrete

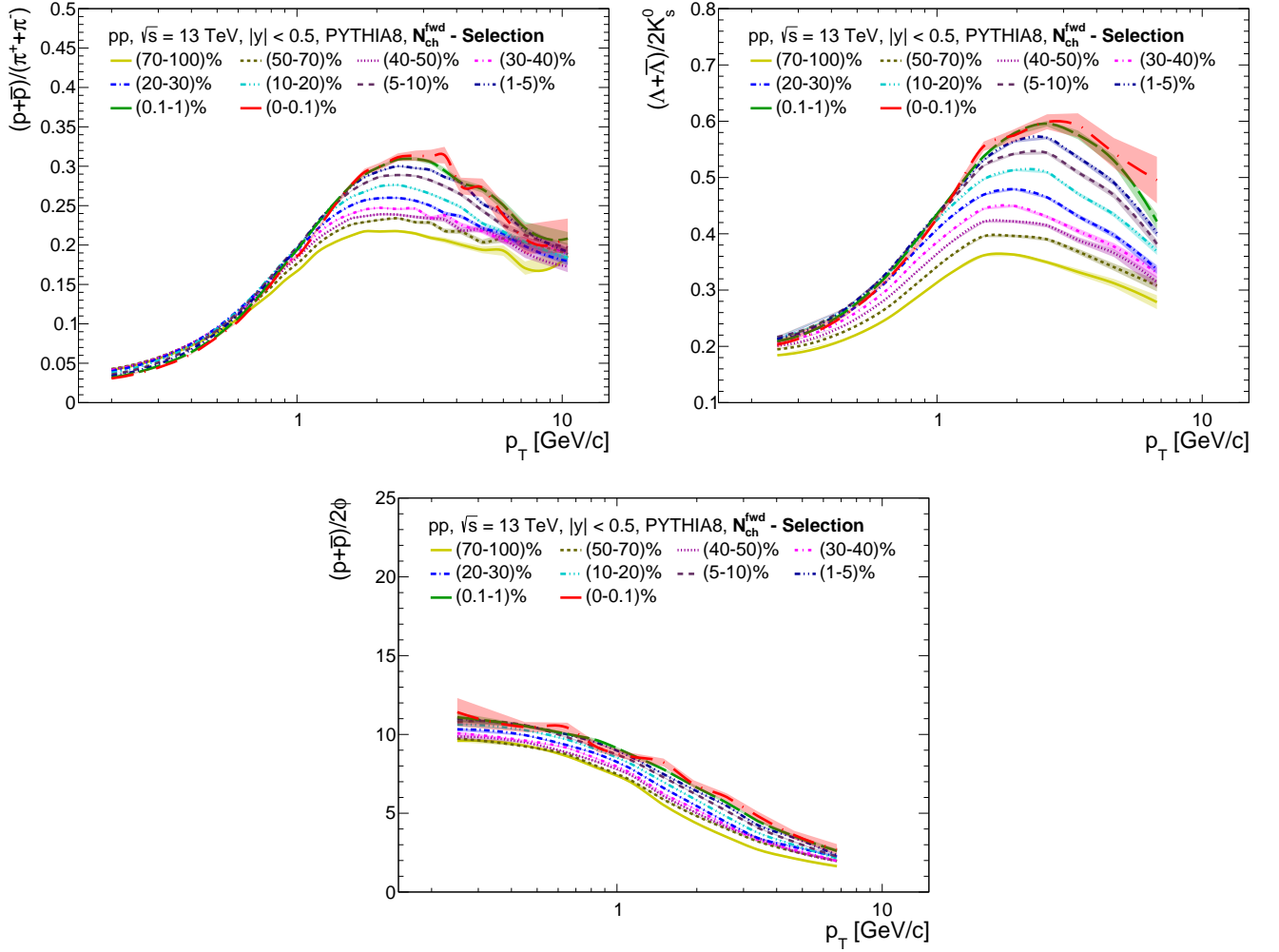


FIG. 53. p_T -differential p/π (upper left) and Λ/K_S^0 (upper right) and p/ϕ (lower middle) ratios measured in $|y| < 0.5$ for different forward pseudorapidity charged-particle multiplicity classes (N_{ch}^{fwd}) in pp collisions at $\sqrt{s} = 13$ TeV using PYTHIA8. The selection of events is based on N_{ch}^{fwd} classes and shown in the right panel of Fig. 6.

Fourier transformation using the following expression.

$$v_{n,n}(p_T^a, p_T^b) = \langle \cos n\Delta\phi \rangle = \frac{\sum_{m=1}^N \cos(n\Delta\phi_m) C(\Delta\phi_m)}{\sum_{m=1}^N C(\Delta\phi_m)}. \quad (36)$$

Here, N is the number of bins in the $\Delta\phi$ distribution. Consequently, one can determine v_n from $v_{n,n}$ from the following expression

$$v_n(p_T^a) = \frac{v_{n,n}(p_T^a, p_T^b)}{\sqrt{v_{n,n}(p_T^b, p_T^b)}} \quad (37)$$

Due to the collective behavior of the system formed in heavy-ion collisions, in the left panel for Pb-Pb, we observe a clear mass ordering of particles below $p_T < 2$ GeV/c. This provides significant evidence of radial flow in heavy-ion collisions. Interestingly, in small sys-

tems such as pp and p-Pb, for high-multiplicity events, similar observations are made, which signifies the presence of radial flow in small systems. Further, for $p_T > 2$ GeV/c, the v_2 of different particles cross each other and for $p_T > 2.5$ GeV/c, a clear baryon-meson grouping is observed in all the collision systems shown in Fig. 65. This baryon-meson grouping in heavy-ion collisions provides evidence of particle production through the quark-coalescence mechanism [148]. However, elliptic flow measurements in small systems at other multiplicity classes do not exhibit similar behavior (mass-ordering at low- p_T and baryon-meson separation at intermediate p_T) as observed in heavy-ion collisions [149]. The absence of such behaviour in elliptic flow measurements in these collisions at lower multiplicity regions could be influenced by the domination of jetty events in the measurements. Thus, an event shape-based study of anisotropic flow coefficients in small systems is timely to properly under-

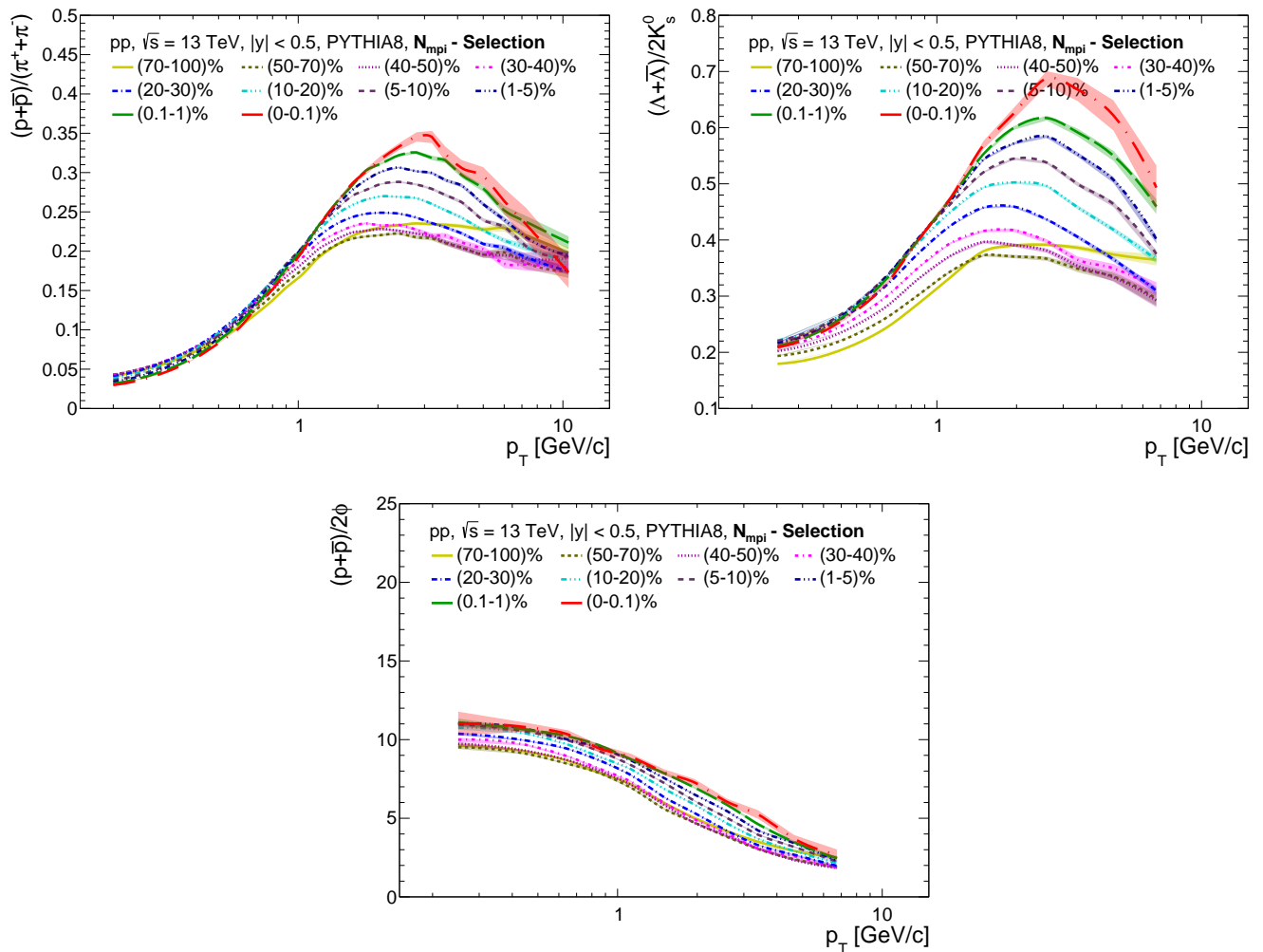


FIG. 54. p_T -differential p/π (upper left) and Λ/K_S^0 (upper right) and p/ϕ (lower middle) ratios measured in $|y| < 0.5$ for different N_{mpi} classes in pp collisions at $\sqrt{s} = 13$ TeV using PYTHIA8. The selection of events is based on N_{mpi} classes and shown in the right panel of Fig. 7.

stand the microscopic origin of flow signatures in small collision systems.

While understanding the collective dynamics in small collision systems with event-shape, a study is performed in e^+e^- collisions by measuring the two-particle azimuthal correlation of charged particles using the event-shape observable thrust [150]. The long-range near-side correlation is measured using archived hadronic e^+e^- data collected by ALEPH LEP-II at center-of-mass energies $\sqrt{s} = 183 - 209$ GeV. As discussed in Sec II, the event-shape observable thrust measures the out-of-event-plane energy flow. In this study, the thrust-axis is used to define the coordinate system. The determination of thrust axis and the exact procedure used to find the two-particle correlation functions can be found in Ref. [150]. The left and right panel of Fig. 66 show the associated azimuthal yield for $N_{\text{trk}} \geq 5$ (inclusive) and $N_{\text{trk}} \geq 50$ (high-multiplicity), respectively. For inclusive measure-

ment, the MC simulation based on the PYTHIA 6 model qualitatively describes the experimental data. However, high multiplicity class data exhibits a long-range near-side structure, while the MC simulation does not reproduce it well. In particular, the data have a significant slope compared to the PYTHIA 6 simulation at higher azimuthal angle $\Delta\phi$.

Furthermore, for the first time, the two-particle correlation function is decomposed in a Fourier series in e^+e^- collisions. The resulting anisotropic flow coefficients v_1 , v_2 , and v_3 are obtained as a function of p_T and shown in Fig. 67. The flow coefficients v_1 , v_2 , and v_3 measured from the data are compared with the PYTHIA 6 simulation results. It is observed that PYTHIA 6 has qualitative agreement with data for multiplicity integrated events, while for $N_{\text{trk}} \geq 50$ the PYTHIA 6 predicts a smaller magnitude for $|v_n|$. The interpretation of the positive v_2 and the negative v_3 in e^+e^- collisions can-

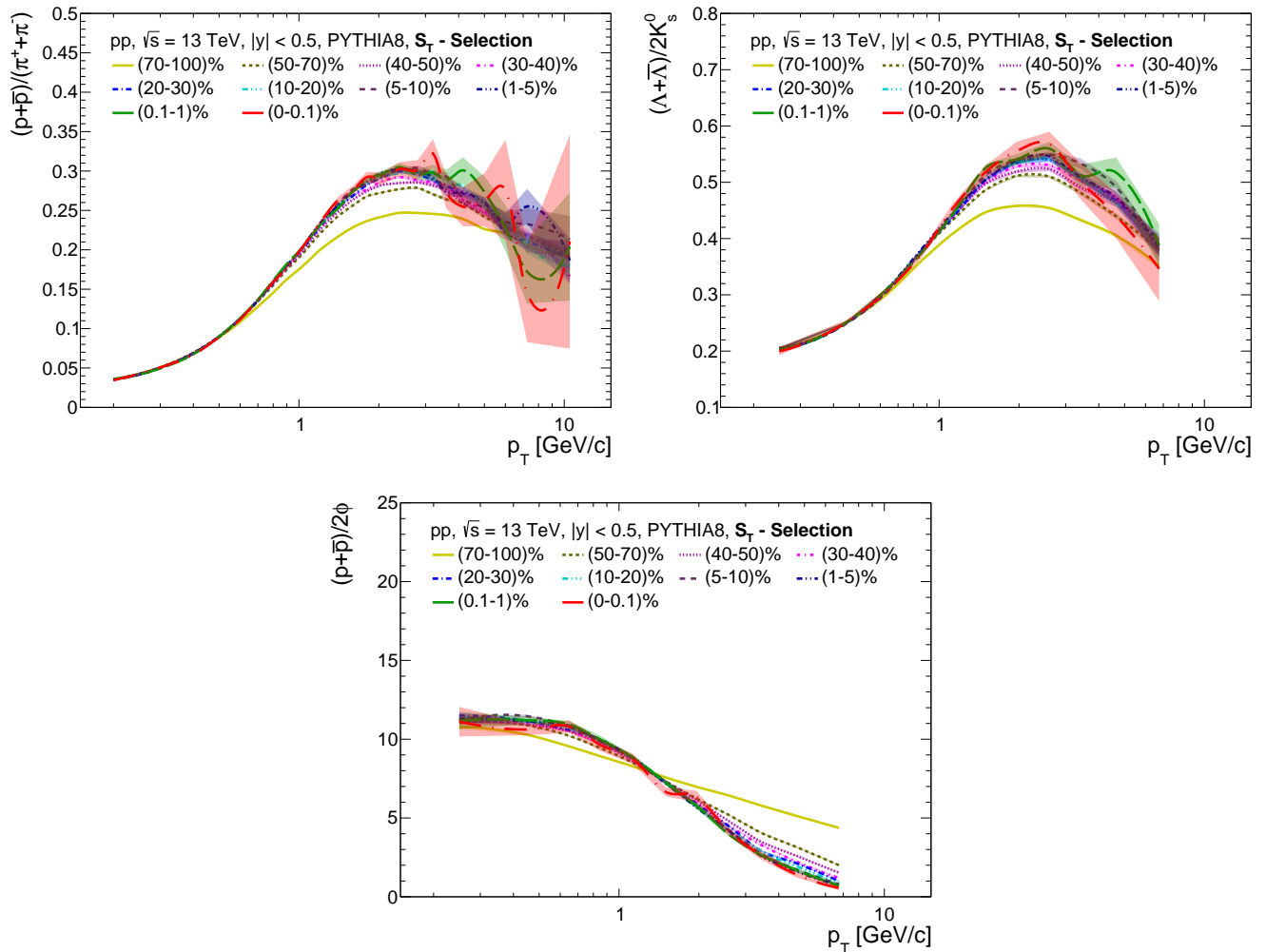


FIG. 55. p_T -differential p/π (upper left) and Λ/K_S^0 (upper right) and p/ϕ (lower middle) ratios measured in $|y| < 0.5$ for different unweighted transverse sphericity (S_T) classes in pp collisions at $\sqrt{s} = 13$ TeV using PYTHIA8. The selection of events is based on S_T classes and shown in the right panel of Fig. 9

not be explained by the geometry-driven interpretation. Hence, this motivates further theoretical and experimental efforts to identify the physics mechanisms that could be responsible for the emergence of collectivity in such systems. Future experiments such as the Electron-Ion Collider at BNL, the Future Circular Collider at CERN may provide new and more differential measurements to clarify the origin of long-range near-side correlations in small systems.

In a master thesis at Lund University [151], a detailed investigation of two-particle correlations using event-shape classifiers for proton-proton collisions was performed. In these preliminary studies, while comparing sphericity, R_T , and flattenicity, it is concluded that flattenicity selects flatter events than sphericity, both when looking at the low and high flattenicity bins. Also, it was found that flattenicity appears to be able to select the most isotropic events out of the three investigated clas-

sifiers, which makes it the best tool to probe QGP-like properties in small collision systems.

F. Searches for jet-quenching

Let us now move to one of the missing signals of QGP behavior in small systems, *i.e.*, jet quenching or jet-like region modification. So far, jet quenching effects have not been observed in small collision systems [21, 152–154].

The possible modification of the charged particles produced in the hard scattering in pp , p -Pb, and Pb-Pb collisions, the p_T distributions in the toward and away regions can be obtained after the subtraction of the p_T spectra in the transverse region. The subtracted yields ($dN_{ch}^{st,sa}/dp_T$) can be further normalised to those measured in minimum-bias (MB) pp collisions, which can be sensitive to jet quenching effects. The ratio can be given

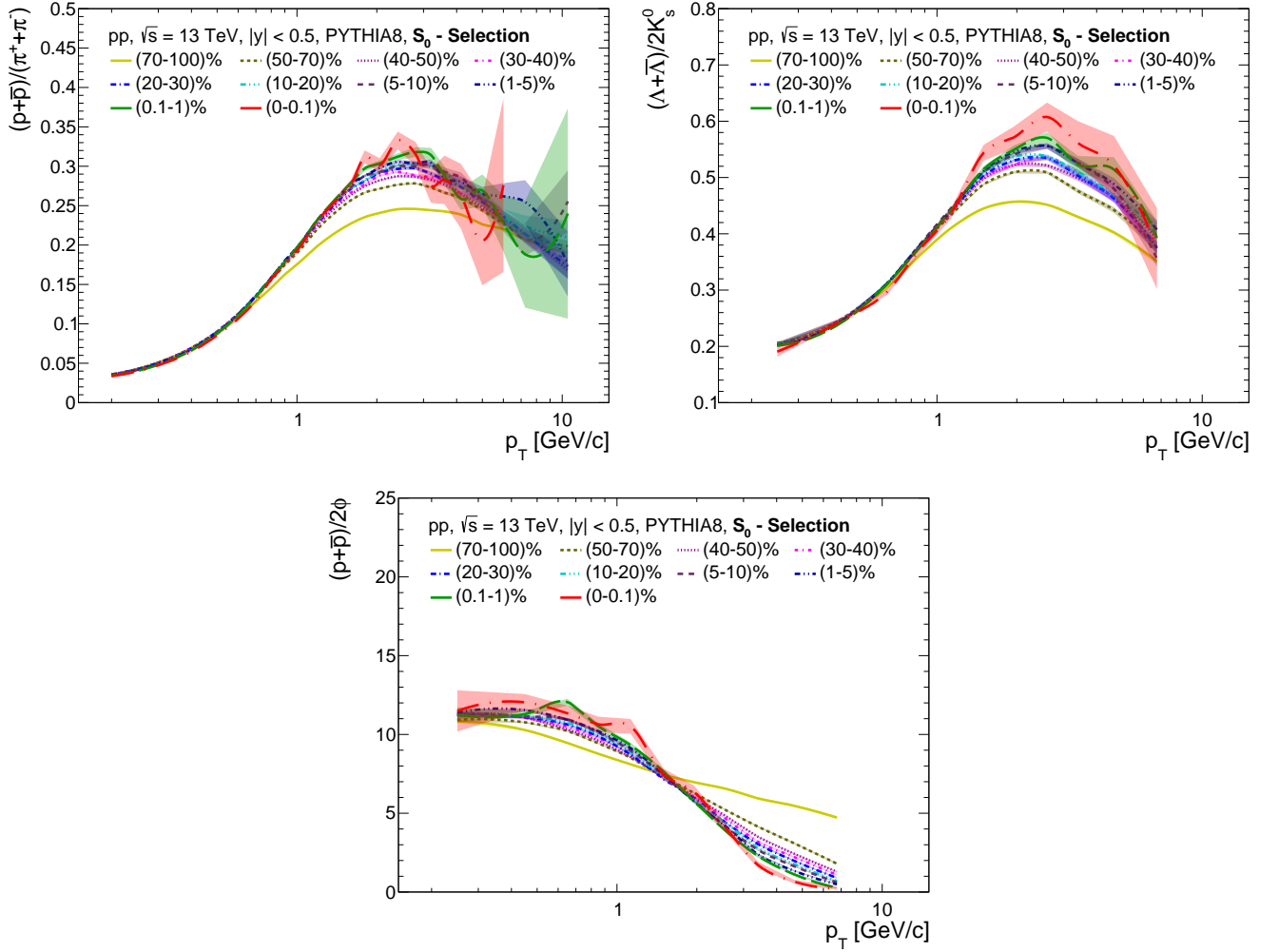


FIG. 56. p_T -differential p/π (upper left) and Λ/K_S^0 (upper right) and p/ϕ (lower middle) ratios measured in $|y| < 0.5$ for different weighted transverse sphericity (S_0) classes in pp collisions at $\sqrt{s} = 13$ TeV using PYTHIA8. The selection of events is based on S_0 classes and shown in the right panel of Fig. 12.

as,

$$I_X^{t,a} = \frac{(dN_{ch}^{st,sa}/dp_T)|_X}{(dN_{ch}^{st,sa}/dp_T)|_{pp,MB}}, \quad (38)$$

where X is the collision system and the event multiplicity class. In Eq. (38), the superscripts ‘t’ and ‘a’ stand for the p_T -differential yields in the toward and away regions, respectively. Further, the superscripts ‘sa’ and ‘st’ denote the p_T -differential yields in the toward and away regions, respectively, obtained after the subtraction of p_T spectra in the transverse region. With this ratio, the hard process p_T spectra in the toward and away regions are isolated, and thus allowing one to study possible jet-like region modifications to the produced particles due to medium effects in pp , p-Pb, and Pb-Pb collisions. In heavy-ion collisions, this ratio is similar to the studies using the quantity I_{AA} [155–157], where jets produced

in the early stages of the collision propagate through the hot and dense QGP. Their interaction with the medium leads to parton-energy loss, which is often referred to as jet quenching [158]. This effect manifests in the suppression of the high- p_T charged-particle yield in the away region [155, 156]. ALICE experiment attempted of I_X^t and I_X^a using an event classifier, *i.e.*, average charged-particle multiplicity in transverse region in $4 < p_T < 6$ GeV/c for different multiplicity classes in pp , p-Pb and Pb-Pb collisions at $\sqrt{s_{NN}} = 5.02$ TeV [26], as shown in Fig. 68. One observes that the Pb-Pb collisions clearly show jet-like region modifications while for both pp and p-Pb collisions the I_X^t and I_X^a values are found to be unity, indicating no jet-like region modification in the current precision.

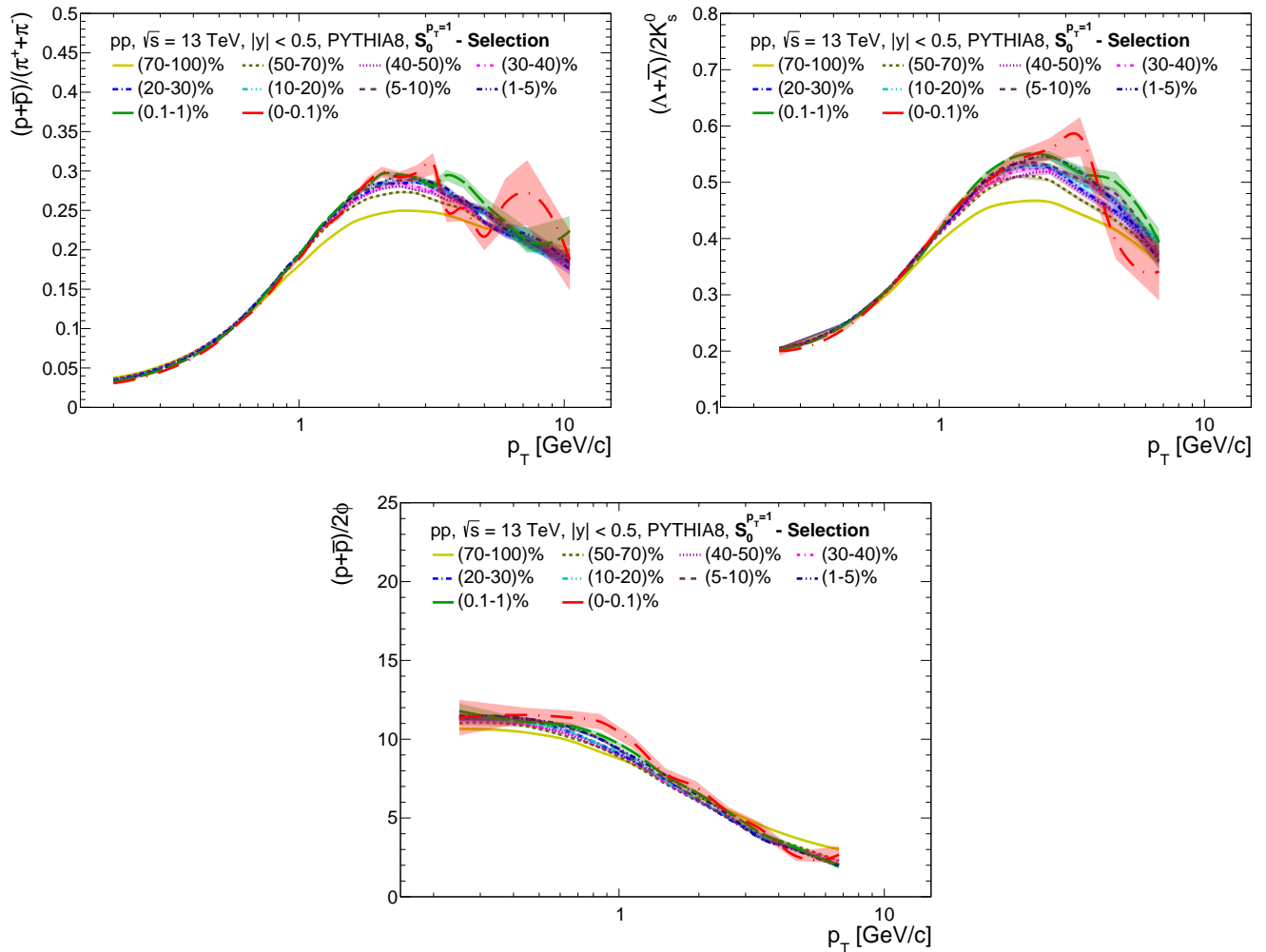


FIG. 57. p_T -differential p/π (upper left) and Λ/K_S^0 (upper right) and p/ϕ (lower middle) ratios measured in $|y| < 0.5$ for different unweighted transverse sphericity ($S_0^{p_T=1}$) classes in pp collisions at $\sqrt{s} = 13$ TeV using PYTHIA8. The selection of events is based on $S_0^{p_T=1}$ classes and shown in the right panel of Fig. 12

V. EXTENSION TO HEAVY-ION COLLISIONS

While discussing the studies related to small systems, it is now equally important to understand the dynamics of event shape observables in heavy-ion collisions, where the formation of QGP is most likely to occur. To bring all collision systems on an equal footing, we will now move our discussion towards extending the event classifiers to heavy-ion collisions. So far, there is no experimental study in such directions, except using flow vector [108]. As a starting point, we discuss the implementation of transverse sphericity in heavy-ion collisions.

A. Transverse Sphericity

Figure 69 top (bottom) panel shows S_0 distribution for different centrality (multiplicity) classes in Pb-Pb (pp) collisions at $\sqrt{s_{NN}} = 5.02$ TeV ($\sqrt{s} = 13$ TeV) obtained using AMPT (PYTHIA8). It is to be noted that the multiplicity in pp collisions is estimated in the V0 acceptance of the ALICE detector during Run 1 and Run 2, and the centrality selection in AMPT for Pb-Pb collisions is performed using geometrical impact parameter slicing. In pp collisions, S_0 distribution shifts towards the isotropic limit with increasing multiplicity selection; however, the peak of the distributions still lies towards the jetty event, except for the class having the highest multiplicity. This is due to the fact that a higher value of N_{ch}^{fwd} corresponds to events having higher N_{mpi} . A similar centrality dependence is observed in Pb-Pb collisions, where the distribu-

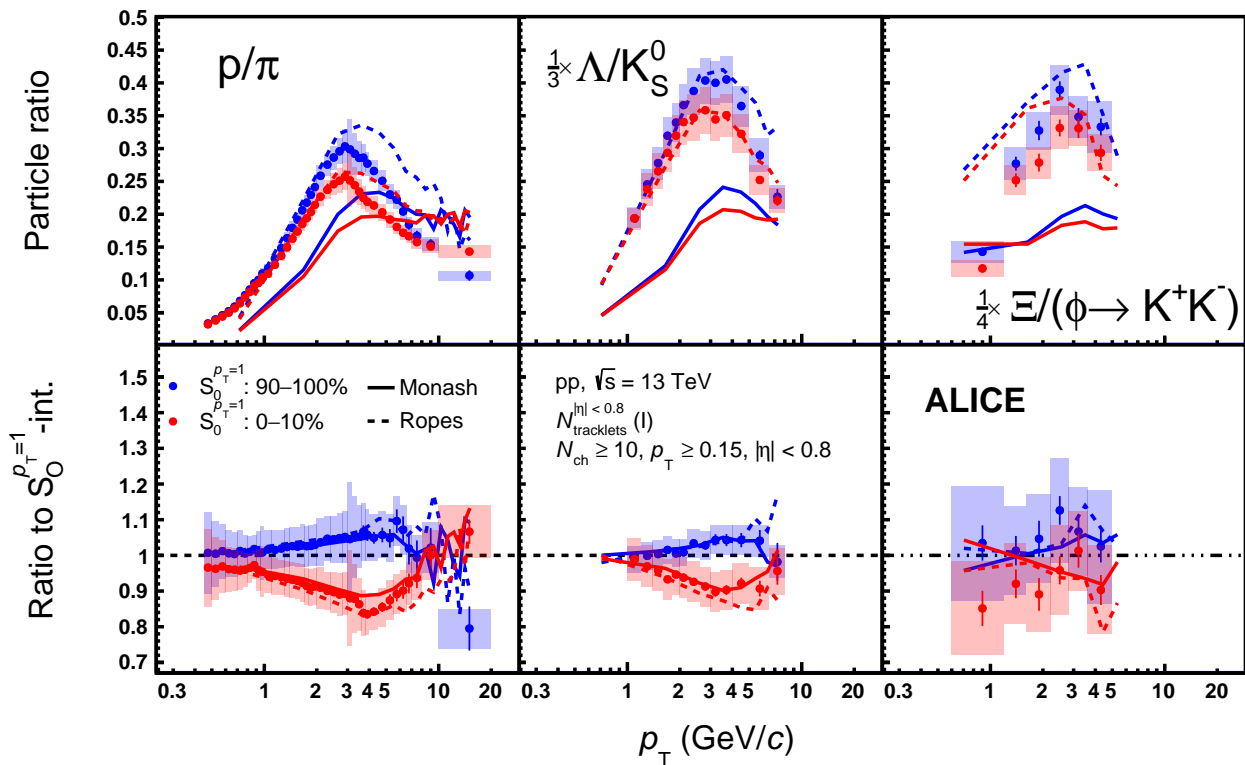


FIG. 58. p_T -differential p/π (upper left), Λ/K_S^0 (upper middle), and Ξ/ϕ (upper right) ratios for different classes of $S_0^{pT=1}$ for the top 0-1% multiplicity class measured by $N_{\text{tracklets}}^{|\eta|<0.8}$ in pp collisions at $\sqrt{s} = 13$ TeV with ALICE and compared with PYTHIA 8 Color Ropes and Monash. The lower panel shows the ratio to $S_0^{pT=1}$ -integrated case [53].

tion of transverse sphericity shifts towards the isotropic limits as one moves towards the central collisions. The peaks of the transverse sphericity distribution in Pb-Pb collisions always lie towards the extreme isotropic limit, where the formation of a QCD medium is viable. While both AMPT and PYTHIA8 have differences in the underlying processes, using transverse sphericity, one can probe for similar event topology, whether soft or hard interactions dominate underlying physical processes.

Figure 70 shows the transverse momentum space correlation (p_x vs p_y) for different classes of S_0 in (40-50)% Pb-Pb collisions at $\sqrt{s_{NN}} = 5.02$ TeV using AMPT. In the upper right figure, the S_0 -integrated events, a clear momentum-space anisotropy can be seen, which indicates the presence of initial-stage spatial anisotropy. The finite initial state spatial anisotropy can be understood as the presence of an almond-shaped overlap region in the mid-central collisions, where the presence of a larger pressure gradient along the x -axis than the y -axis. This consequently leads to the emission of particles with larger p_x , i.e., $p_x > p_y$. As one moves towards the high- S_0 events, the correlation almost vanishes, showing a circular geometry. This indicates an absence of momentum-space anisotropy in the final state and almost zero elliptic flow for the high- S_0 events. However, for the low- S_0 events,

a higher momentum space anisotropy is observed, where the transverse momentum correlation becomes more elliptical compared to the S_0 -integrated events. This feature of the transverse sphericity testifies to its applicability from small systems to heavy-ion collisions and as a probe to understand the formation of a QCD medium.

1. Two-particle correlations and anisotropic flow

One of the key signatures for collectivity is the anisotropic flow, which can be obtained using two-particle azimuthal correlations. As already highlighted in Fig. 70, the initial state spatial anisotropy can be probed using event shape observables, which translates to final state momentum anisotropy. So, the study of anisotropic flow with event shape would give an experimental handle to probe the collectivity. Figure 71 shows the two-particle azimuthal correlation function ($C(\Delta\phi)$) as a function of relative azimuthal angle for different transverse sphericity classes in (40-50)% centrality Pb-Pb collisions using AMPT. In Fig. 71, the peak and width of the correlation function vary strongly with respect to the choice of transverse sphericity selection. This indicates that using transverse sphericity, one can distinguish events based

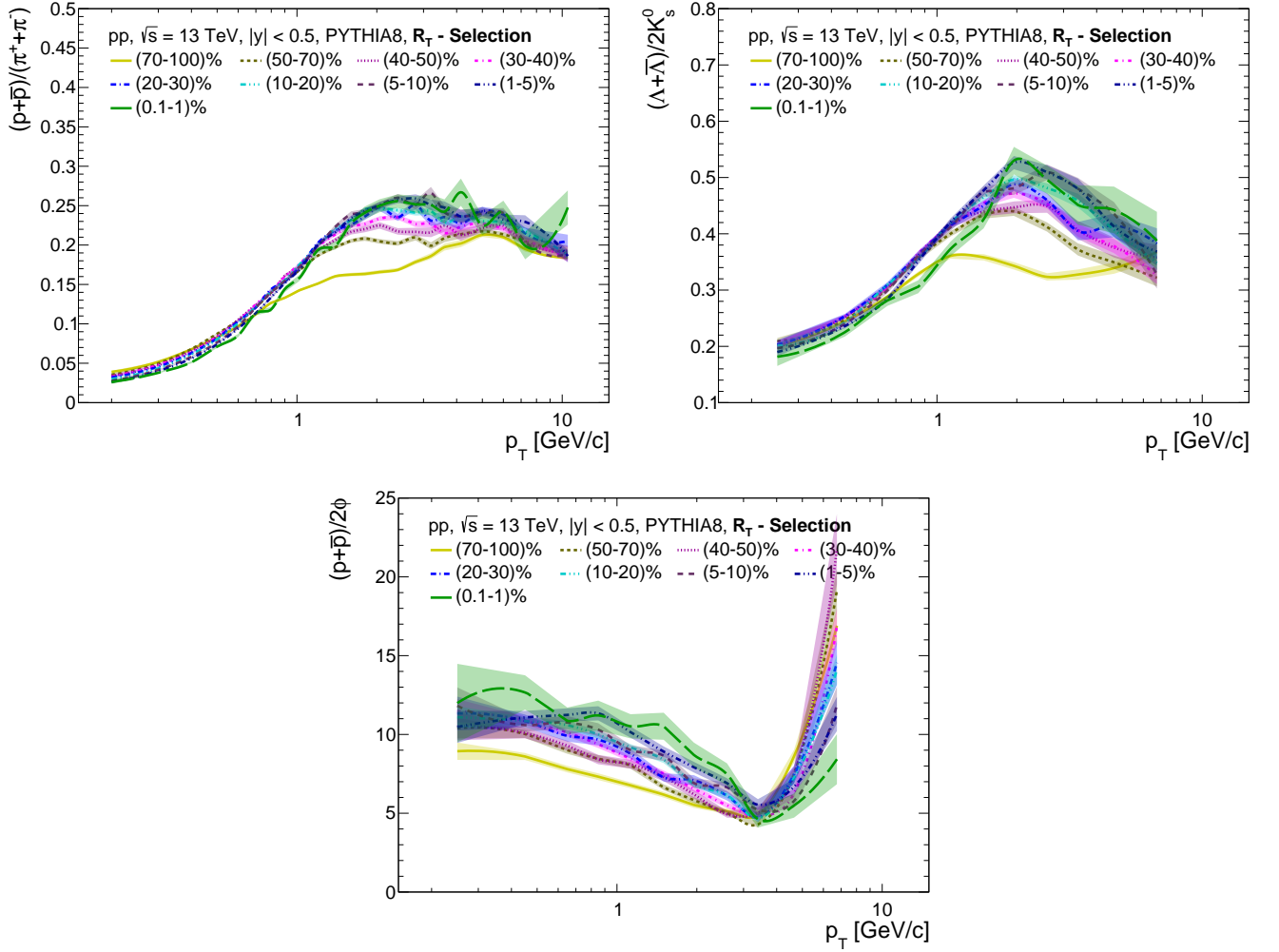


FIG. 59. p_T -differential p/π (upper left) and Λ/K_S^0 (upper right) and p/ϕ (lower middle) ratios measured in $|y| < 0.5$ for different relative transverse activity classifier (R_T) classes in pp collisions at $\sqrt{s} = 13$ TeV using PYTHIA8. The selection of events is based on R_T classes and shown in the left panel of Fig. 17

on geometrical shapes. In addition, one can observe that for low- S_0 events, the two-particle azimuthal correlation function has a larger peak compared to S_0 -integrated and high- S_0 events have the smallest peak structure. This indicates the presence of a larger elliptic flow for low- S_0 events. Furthermore, one observes two peaks in the away side region for high- S_0 events, indicating the presence of a larger triangular flow in such events.

Figure 72 shows the elliptic flow (v_2) (top) and triangular flow (v_3) (bottom) as a function of transverse momentum for different classes of transverse sphericity in Pb-Pb collisions at $\sqrt{s_{NN}} = 5.02$ TeV using AMPT. The results in Fig. 72 are limited to (40-50)% centrality class only as the mid-central events are expected to have the highest contribution from both elliptic flow and triangular flow, which could help us to identify the transverse sphericity dependence clearly. As inferred from Fig. 71, where the signals for the two-particle correlation

function are highest for the low- S_0 events, indicating a larger value of elliptic flow. A similar direct conclusion can be found in Fig. 72. One finds that, as events go from high- S_0 events to low- S_0 events, the value of elliptic flow increases. This shows that elliptic flow has a direct anti-correlation with transverse sphericity selection. However, in the bottom panel of Fig. 72, the triangular flow is found to have the highest value for the high- S_0 class of events and possesses a minimum value for the low- S_0 events, as inferred from Fig. 71. Triangular flow is found to have a positive correlation with the transverse sphericity selection.

Figure 73 shows the elliptic flow (v_2) (top) and triangular flow (v_3) (bottom) as a function of centrality for different classes of transverse sphericity in Pb-Pb collisions at $\sqrt{s_{NN}} = 5.02$ TeV using AMPT. In heavy-ion collisions, the pressure gradient formed during the collision is responsible for transforming the initial spatial anisotropy

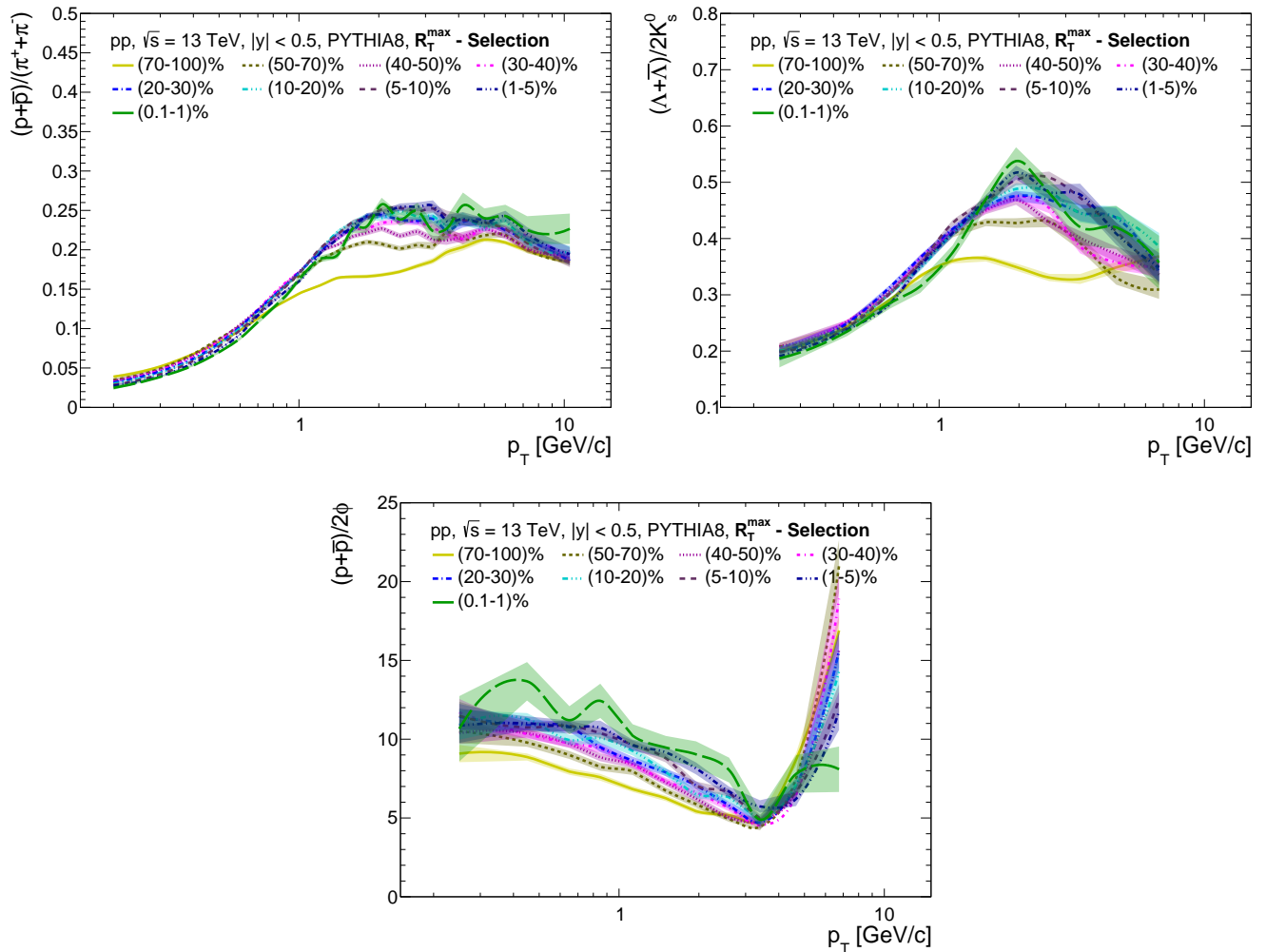


FIG. 60. p_T -differential p/π (upper left) and Λ/K_S^0 (upper right) and p/ϕ (lower middle) ratios measured in $|y| < 0.5$ for different maximum relative transverse activity classifier (R_T^{\max}) classes in pp collisions at $\sqrt{s} = 13$ TeV using PYTHIA8. The selection of events is based on R_T^{\max} classes and shown in the middle panel of Fig. 17

to the final momentum space anisotropy. In most central collisions, the collision geometry is almost spherical, which is reflected in the low value of anisotropic flow coefficients. As one moves towards the mid-central collisions, the value of both elliptic and triangular flow starts to rise because the collision overlap region retains an almond-shaped structure, as seen in the figure. However, for the peripheral collisions, due to the low system size, the lifetime of the QCD medium is very short, which leads to a lower value of anisotropic flow. The important thing to notice in the figure is that transverse sphericity plays a crucial role in the event selections for the anisotropic flow coefficients. This is because the anisotropic flow coefficients are found to be very sensitive to transverse sphericity selection.

2. Eccentricity and elliptic flow fluctuations

The strong correlation of S_0 with v_2 shown in the previous section can be exploited to constrain the probability distributions of v_2 , thereby reducing their event-by-event fluctuations. The left panel of Fig. 74 shows the relative eccentricity fluctuations, $F(\epsilon_2) = \sigma_{\epsilon_2}/\langle\epsilon_2\rangle$, as a function of centrality for different classes of transverse sphericity in Pb-Pb collisions at $\sqrt{s_{NN}} = 5.02$ TeV using AMPT. Here, $\sigma_{\epsilon_2} = \sqrt{\langle\epsilon_2^2\rangle - \langle\epsilon_2\rangle^2}$ is the eccentricity fluctuation, $\langle\epsilon_2\rangle$ is the event-average eccentricity and $\langle\epsilon_2^2\rangle$ is the RMS value. Towards the most central collisions, the collision overlap region is close to a circle in the transverse plane, where the eccentricity of the collision geometry is small. In this region, the measured finite values of initial eccentricity are dominated by event-by-event eccentricity fluctuations, driven by the density fluctuations. Thus, the relative eccentricity fluctuations are the highest in

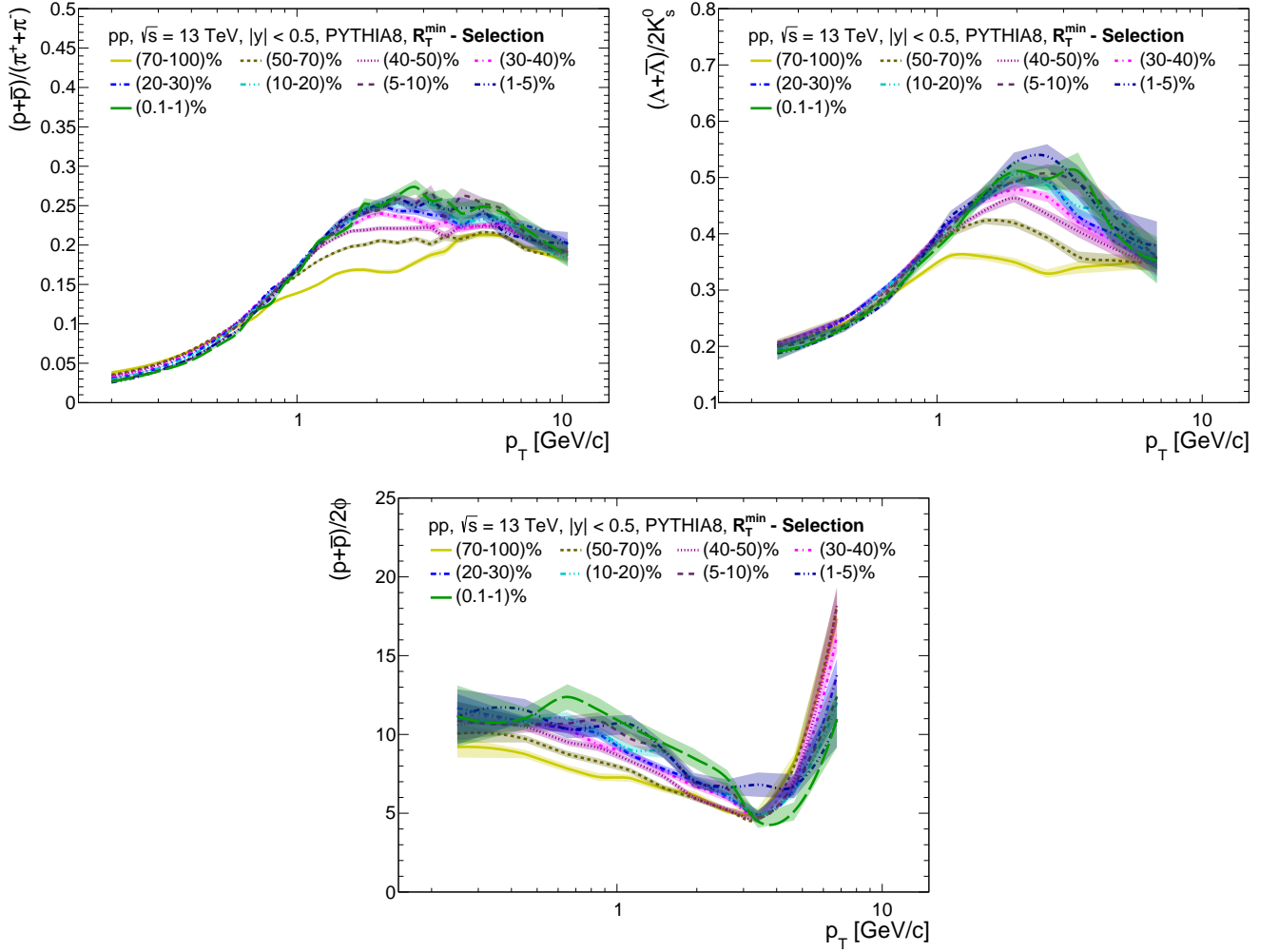


FIG. 61. p_T -differential p/π (upper left) and Λ/K_S^0 (upper right) and p/ϕ (lower middle) ratios measured in $|y| < 0.5$ for different minimum relative transverse activity classifier (R_T^{\min}) classes in pp collisions at $\sqrt{s} = 13$ TeV using PYTHIA8. The selection of events is based on R_T^{\min} classes and shown in the right panel of Fig. 17

the central collisions. However, as one moves towards the mid-central collisions, the collision geometry becomes elliptic, and the corresponding contribution of eccentricity fluctuation reduces in the measured value of eccentricity. It is interesting to see that for the S_0 integrated case $F(\epsilon_2)$ is highest compared to other sphericity classes in (0-20)% centrality. Towards the mid-central and peripheral collisions, high- S_0 events are found to have the largest values of $F(\epsilon_2)$, where the collision overlap geometry is expected to be isotropic. $F(\epsilon_2)$ is found to be smallest for the low- S_0 classes where the collision geometry is elliptic [70] compared to other S_0 classes.

Relative elliptic flow fluctuations, $F(v_2) = \sigma_{v_2}/\langle v_2 \rangle$, is shown in the right panel of Fig. 74. Here, $\sigma_{v_2} = \frac{\sqrt{v_2^2\{2,|\Delta\eta|>1.0\} - v_2^2\{4\}}}{2}$ is the elliptic flow fluctuations and $\langle v_2 \rangle = \frac{\sqrt{v_2^2\{2,|\Delta\eta|>1.0\} + v_2^2\{4\}}}{2}$ is the RMS value of elliptic flow estimated from two- and four- particle Q-cumulant

method [71]. For a particular sphericity class, $F(v_2)$ is higher for the central and peripheral collisions and shows a minimum in the mid-central collisions. This is expected as the collision geometry is isotropic, having a smaller value of v_2 , in the central collisions where the contribution is dominated by event-by-event fluctuations rather than elliptic geometry. On the other hand, in the peripheral collisions, although the collision overlap region is driven by an initial large elliptic geometry, a smaller size of the system results in large fluctuations of elliptic flow. Similar to $F(\epsilon_2)$, low- S_0 events possess smaller $F(v_2)$ and within uncertainties, one can observe a larger $F(v_2)$ in the (0-20)% centrality class for the S_0 -integrated case as compared to other classes of transverse sphericity.

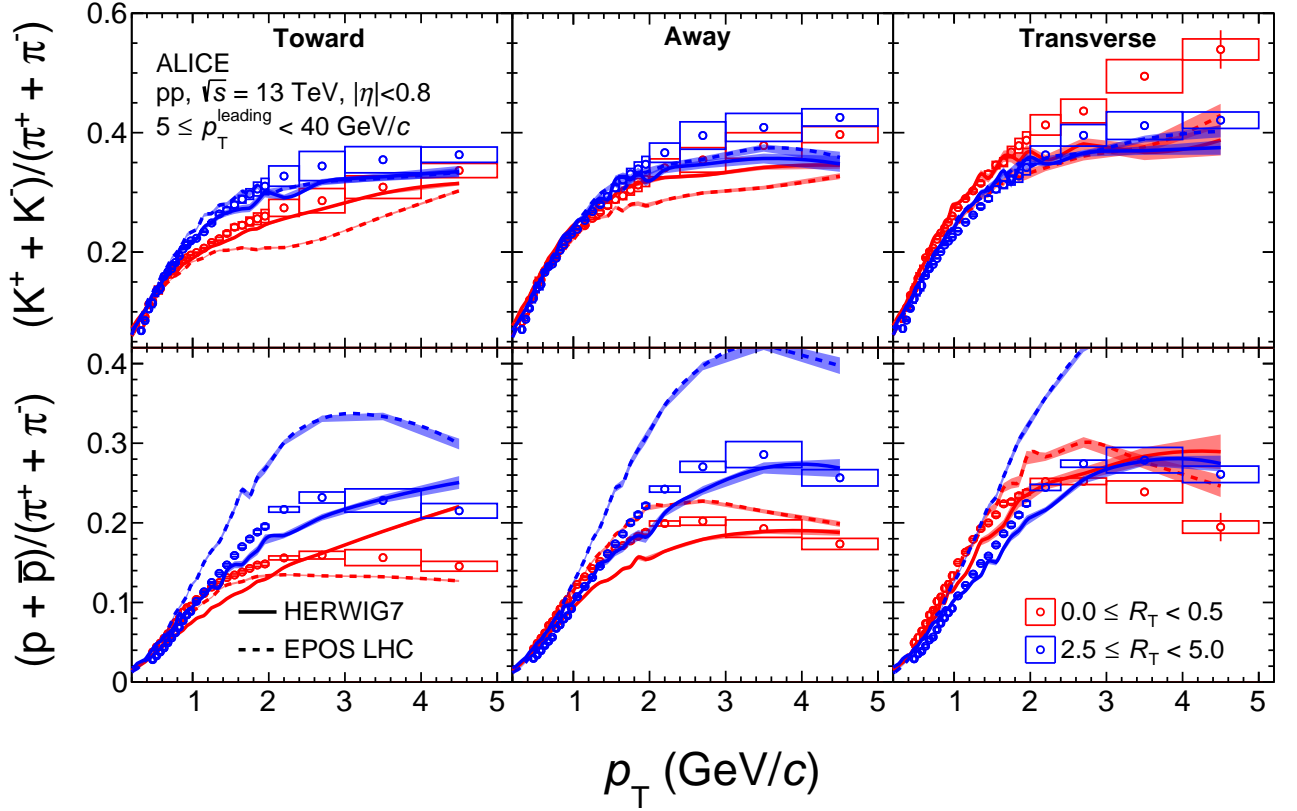


FIG. 62. p_T -differential K/π (upper) and p/π (lower) ratios measured in different topological regions as a function of R_T in pp collisions at $\sqrt{s} = 13$ TeV with ALICE. Comparisons are made with similar measurements performed with EPOS LHC and HERWIG7 [50].

3. Symmetry Plane Correlations

After the discussion on anisotropic flow coefficients, their fluctuations, and the impact of event shape selection on these coefficients, it is equally important to understand the significance of symmetry plane angles, ψ_n . However, unlike v_n , the estimation of ψ_n is not trivial in experiments due to uncertainty in the estimation of the reaction plane. Therefore, it is pointless to estimate ψ_n in heavy-ion collisions, which would always be ‘0’, due to their random orientation for each event.

However, the studies of symmetry plane correlation bear a great amount of significance. Similar to anisotropic flow coefficients, which depend upon the initial spatial anisotropy and are sensitive to the transport properties of the medium, the symmetry plane correlations (SPCs) can provide an independent measure of the initial correlations among the participant planes and are sensitive to the transport properties of the medium formed. Thus, the studies of SPCs can provide an independent measure of the transport properties of the systems. The calculation of anisotropic flow coefficients (v_n) along with the symmetry plane angles (ψ_n) can be performed using the following expression [147, 159, 160].

$$v_{n_1}^{a_1} v_{n_2}^{a_2} \dots v_{n_k}^{a_k} e^{i(a_1 n_1 \psi_{n_1} + a_2 n_2 \psi_{n_2} + \dots + a_k n_k \psi_{n_k})} = \langle e^{i(n_1 \phi_1 + n_2 \phi_2 + \dots + n_l \phi_l)} \rangle \quad (39)$$

Here, a_i denotes the number of times the harmonics n_i

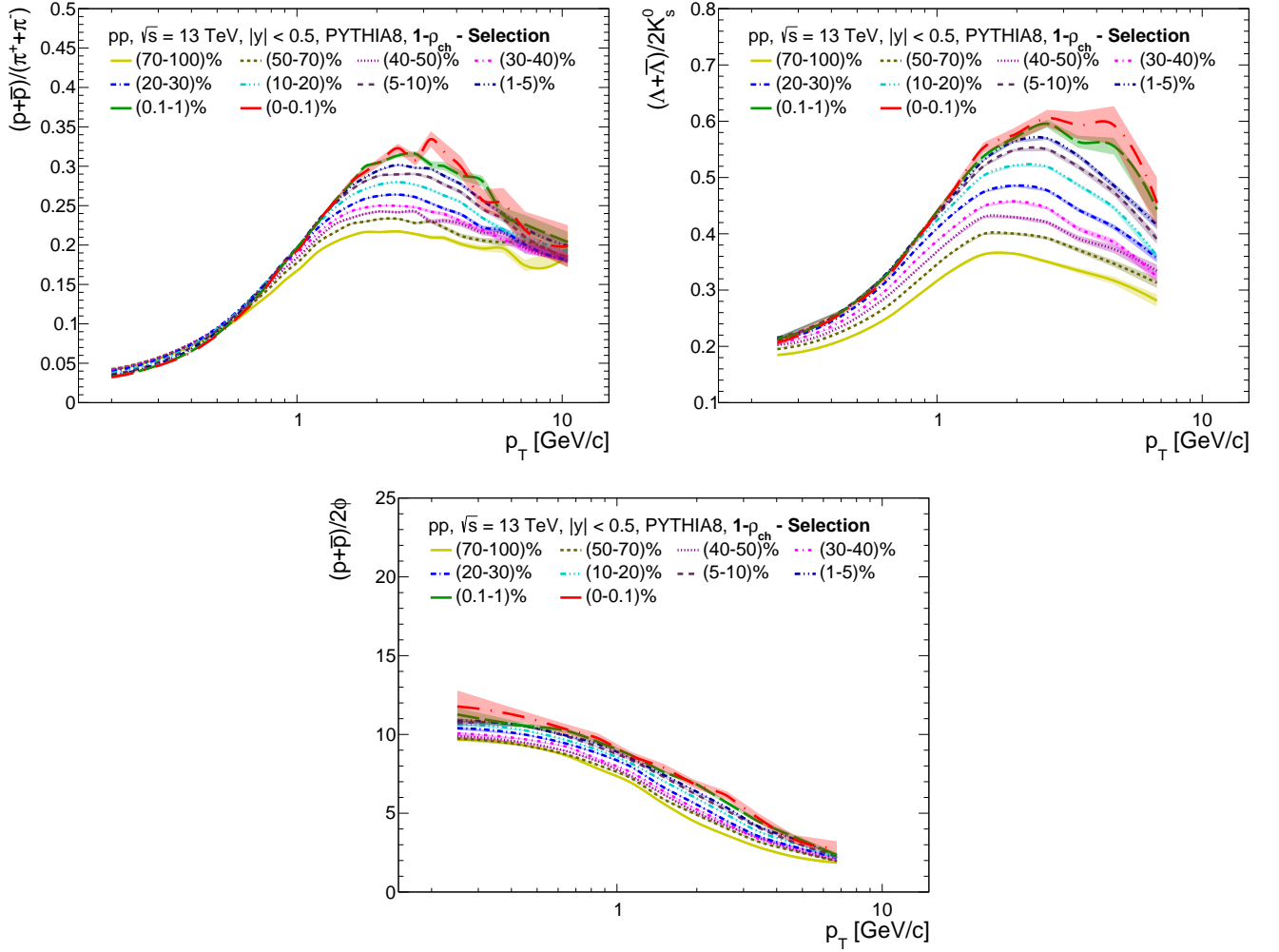


FIG. 63. p_T -differential p/π (upper left) and Λ/K_S^0 (upper right) and p/ϕ (lower middle) ratios measured in $|y| < 0.5$ for different charged-particle flattenicity ($1 - \rho_{ch}$) classes in pp collisions at $\sqrt{s} = 13$ TeV using PYTHIA8. The selection of events is based on $(1 - \rho_{ch})$ classes and is shown in Fig. 19

or equivalently $-n_i$ occurs². The choice of n_i and a_i are made such that $\sum_{i=1}^k a_i n_i = 0$.

The estimation of SPCs is performed using the Gaussian Estimator method [147, 159, 160], defined as follows.

$$\begin{aligned} & \langle \cos(a_1 n_1 \psi_1 + a_2 n_2 \psi_2 + \dots + a_k n_k \psi_k) \rangle_{GE} \\ &= \sqrt{\frac{\pi}{4}} \frac{\langle v_{n_1}^{a_1} v_{n_2}^{a_2} \dots v_{n_k}^{a_k} \cos(a_1 n_1 \psi_1 + a_2 n_2 \psi_2 + \dots + a_k n_k \psi_k) \rangle}{\sqrt{\langle v_{n_1}^{2a_1} v_{n_2}^{2a_2} \dots v_{n_k}^{2a_k} \rangle}} \end{aligned} \quad (40)$$

² Due to a azimuthal symmetry of particle distribution of particles, i.e., invariance of Eq. (34) for $\phi \rightarrow -\phi$, allows $v_n = v_{-n}$ and $\psi_n = \psi_{-n}$. This is useful to construct the symmetry plane correlations among specific harmonics.

Here, $\langle \dots \rangle$ denotes the event average over a particular set of events. Figure 75 shows the centrality and sphericity dependence of SPCs in Pb-Pb collisions at $\sqrt{s_{NN}} = 5.02$ TeV using AMPT. Figures 75 (a), (b) and (c) show $\langle \cos[4(\psi_4 - \psi_2)] \rangle_{GE}$, $\langle \cos[6(\psi_6 - \psi_2)] \rangle_{GE}$, and $\langle \cos[6(\psi_3 - \psi_2)] \rangle_{GE}$, respectively. The strength of the correlations for the sphericity-integrated events decrease from $\langle \cos[4(\psi_4 - \psi_2)] \rangle_{GE}$ to $\langle \cos[6(\psi_6 - \psi_2)] \rangle_{GE}$, and $\langle \cos[6(\psi_3 - \psi_2)] \rangle_{GE}$, which require 3, 4 and 5 particle correlations, respectively, for their estimation. These initial state correlations and their event-by-event fluctuations can be traced back to the correlation among the participant planes and their event-by-event fluctuations. The initial state fluctuations are random in nature and arise due to the finite size of the participants in the collision. According to the central limit theorem, the average of random fluctuations converges to a Gaussian distribution when the number of sampling is large. For a distribu-

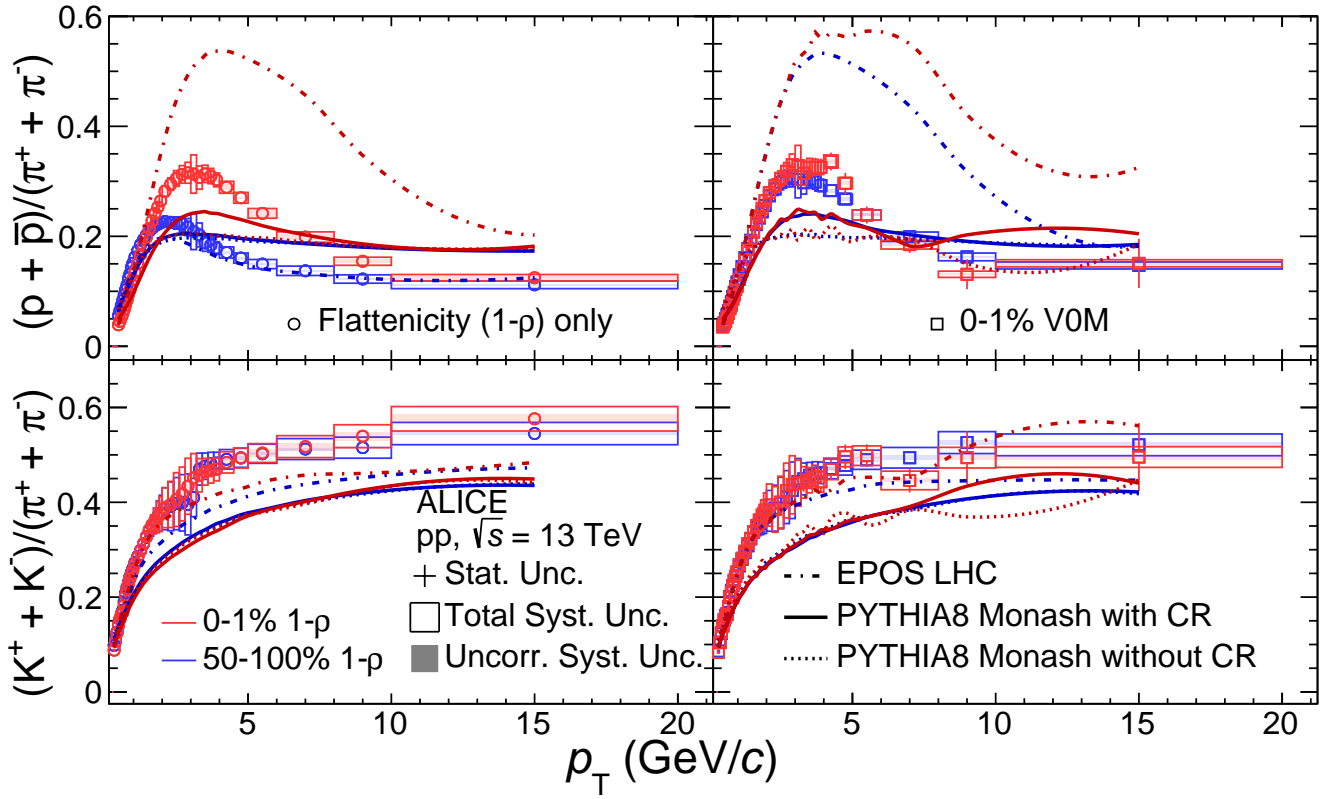


FIG. 64. p_T -differential proton to pion (upper) and kaon to pion (lower) ratios for different classes of flattenicity in minimum bias (left) and (0-1)% V0M class (right) in pp collisions at $\sqrt{s} = 13$ TeV with ALICE [55].

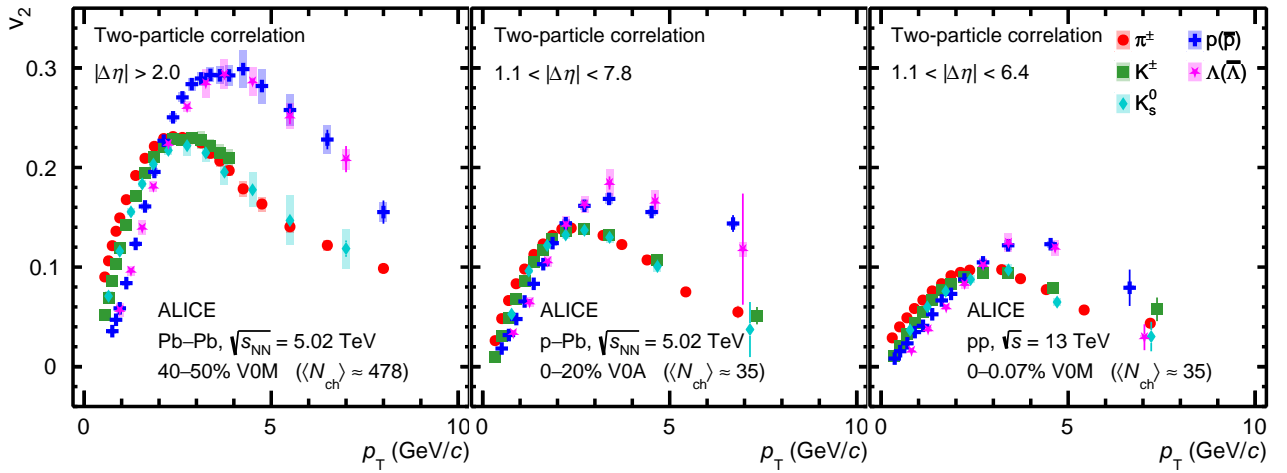


FIG. 65. Elliptic flow (v_2) of mesons (π^\pm , K^\pm , K_S^0) and baryons ($p + \bar{p}$, $\Lambda + \bar{\Lambda}$) with $|\eta| < 0.8$ in Pb-Pb collisions at $\sqrt{s_{NN}} = 5.02$ TeV (left), p-Pb collisions at $\sqrt{s_{NN}} = 5.02$ TeV (upper right) and pp collisions at $\sqrt{s} = 13$ TeV (right) using two-particle correlation method. Centrality and multiplicity classes are chosen based on the multiplicity deposited in the V0 detector of ALICE [147].

tion close to Gaussian, the second-order cumulant has the largest values, the values of other moments are smaller,

and vanish for higher-order moments. Here, the number of particle correlations is related to the order of particle

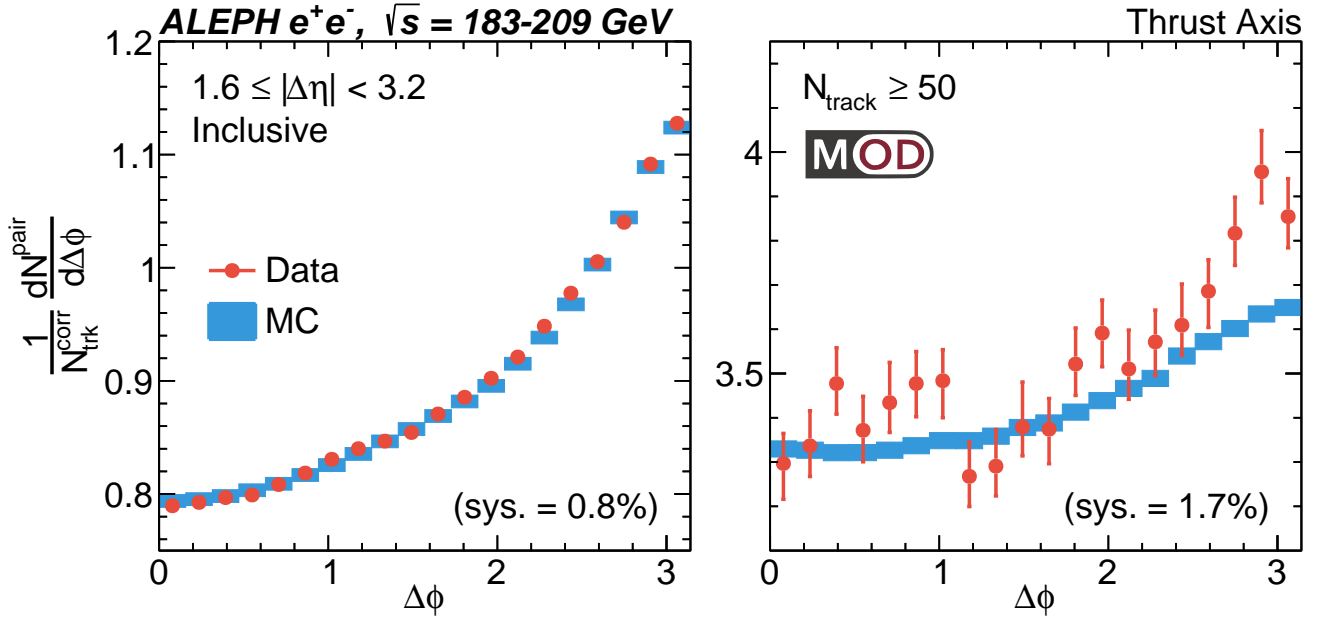


FIG. 66. The azimuthal associated yield for the long-range region $1.6 < |\Delta\eta| < 3.2$ is shown for $N_{\text{trk}} \geq 5$ (left) and $N_{\text{trk}} \geq 50$ (right). The red dots with statistical error bars are from experimental data, while the blue line with statistical error bars is obtained from the PYTHIA 6 model [150]

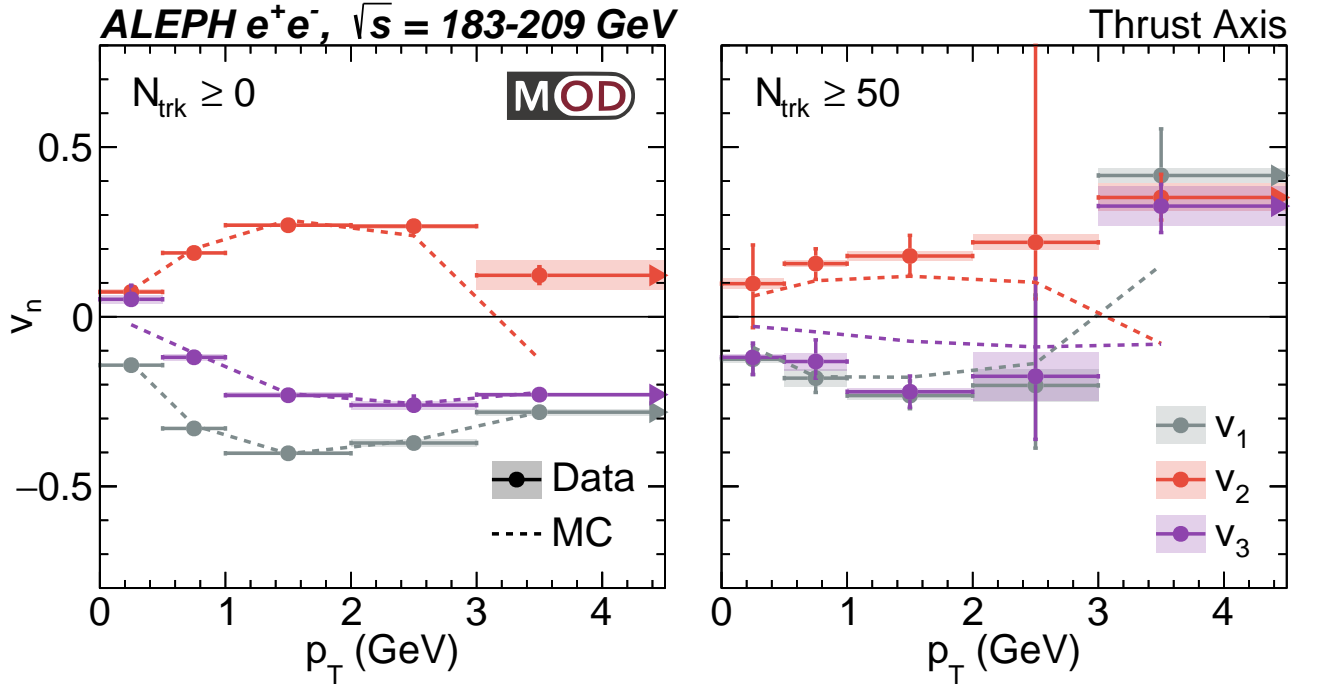


FIG. 67. v_n as a function of p_T for $N_{\text{trk}} \geq 0$ (left) and $N_{\text{trk}} \geq 50$ (right) for the thrust axis analysis using LEP-II data. The marker with black, red, and purple error bars represents v_1 , v_2 , and v_3 measured from the data. The dashed line with the corresponding color represents the results obtained from the MC simulation [150]

cumulants, which explains the quantitative behavior of different SPCs. Looking at the sphericity dependence, one finds that for a non-vanishing choice of SPCs, low-

S_0 events have larger correlations as compared to high- S_0 events, which are sometimes negative. This can be intuitively understood since the low- S_0 events have an

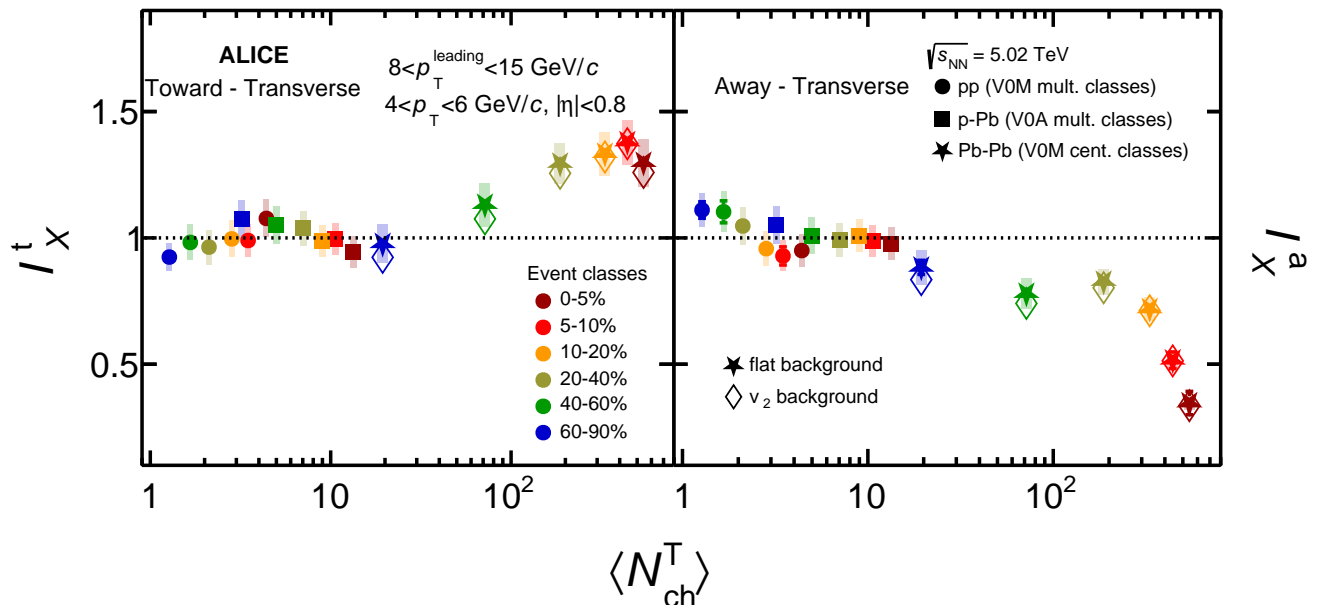


FIG. 68. I_X^t (left panel) and I_X^a (right panel) as a function of average charged-particle in transverse region in $4 < p_T < 6$ GeV/c for different multiplicity classes in pp , p -Pb and Pb-Pb collisions at $\sqrt{s_{NN}} = 5.02$ TeV [26].

elliptic geometry, the symmetry planes align themselves with ψ_2 , leading to a rise in SPCs. On the other hand, since high- S_0 events have isotropic emission of particles, the symmetry planes do not have any specific direction of alignment, which leads to smaller values. It is interesting to note that, although v_2 and v_3 are anticorrelated, in this study we do not observe any correlation between ψ_2 and ψ_3 , for all classes of S_0 [108, 162–167]. This highlights the applicability of SPCs to probe the transport properties of the system formed in heavy-ion collisions, where the application of event shape selections can enhance our understanding.

4. Kinetic freeze-out temperature and radial flow

One of the crucial observables used in the high-energy collisions is the study of kinetic freeze-out temperature (T_{kin}) versus mean transverse radial flow velocity ($\langle\beta_T\rangle$), which gives much more information about the system formed in such collisions. Both these observables are anti-correlated and are proportional to the system formed in heavy-ion collisions [143]. Figure 76 shows T_{kin} versus $\langle\beta_T\rangle$ for different classes of transverse sphericity and centrality extracted from a simultaneous fit of Boltzmann-Gibbs Blastwave function to identified particle transverse momentum spectra in Pb-Pb collisions at $\sqrt{s_{NN}} = 5.02$ TeV using AMPT. For a particular class of transverse sphericity, as one moves from central to peripheral collisions, T_{kin} increases and the value of $\langle\beta_T\rangle$ decreases. This is because, due to the large number of particles in

the most central collisions, the outward pressure is large, which contributes to a larger value of $\langle\beta_T\rangle$. On the other hand, due to the large multiplicity in the most central collisions, the system would take a longer time to reach kinetic freeze-out. However, as one moves towards the peripheral collisions, due to less multiplicity, one may find a lower value for $\langle\beta_T\rangle$ and a higher value for T_{kin} . As seen previously, transverse sphericity is proportional to the charged-particle multiplicity; thus, for the high- S_0 events, one may find a larger multiplicity than for low- S_0 events. Consequently, one may observe a higher value for $\langle\beta_T\rangle$ and a lower value for T_{kin} for high- S_0 events in contrast to low- S_0 events, as shown in Fig. 76.

In small systems such as pp collisions, the calculation of sphericity is much easier in experiments due to the smaller number of final-state charged particles; however, the calculation can become computationally challenging in heavy-ion collisions where the final-state charged-particle multiplicity is comparably larger than that obtained in pp collisions. This leads to the need for machine learning based regression models to estimate the value of transverse sphericity from the final-state charged particles in heavy-ion collisions on an event-by-event basis. Thus, we will also discuss the implementation of ML models in this section.

B. Reduced flow vectors (q_n)

As stated earlier, the reduced flow vectors are one of the observables often used in heavy-ion collisions to select

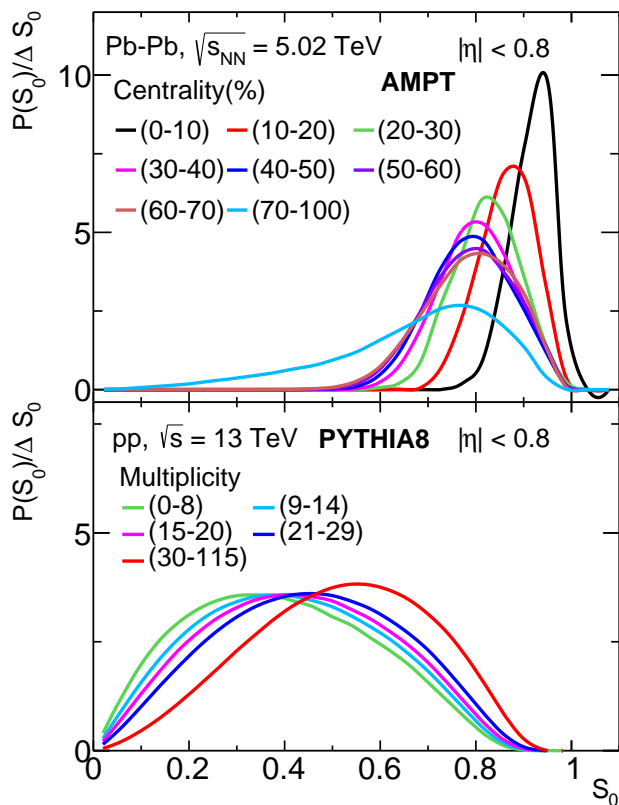


FIG. 69. Top panel: p_T -weighted transverse sphericity (S_0) distribution for different classes of collision centrality in Pb–Pb collisions at $\sqrt{s_{NN}} = 5.02$ TeV using AMPT. Bottom panel: p_T -weighted transverse sphericity (S_0) distribution for different multiplicity classes in V0 acceptance region of ALICE detector in pp collisions at $\sqrt{s} = 13$ TeV using PYTHIA8 [67].

events based upon different magnitudes of anisotropic flow coefficients. For example, q_2 , the second-order reduced flow vector, is often used to select events with smaller or larger values of elliptic flow. Similarly, the third-order reduced flow vector, q_3 , is useful to identify the triangular events. In this section, we review some of the usages of reduced flow vectors.

Figure 77 shows the two-particle correlation function as a function of relative azimuthal angle for different percentiles of events selected with q_2 (left) and q_3 (right) in Pb–Pb collisions at $\sqrt{s_{NN}} = 2.76$ TeV with ATLAS [108]. In the left panel, one selects the events having the largest (red open circles) and smallest (blue open squares) elliptic events with q_2 . One finds that the events with the largest values of q_2 show an amplified two-distinct peak structure as compared to when no q_2 based event selection was applied. Further, a three-peak structure in $C(\Delta\phi)$ is observed when the smallest q_2 events are selected, which corresponds to events dominated by triangular flow. Similarly, in the right panel, the two-particle correlation function as a function of relative azimuthal

angle is shown for different event percentiles of q_3 . Here, the behavior is opposite of what we observed in the left panel, where events are selected based on q_2 . Two-peak structure in the away-side region of the two-particle correlation function for the largest q_2 events hints at a large contribution of triangular flow, v_3 .

The observations made in Fig. 77 are reflected in the extracted flow coefficients. Fig. 78 shows p_T -differential v_2 , v_3 , v_4 and v_5 , from top to bottom, respectively, as a function of events selected with q_2 (left) and q_3 (right) in Pb–Pb collisions at $\sqrt{s_{NN}} = 2.76$ TeV with ATLAS [108]. As inferred from Fig. 77, in Fig. 78, we observed large v_2 and smaller v_3 for the largest q_2 events. Similarly, a higher v_3 and smaller v_2 are observed for events selected by q_3 . These observations hint at an anti-correlation between v_2 and v_3 . Further, the event selection with q_2 affects both v_4 and v_5 , which shows higher values for the event with large q_2 . This indicates a non-linear contribution of v_2 on v_4 and v_5 . In contrast, the event selection with q_3 has a small impact on v_4 , where large v_3 events possess small values of v_4 . This can be attributed to the positive correlation between v_2 and v_4 and the anti-correlation between v_2 and v_3 . Further, a positive correlation between q_3 and v_5 signifies a non-linear contribution of v_3 on v_5 measurements. Thus, the studies of reduced flow vectors in heavy-ion collisions are useful to quantify the contributions of v_2 and v_3 on higher order anisotropic flow coefficients, which can also be removed following the method discussed in Ref. [108]. A similar measurement is also performed with ALICE [110], where v_2 with event selection with q_2 from two different detectors. Here, q_2 is measured with the charged particles in both midrapidity using TPC and forward rapidity using the ALICE V0C detector. One finds that q_2 estimated with TPC selects events with stronger elliptic flow in the midrapidity region as compared to q_2 estimated with the ALICE V0C detector. The main contributor to this difference is attributed to the selectivity of q_2 from TPC, which is different from that of V0C. This is explicitly checked in Ref. [110] by relaxing the selection itself or rejecting a random fraction of tracks for the computation of q_2 from TPC. It is observed that the selection of (65–100)% for the largest q_2 sample ((0–55)% of the smallest q_2 sample) measured with TPC, or by randomly rejecting 70% of the TPC tracks leads to average variation of v_2 in $0.2 < p_T < 4$ GeV/c comparable to the one obtained by selecting standard largest (smallest) 10% q_2 events measured with V0C [110].

Figure 79 shows the ratio of p_T -differential yield from q_2 -selected events to that of unbiased events for different centrality classes in Pb–Pb collisions at $\sqrt{s_{NN}} = 2.76$ TeV with ALICE [110]. q_2 estimated from ALICE TPC is also compared to that measured with the V0C detector. To reduce the auto-correlation bias of measuring both q_2 from TPC and particle p_T -spectra, q_2 measurement is performed with charged particles in $|\eta| < 0.4$ while the p_T -spectra is measured with particles in $0.5 < |\eta| < 0.8$. It is observed that large- q_2 events possess a harder p_T -

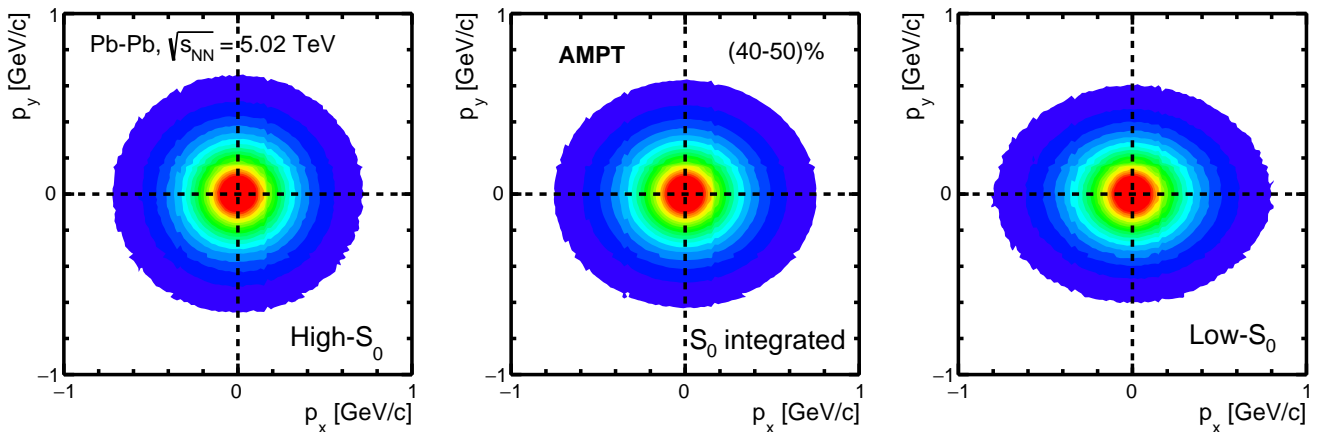


FIG. 70. Transverse momentum space correlation (p_x vs p_y) for different classes of transverse sphericity and (40-50)% centrality class in Pb-Pb collisions at $\sqrt{s_{NN}} = 5.02$ TeV using AMPT. High- S_0 and low- S_0 events have the highest 20% and lowest 20% value in the transverse sphericity distribution, respectively [68].

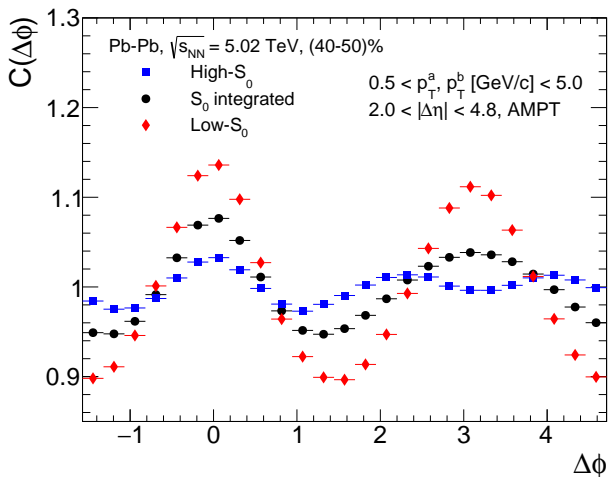


FIG. 71. Two-particle azimuthal correlation function for different transverse sphericity classes in (40-50)% centrality Pb-Pb collisions at $\sqrt{s_{NN}} = 5.02$ TeV using AMPT [68, 70].

spectra as compared to small- q_2 events. Further, the transverse momentum spectra of the large (small) q_2^{TPC} are harder (softer) than that of events selected with q_2^{V0C} .

C. Role of machine learning

Most of the event topology studies in heavy-ion collisions have only been performed using MC simulations based on phenomenological models so far. As the studies are CPU-intensive, machine learning tools can be used for their estimation in heavy-ion collisions. Machine learning tools such as boosted decision trees and

deep neural network models are quite popular in the high-energy physics community due to their accuracy and robustness in regression and classification tasks. These models are usually trained with a simulated dataset obtained from phenomenological models that best describe the real-world data. The training dataset contains a set of input variables and the corresponding output variable, or the target. The machine is trained to capture the input-output correlations, hence, a careful consideration of the input variables can be made, which can help in training the model. For the estimation of transverse sphericity [168], average charged-particle multiplicity ($\langle dN_{ch}/d\eta \rangle$), average charged-particle multiplicity in the transverse region ($\langle N_{ch}^{\text{TS}} \rangle$), mean transverse momentum ($\langle p_T \rangle$) are chosen as input observables. Figure 80 shows the correlation matrix among the input variables ($\langle dN_{ch}/d\eta \rangle$, $\langle N_{ch}^{\text{TS}} \rangle$, $\langle p_T \rangle$) and target variable (S_0) in Pb-Pb collisions at $\sqrt{s_{NN}} = 5.02$ TeV from AMPT model. The numbers inside the boxes represent the strength of correlation on a scale ranging from -1 to 1, where (-)1 means strong (anti)correlation. These correlation coefficients (ρ) are calculated for any given variables x and y as, $\rho = \text{cov}(x, y) / \sigma_x \sigma_y$. Here, cov is the covariance and σ is the standard deviation. From the figure, it is observed that the $\langle dN_{ch}/d\eta \rangle$ and $\langle N_{ch}^{\text{TS}} \rangle$ have positive correlation with the S_0 .

For this supervised regression task, a gradient boosted decision tree model is trained. Decision trees are mathematical structures that make decisions based on certain rules to split and direct the outcome to other decision points. Such decision points are called nodes. A single tree begins from a root node and can continue splitting recursively into further internal nodes. The number of internal nodes can be controlled via the `maximum depth` feature of the tree. Splitting is based on minimizing the node impurity. In regression tasks, the node impurity can be measured via either least-squares or least-absolute-

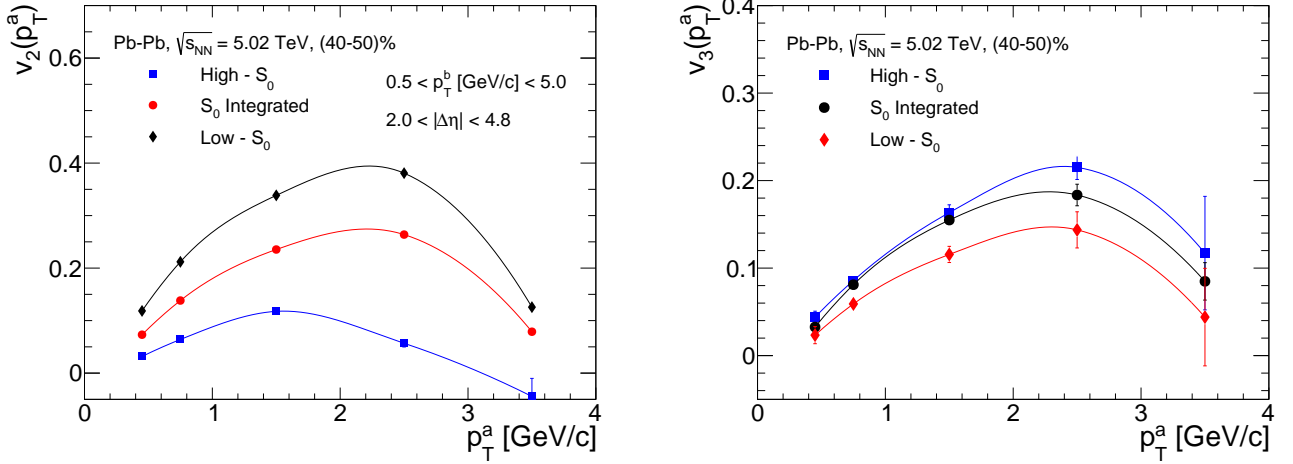


FIG. 72. Elliptic (top) and triangular (bottom) flow as a function of transverse momentum in (40-50)% centrality for different sphericity selections in Pb-Pb collisions at $\sqrt{s_{NN}} = 5.02$ TeV using AMPT [68, 70].

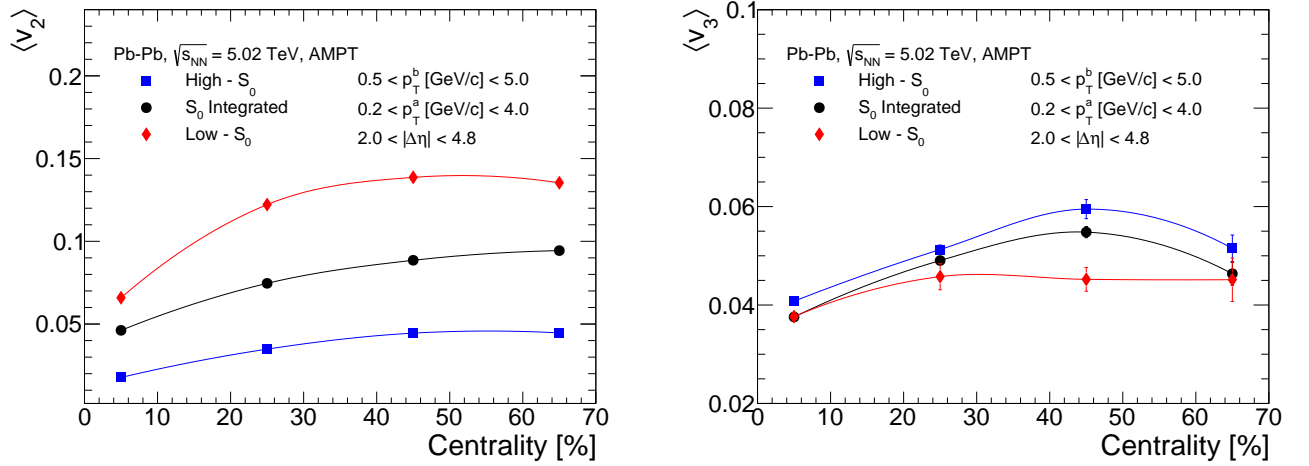


FIG. 73. Elliptic (top) and triangular (bottom) flow as a function of centrality for different sphericity selections in Pb-Pb collisions at $\sqrt{s_{NN}} = 5.02$ TeV using AMPT [70].

deviation. In gradient boosting, many such trees are grown in a forward stage-wise fashion, iteratively. The shortcomings of the previous tree, identified as the gradients, can be compensated for by the next tree. The maximum number of such trees can also be optimized to obtain the best prediction. In a nutshell, the training of the model involves optimizing the model parameters such that the loss function is minimized. The loss function quantifies the difference between the true value and the predicted value from the model.

The training of the model is influenced by a number of factors, such as the number of training examples (or events) in the training dataset and the choice of the loss functions. To evaluate the quality of training against

these two parameters, one can study the mean-absolute error of the target observable, *i.e.*, ΔS_0 , as defined below,

$$\Delta S_0 = \frac{1}{N_{\text{events}}} \sum_{n=1}^{N_{\text{events}}} |S_0^{\text{true}} - S_0^{\text{pred}}|. \quad (41)$$

By increasing the training data size from 10K to 50K events, ΔS_0 varies from 0.068 to 0.056. Further increasing the training data size to 60K events and beyond does not seem to decrease ΔS_0 as it saturates at the value of 0.055. This decrease in the value of ΔS_0 or increase in accuracy of the model with increasing the training data size is trivial to understand, since the model learns bet-

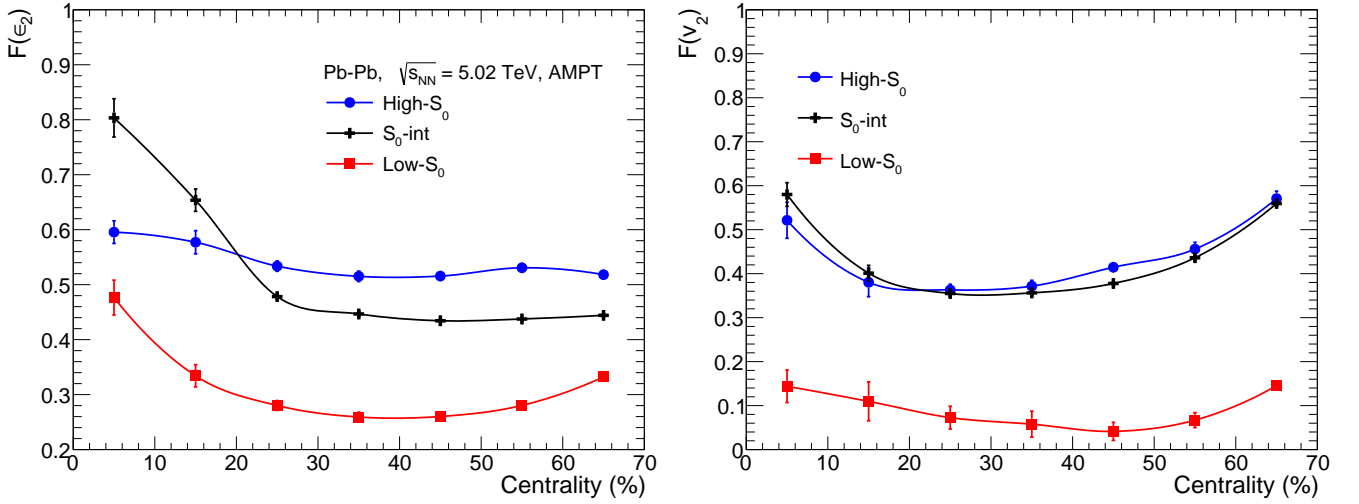


FIG. 74. $F(\epsilon_2)$ (left) and $F(v_2)$ (right) as a function of collision centrality for different classes of transverse sphericity in Pb-Pb collisions at $\sqrt{s_{NN}} = 5.02$ TeV using AMPT [71].

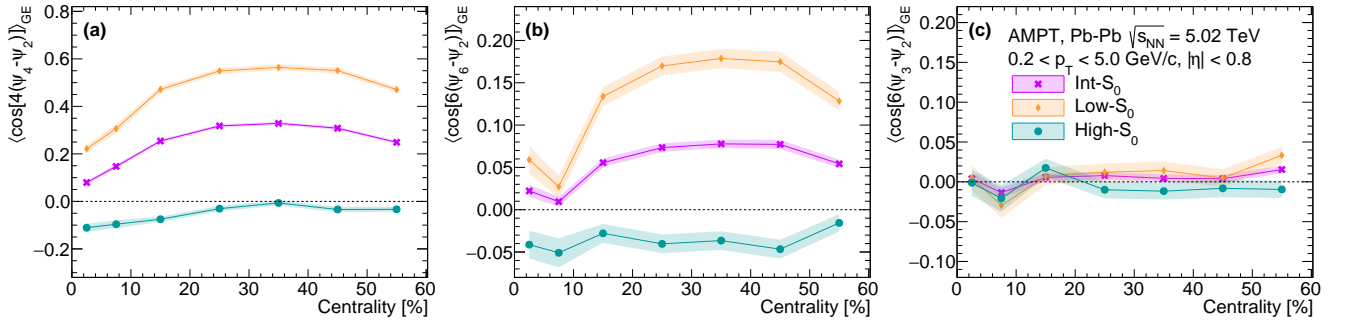


FIG. 75. Transverse sphericity and collision centrality dependence of symmetry plane correlations using Gaussian Estimator in Pb-Pb collisions at $\sqrt{s_{NN}} = 5.02$ TeV using AMPT [66].

ter with more training examples, yet, it is expected to saturate at some point, when no further information is learned beyond a certain limit.

Similarly, to understand the behavior of the loss function and boosting iteration trade-off on training of the model, three different models are trained with a varying number of trees. The left panel of Fig. 81 shows the evolution of mean-absolute error (ΔS_0) with increasing number of boosting iterations (number of trees) using the GBDT models with different loss functions. It is seen that, with increasing the number of trees, the ΔS_0 curves seem to fall exponentially and approaches zero quickly. The loss curves saturate and remain unaffected by further increases in boosting iterations beyond 80. Again, the small value of ΔS_0 indicates a better learning of the model. Among the three models, the model with the least-squares loss seems to learn faster with a minimum value of ΔS_0 for each boosting iteration, hence, it is chosen to be the default method for this study.

After fixing the training data size, the loss function, and the number of boosting iterations, one can com-

pare the predictions of the model to the true value of S_0 . The right panel of Fig. 81 shows the direct comparison between the GBDT model prediction vs. the true value of S_0 from minimum bias Pb-Pb collisions at $\sqrt{s_{NN}} = 5.02$ TeV using AMPT on an event-by-event basis. For most of the events, a good agreement between the true and predicted values of S_0 is observed, which also populates the $S_0^{\text{true}} = S_0^{\text{pred.}}$ curve. However, deviations from the true value of S_0 can still be seen, which is more prominent for lower values of S_0 (jetty-like events) compared to the higher values of S_0 (isotropic events). The minimum bias dataset contains mostly isotropic events than jetty-like events in Pb-Pb collisions, which is evident from Fig. 69. Therefore, the trained model performs better with events that are isotropic than jetty-like as far as predicting the exact value of S_0 is concerned.

The transverse sphericity distributions in minimum bias Pb-Pb collisions at $\sqrt{s_{NN}} = 5.02$ and 2.76 TeV are shown in Fig. 82 based on the GBDT model training discussed so far. The predicted sphericity distribution is compared with the true distribution obtained

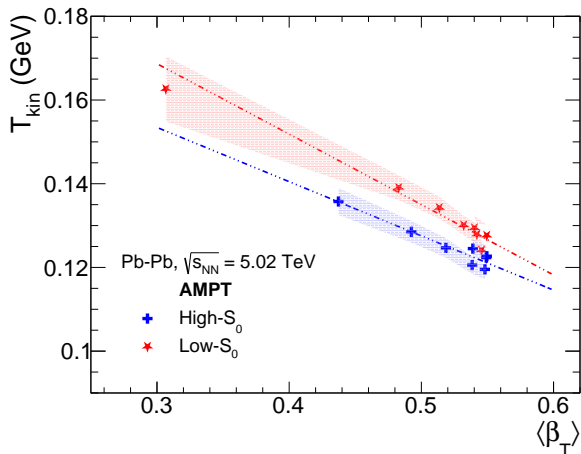


FIG. 76. Transverse sphericity dependence of kinetic freeze-out temperature (T_{kin}) versus mean transverse radial flow velocity ($\langle\beta_T\rangle$) extracted from a simultaneous fit of Boltzmann-Gibbs Blastwave function to identified particle transverse momentum spectra in Pb-Pb collisions at $\sqrt{s_{NN}} = 5.02$ TeV using AMPT [67].

from the AMPT simulation. It is evident that the ML-based regression method using GBDT accurately predicts the sphericity distribution for Pb-Pb collisions at $\sqrt{s_{NN}} = 5.02$ TeV. However, a discrepancy is observed in the low- S_0 region, likely due to the lower probability of events evolving to be jetty-like in the final-state in heavy-ion collisions compared to those with an isotropic nature. Therefore, this deviation is probably caused by limited statistics in the low- S_0 range, which is further indicated by the statistical uncertainty band (in black) in the lower ratio panel for the true distribution itself. The model trained with 5.02 TeV data can also predict the sphericity distribution for Pb-Pb collisions at $\sqrt{s_{NN}} = 2.76$ TeV. This suggests that the correlation between sphericity distributions and input variables remains consistent across LHC energies. Similar statistical fluctuations in the prediction for low- S_0 events can also be seen for 2.76 TeV case as well.

The discussed work in this subsection serves as a baseline for future developments aimed at full-scale applications in collider experiments focused on event shape observables. The possible next steps would be to incorporate detector effects, such as p_T resolution, smearing of the measured input observables, and the inclusion of additional parameters in the training. Advanced ML models could also be explored for further testing. With the advent of advanced ML models in the era of big data, the applicability of ML in various directions of the event-shape studies to understand multi-hadron production dynamics will remain a promising research domain.

VI. FINAL WORDS ON EACH CLASSIFIER

Let us now summarize the conclusions from each event classifier.

- **Impact parameter** In heavy-ion collisions, the impact parameter (b) of a collision is one of the crucial parameters that has a significant impact on the final state particle production. However, experimental measurement of such a quantity is nearly impossible in experiments as the length scale ranges in the level of a few fermi. Thus, experimental data are typically categorised by the collision centrality. A well-established Glauber model formalism is developed to estimate the impact parameter and number of participants from experimental data, which considers multiple scattering of nucleons in nuclear targets.
- **Charged-particle multiplicity in mid- and forward-rapidity:** The trend of mid-rapidity multiplicity dependent results shows the similar MPI-dependent behavior of strangeness enhancement, baryon-to-meson ratios, and $\langle p_T \rangle$. However, they are highly prone to auto-correlation bias and selection bias to high- p_T yields. Multiplicity measured in forward-rapidity shows a significant reduction of auto-correlation bias with respect to midrapidity multiplicity classes, but it is prone to a selection bias of choosing high- $\langle p_T \rangle$ particles.
- **Number of multi-parton interactions:** In microscopic models like PYTHIA 8, MPI plays a pivotal role in particle production. The results from MPI-based selections give us a reference while studying different event classifiers used in this manuscript. As MPI cannot be measured directly in experiments, the essence of this review work is to find an appropriate proxy for the studies on QGP-like effects. While comparing the p_T spectra of pions in different N_{mpi} classes, we found that the high- p_T yields tend to approach the value found in minimum bias collisions irrespective of N_{mpi} classes, which is in contrast to the rising trend seen when one compares pion p_T spectra as a function of multiplicity classes. Furthermore, a clear strangeness enhancement (suppression) is seen for high (low) multiplicity pp collisions when studied as a function of the number of multi-parton interactions. It is also found that the strangeness enhancement saturates for high-MPI regions.
- **Transverse sphero(i)city:** Due to an implicit requirement of a minimum number of charged particles being larger than 10 to have a statistically meaningful concept of a topology, the MPI reach of sphero(i)city selection is limited towards intermediate and high MPI. From model studies, transverse sphero(i)city is found to have a marginal effect

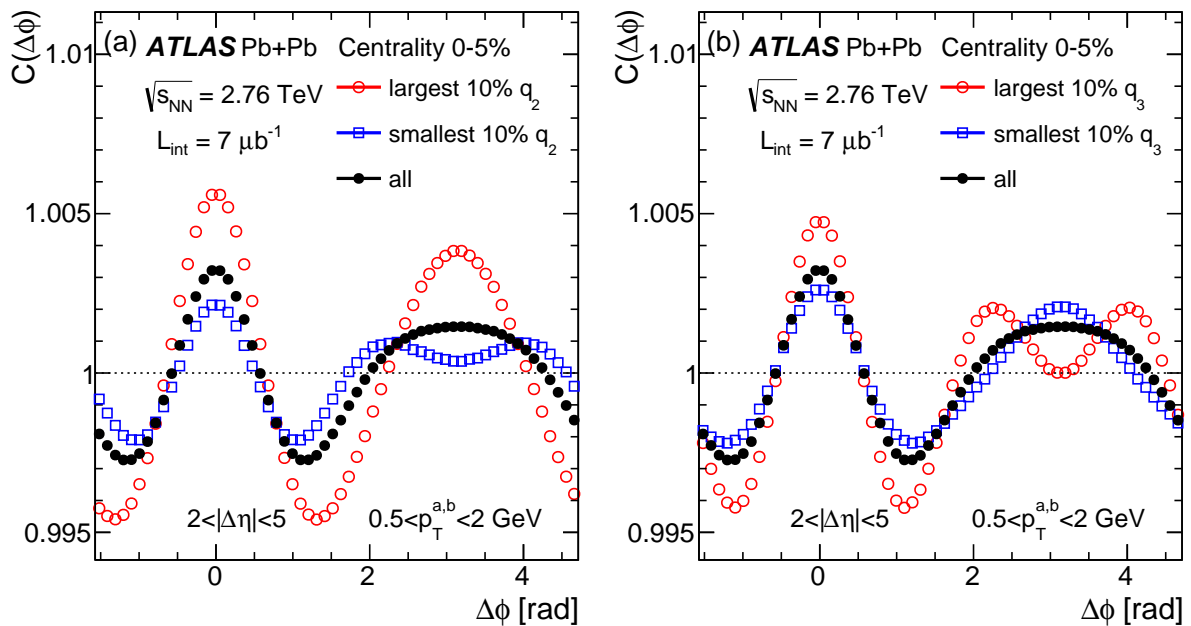


FIG. 77. Azimuthal dependence of two-particle correlation function ($C(\Delta\phi)$) versus q_2 (left) and q_3 (right) for 0-5% centrality class in Pb-Pb collisions at $\sqrt{s_{NN}} = 2.76$ TeV with ATLAS [108].

on strangeness enhancement. The isotropic events show larger baryon-to-meson ratios compared to jetty events. A similar behavior of strangeness enhancement and baryon-to-meson ratios is observed when studied as a function of transverse sphericity. However, quantitatively, the strangeness enhancement and baryon-to-meson ratios in isotropic events (defined using transverse sphericity) are less compared to the studies based on transverse sphericity. In addition, the usage of p_T -unweighted definition of sphericity, introduced by the ALICE experiment, results in larger enhancement of strangeness in high-multiplicity pp collisions with respect to the traditional definition of transverse sphericity.

- **Relative transverse activity classifier:** With a high transverse momentum cut for trigger particle, one probes a semi-hard QCD domain ($\langle p_T \rangle > 10$ GeV/c) with R_T , which is unlike any other classifiers discussed in this manuscript. The studies based on R_T in the transverse region show significant auto-correlation bias, which is expected as R_T is calculated in the transverse region. However, the towards region, which is free from multiplicity selection biases for R_T study, shows mild effects of QGP-like behavior as expected from MPI-based classifier.
- **Charged-particle flattenicity:** The most recent event shape observable, charged-particle flattenicity, is found to be most suited for the study of QGP-like behavior in small systems in the soft-QCD

domain ($\langle p_T \rangle < 10$ GeV/c). It shows a similar quantitative strangeness enhancement and baryon-to-meson ratios as seen for the studies based on the number of multi-parton interactions. Charged-particle flattenicity is found to have the least selection biases to hard particle production, and thus, is the preferred classifier for future multi-differential experimental studies. However, it is worth mentioning that, to make the studies coherent and detector/experiment-independent, one needs to employ an unfolding procedure to retrieve a true flattenicity distribution from the folded distributions with the detector effects.

VII. OUTLOOK

As discussed in this manuscript, event shape observables have proven to be valuable tools in understanding the underlying dynamics of pp collisions. They offer key insights into QCD dynamics and serve as a bridge between theory and experimental measurements. Event shape observables are expected to be instrumental in testing the QCD, as, by construction, they are collinear and infrared safe observables. Thus, they do not change their value if a parton is split into two collinear partons or an extra soft gluon is added. This is an important condition for the cancellation of divergences associated with such gluon emissions, which makes them ideal tools for making finite perturbative QCD predictions. In addition, these event-shape classifiers have shown a significant correlation with MPI, which makes them the ideal tool for the

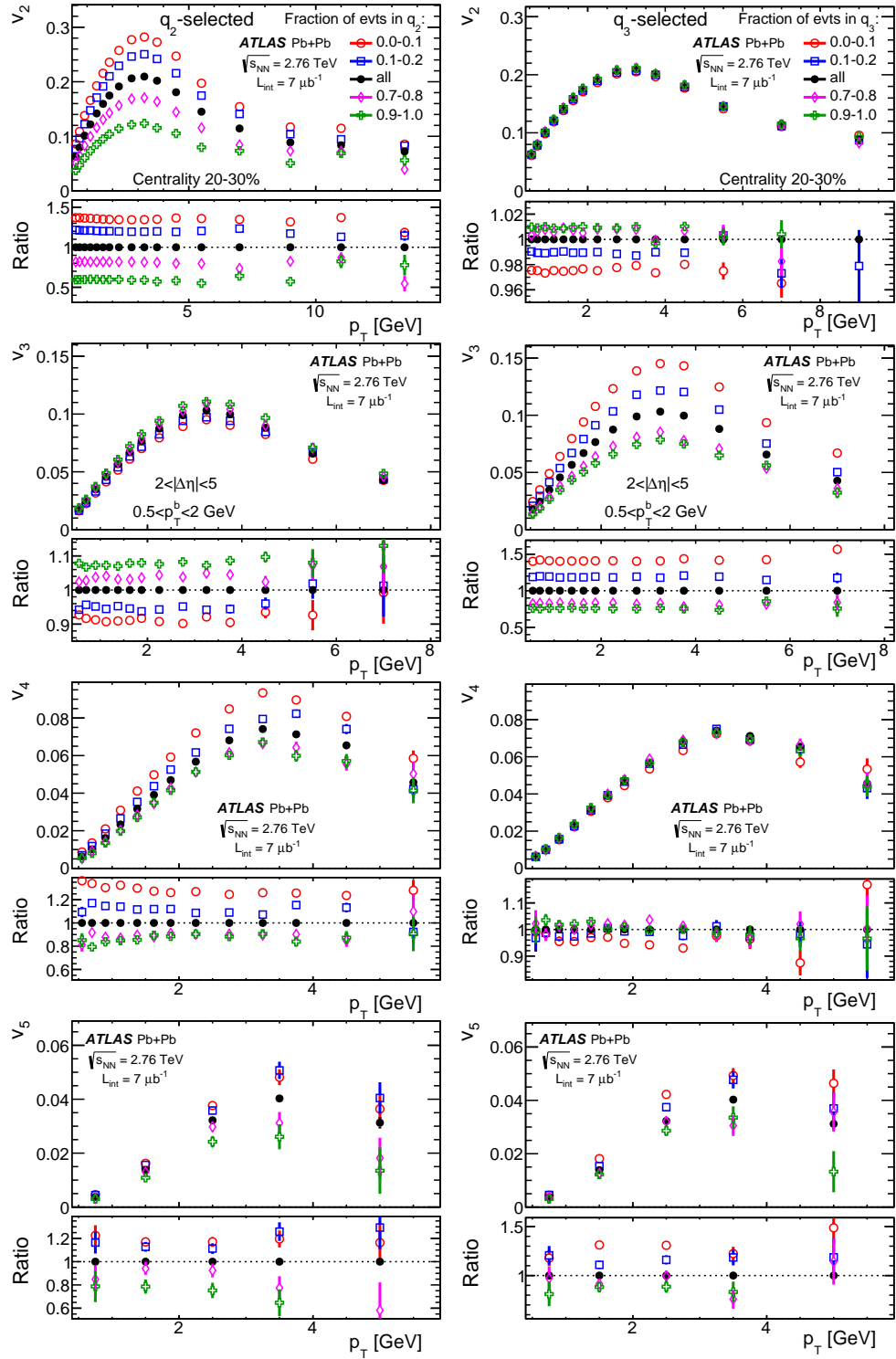


FIG. 78. p_T -differential anisotropic flow coefficients versus q_2 (left) and q_3 (right) in Pb-Pb collisions at $\sqrt{s_{NN}} = 2.76$ TeV with ATLAS [108].

understanding of QGP-like effects. Thus, these are nearly perfect observables to be used as event estimators as they can probe both perturbative and non-perturbative QCD sectors.

Thus, over the last decade, extensive theoretical and phenomenological research has been carried out in the domain of event shape observables in small systems, however, limited statistics have prevented experimentalists

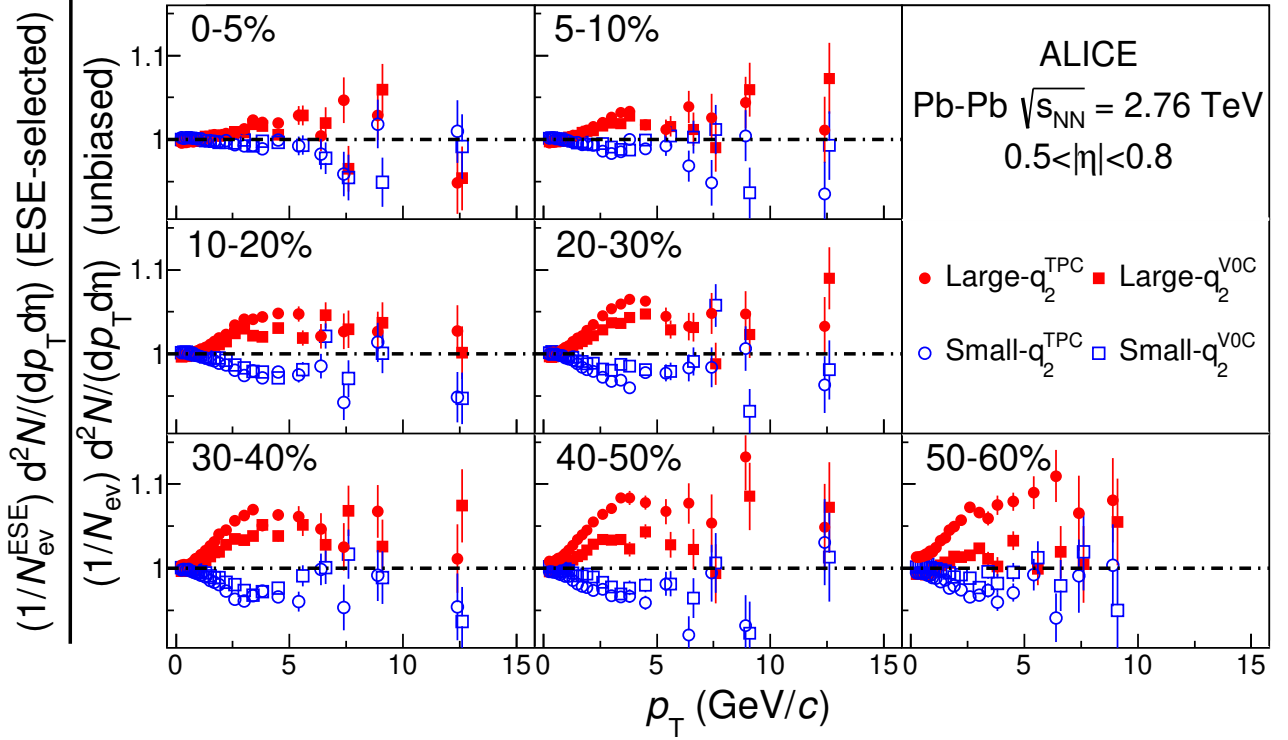


FIG. 79. Ratio of p_T -spectra of different event-shape-engineering (ESE) selected events using q_2 estimated with ALICE TPC and V0C detectors to p_T -spectra of unbiased events for different centrality classes in Pb-Pb collisions at $\sqrt{s_{NN}} = 2.76$ TeV with ALICE [110].

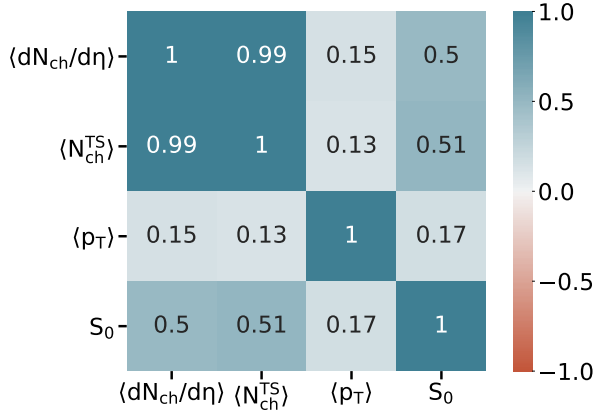


FIG. 80. Correlation matrix showing the values of the correlation coefficients among the input variables ($\langle dN_{ch}/d\eta \rangle$, $\langle N_{ch}^{TS} \rangle$, $\langle p_T \rangle$) and target variable (S_0) in Pb-Pb collisions at $\sqrt{s_{NN}} = 5.02$ TeV using AMPT [168].

from using these observables to perform precision studies. In addition, due to a lack of statistics, no experimental measurements of the heavy flavors using event shapes have been performed. Given significantly higher

statistics would be available in Runs 3 and 4 of the LHC with respect to Runs 1 and 2, all the above-discussed event-classifiers can be experimentally used to probe the discussed observables with a high level of precision. As shown in the manuscript, the usage of event shape observables can be even extended to heavy-ion collisions, which will also bring different collision systems on equal footing. Thanks to machine learning models, handling large datasets has become more feasible, which is also highlighted in the manuscript.

In summary, this review article will provide a baseline for future experimental studies, which will give a clear insight into the microscopic origin of QGP-like behavior in small collision systems at the LHC and hopefully, in the next decade, one can get a clear picture if small systems collectivity originates from macroscopic features like the formation of QGP or from microscopic mechanisms like string interactions.

ACKNOWLEDGMENTS

S.P. and B.S. acknowledge the doctoral fellowships from the UGC and CSIR, Government of India. S.T. acknowledges the CERN Research Fellowship and the funding received from the European Union's Horizon Eu-

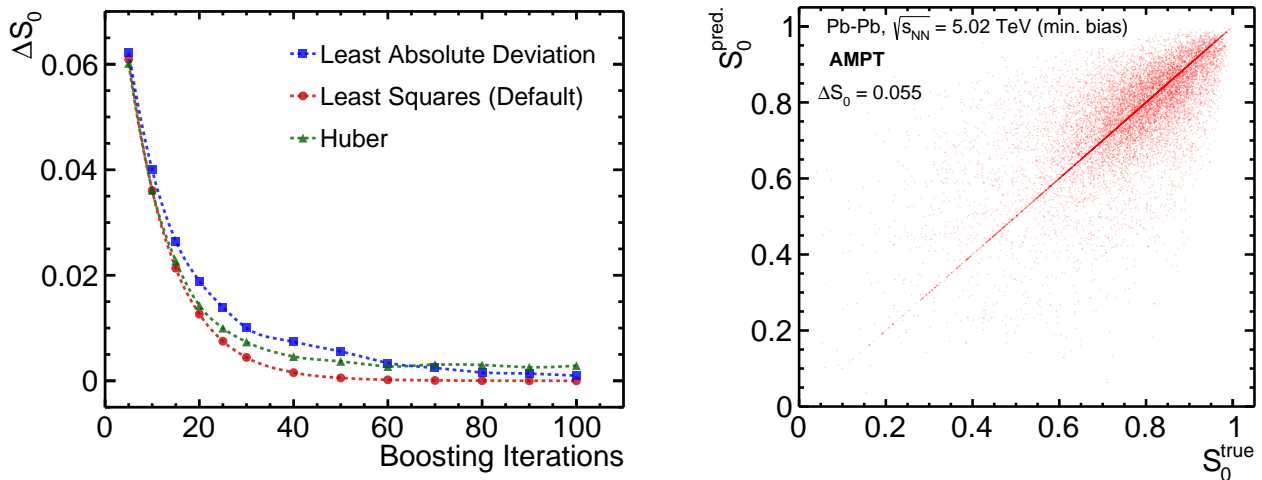


FIG. 81. (Top) Evolution of mean-absolute error (ΔS_0) with increasing number of boosting iterations (number of trees) using GBDT models trained with different loss functions. (Bottom) The predicted sphericity from the GBDT model compared to the true sphericity in Pb–Pb collisions at $\sqrt{s_{NN}} = 5.02$ TeV using AMPT [168].

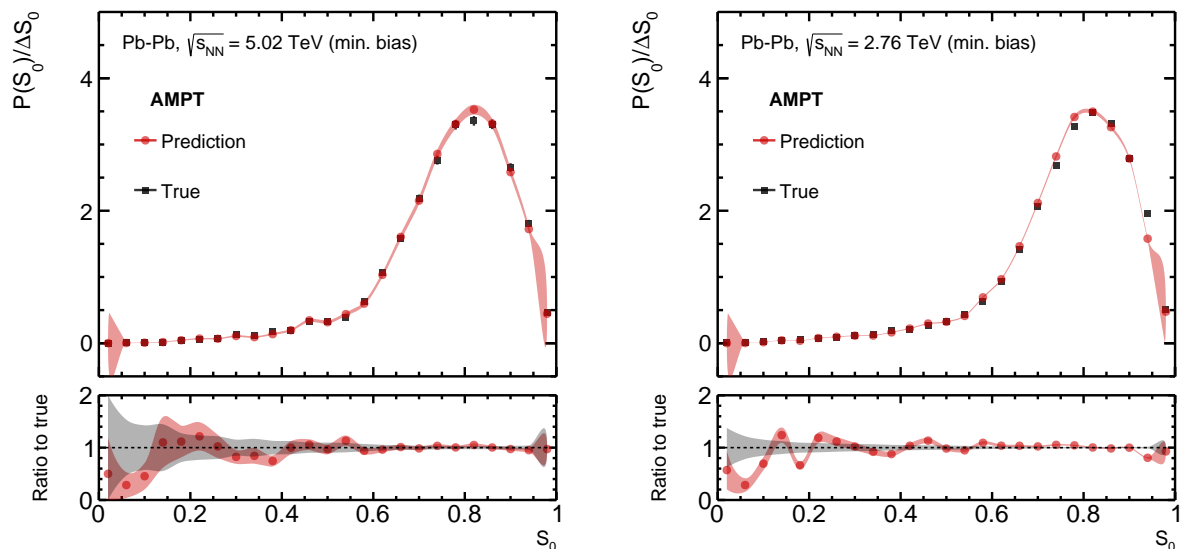


FIG. 82. Predicted sphericity distribution from the GBDT model (red) compared to the true sphericity distribution from AMPT (black) for Pb–Pb collisions at $\sqrt{s_{NN}} = 5.02$ TeV (left) and 2.76 TeV (right). Bottom panels show the ratio of predicted to true curves [168].

rope research and innovation programme under the Marie Skłodowska-Curie grant agreement No. 101149298. The authors acknowledge the DAE-DST, Government of India, funding under the Mega-Science Project—“Indian participation in the ALICE experiment at CERN” bearing Project No. SR/MF/PS-02/2021- IITI (E-37123).

The authors acknowledge Neelkamal Mallick for the discussion on the heavy-ion related studies. S.T. acknowledges discussion with Alexander Philipp Kalweit and Alice Ohlson during the preparation of this manuscript.

[1] M. Diehl, D. Ostermeier and A. Schafer, Elements of a theory for multiparton interactions in QCD, JHEP **03**,

089 (2012) [erratum: JHEP **03**, 001 (2016)].

- [2] R. Field, The underlying event in hadronic collisions, *Ann. Rev. Nucl. Part. Sci.* **62**, 453 (2012).
- [3] P. Christiansen and P. Van Mechelen, “Soft QCD Physics at the LHC: highlights and opportunities,” [arXiv:2412.02672 [hep-ex]].
- [4] T. Sjöstrand and M. van Zijl, A Multiple Interaction Model for the Event Structure in Hadron Collisions, *Phys. Rev. D* **36**, 2019 (1987).
- [5] S. Chekanov *et al.* [ZEUS], Three- and four-jet final states in photoproduction at HERA, *Nucl. Phys. B* **792**, 1 (2008).
- [6] V. M. Abazov *et al.* [D0], Double parton interactions in $\gamma+3$ jet events in pp^- bar collisions $\sqrt{s} = 1.96$ TeV., *Phys. Rev. D* **81**, 052012 (2010).
- [7] T. Sjöstrand *et al.*, An introduction to PYTHIA 8.2, *Comput. Phys. Commun.* **191**, 159 (2015).
- [8] V. Khachatryan *et al.* [CMS], Evidence for collectivity in pp collisions at the LHC, *Phys. Lett. B* **765**, 193 (2017).
- [9] J. F. Grosse-Oetringhaus and U. A. Wiedemann, “A Decade of Collectivity in Small Systems,” [arXiv:2407.07484 [hep-ex]].
- [10] S. Acharya *et al.* [ALICE], Investigations of Anisotropic Flow Using Multiparticle Azimuthal Correlations in pp , p-Pb, Xe-Xe, and Pb-Pb Collisions at the LHC, *Phys. Rev. Lett.* **123**, 142301 (2019).
- [11] V. Khachatryan *et al.* [CMS], Observation of Long-Range Near-Side Angular Correlations in Proton-Proton Collisions at the LHC, *JHEP* **09**, 091 (2010).
- [12] G. Aad *et al.* [ATLAS], Observation of Long-Range Elliptic Azimuthal Anisotropies in $\sqrt{s} = 13$ and 2.76 TeV pp Collisions with the ATLAS Detector, *Phys. Rev. Lett.* **116**, 172301 (2016).
- [13] V. Khachatryan *et al.* [CMS], Measurement of long-range near-side two-particle angular correlations in pp collisions at $\sqrt{s} = 13$ TeV, *Phys. Rev. Lett.* **116**, 172302 (2016).
- [14] M. Aaboud *et al.* [ATLAS], Measurements of long-range azimuthal anisotropies and associated Fourier coefficients for pp collisions at $\sqrt{s} = 5.02$ and 13 TeV and p+Pb collisions at $\sqrt{s_{NN}} = 5.02$ TeV with the ATLAS detector, *Phys. Rev. C* **96**, 024908 (2017).
- [15] W. Busza, K. Rajagopal and W. van der Schee, Heavy Ion Collisions: The Big Picture, and the Big Questions, *Ann. Rev. Nucl. Part. Sci.* **68**, 339 (2018).
- [16] S. Acharya *et al.* [ALICE], First observation of ultra-long-range azimuthal correlations in low multiplicity pp and p-Pb collisions at the LHC, [arXiv:2504.02359].
- [17] J. Adam *et al.* [ALICE], Enhanced production of multi-strange hadrons in high-multiplicity proton-proton collisions, *Nature Phys.* **13**, 535 (2017).
- [18] S. Acharya *et al.* [ALICE], Multiplicity dependence of light-flavor hadron production in pp collisions at $\sqrt{s} = 7$ TeV, *Phys. Rev. C* **99**, 024906 (2019).
- [19] S. Acharya *et al.* [ALICE], Multiplicity dependence of (multi-)strange hadron production in proton-proton collisions at $\sqrt{s} = 13$ TeV, *Eur. Phys. J. C* **80**, 167 (2020).
- [20] J. L. Nagle and W. A. Zajc, Small System Collectivity in Relativistic Hadronic and Nuclear Collisions, *Ann. Rev. Nucl. Part. Sci.* **68**, 211 (2018).
- [21] S. Acharya *et al.* [ALICE], Search for jet quenching effects in high-multiplicity pp collisions at $\sqrt{s} = 13$ TeV via di-jet acoplanarity, *JHEP* **05**, 229 (2024).
- [22] C. Bierlich and J. R. Christiansen, Effects of color reconnection on hadron flavor observables, *Phys. Rev. D* **92**, 094010 (2015).
- [23] C. Bierlich, G. Gustafson, L. Lönnblad and A. Tarasov, Effects of Overlapping Strings in pp collisions, *JHEP* **03**, 148 (2015).
- [24] C. Bierlich, G. Gustafson and L. Lönnblad, A shoving model for collectivity in hadronic collisions, [arXiv:1612.05132].
- [25] S. Acharya *et al.* [ALICE], Charged-particle production as a function of multiplicity and transverse sphericity in pp collisions at $\sqrt{s} = 5.02$ and 13 TeV, *Eur. Phys. J. C* **79**, 857 (2019).
- [26] S. Acharya *et al.* [ALICE], Study of charged-particle production at high p_T using event topology in pp , p-Pb and Pb-Pb collisions at $\sqrt{s_{NN}} = 5.02$ TeV, *Phys. Lett. B* **843**, 137649 (2023).
- [27] P. A. Movilla Fernandez *et al.* [JADE], A Study of event shapes and determinations of α_s using data of e^+e^- annihilations at $\sqrt{s} = 22$ to 44-GeV, *Eur. Phys. J. C* **1**, 461 (1998).
- [28] J. F. Donoghue, F. E. Low and S. Y. Pi, Tensor Analysis of Hadronic Jets in Quantum Chromodynamics, *Phys. Rev. D* **20**, 2759 (1979).
- [29] M. Dasgupta and G. P. Salam, Event shapes in e^+e^- annihilation and deep inelastic scattering, *J. Phys. G* **30**, R143 (2004).
- [30] A. Banfi, G. P. Salam and G. Zanderighi, Resummed event shapes at hadron - hadron colliders, *JHEP* **08**, 062 (2004).
- [31] S. Bethke *et al.* [JADE], Determination of the Strong Coupling α_s from hadronic Event Shapes with $O(\alpha_s^3)$ and resummed QCD predictions using JADE Data, *Eur. Phys. J. C* **64**, 351 (2009).
- [32] M. Z. Akrawy *et al.* [OPAL], A Study of Jet Production Rates and a Test of QCD on the Z0 Resonance, *Phys. Lett. B* **235**, 389 (1990).
- [33] W. Bartel *et al.* [JADE], Observation of Four - Jet Structure in e^+e^- Annihilation at $\sqrt{s} = 33$ -GeV, *Phys. Lett. B* **115**, 338 (1982).
- [34] S. Brandt, C. Peyrou, R. Sosnowski and A. Wroblewski, The Principal axis of jets. An Attempt to analyze high-energy collisions as two-body processes, *Phys. Lett.* **12**, 57 (1964).
- [35] G. Aad *et al.* [ATLAS], Measurement of event shapes at large momentum transfer with the ATLAS detector in pp collisions at $\sqrt{s} = 7$ TeV, *Eur. Phys. J. C* **72**, 2211 (2012).
- [36] V. Khachatryan *et al.* [CMS], First Measurement of Hadronic Event Shapes in pp Collisions at $\sqrt{s} = 7$ TeV, *Phys. Lett. B* **699**, 48 (2011).
- [37] A. Banfi, G. P. Salam and G. Zanderighi, Phenomenology of event shapes at hadron colliders, *JHEP* **06**, 038 (2010).
- [38] C. Adler *et al.* [STAR], Elliptic flow from two and four particle correlations in Au+Au collisions at $\sqrt{s_{NN}} = 130$ -GeV, *Phys. Rev. C* **66**, 034904 (2002).
- [39] C. Cesarotti and J. Thaler, A Robust Measure of Event Isotropy at Colliders, *JHEP* **08**, 084 (2020).
- [40] T. Martin, P. Skands and S. Farrington, Probing Collective Effects in Hadronisation with the Extremes of the Underlying Event, *Eur. Phys. J. C* **76** 299 (2016).
- [41] G. Bencedi, A. Ortiz and A. Paz, Disentangling the hard gluon bremsstrahlung effects from the relative trans-

- verse activity classifier in pp collisions, *Phys. Rev. D* **104**, 016017 (2021).
- [42] A. Ortiz and L. Valencia Palomo, Universality of the underlying event in pp collisions, *Phys. Rev. D* **96**, 114019 (2017).
- [43] S. G. Weber, A. Dubla, A. Andronic and A. Morsch, Elucidating the multiplicity dependence of J/ψ production in proton-proton collisions with PYTHIA8, *Eur. Phys. J. C* **79**, 36 (2019).
- [44] B. Abelev *et al.* [ALICE], Transverse sphericity of primary charged particles in minimum bias proton-proton collisions at $\sqrt{s} = 0.9, 2.76$ and 7 TeV, *Eur. Phys. J. C* **72**, 2124 (2012).
- [45] V. Chekhovsky *et al.* [CMS], Measurement of event shapes in minimum-bias events from proton-proton collisions at $\sqrt{s} = 13$ TeV, [arXiv:2505.17850].
- [46] G. Aad *et al.* [ATLAS], Measurement of charged-particle event shape variables in $\sqrt{s} = 7$ TeV proton-proton interactions with the ATLAS detector, *Phys. Rev. D* **88**, 032004 (2013).
- [47] B. Abelev *et al.* [ALICE], Underlying Event measurements in pp collisions at $\sqrt{s} = 0.9$ and 7 TeV with the ALICE experiment at the LHC, *JHEP* **07**, 116 (2012).
- [48] S. Acharya *et al.* [ALICE], Event-shape and multiplicity dependence of freeze-out radii in pp collisions at $\sqrt{s} = 7$ TeV, *JHEP* **09**, 108 (2019).
- [49] S. Acharya *et al.* [ALICE], Underlying Event properties in pp collisions at $\sqrt{s} = 13$ TeV, *JHEP* **04**, 192 (2020).
- [50] S. Acharya *et al.* [ALICE], Underlying-event properties in pp and p-Pb collisions at $\sqrt{s_{NN}} = 5.02$ TeV, *JHEP* **06**, 023 (2023).
- [51] S. Acharya *et al.* [ALICE], Production of pions, kaons, and protons as a function of the relative transverse activity classifier in pp collisions at $\sqrt{s} = 13$ TeV, *JHEP* **06**, 027 (2023).
- [52] S. Acharya *et al.* [ALICE], Charged-particle production as a function of the relative transverse activity classifier in pp , p-Pb, and Pb-Pb collisions at the LHC, *JHEP* **01**, 056 (2024).
- [53] S. Acharya *et al.* [ALICE], Light-flavor particle production in high-multiplicity pp collisions at $\sqrt{s} = 13$ TeV as a function of transverse sphericity, *JHEP* **05**, 184 (2024).
- [54] S. Acharya *et al.* [ALICE], Modification of charged-particle jets in event-shape engineered Pb-Pb collisions at $\sqrt{s_{NN}} = 5.02$ TeV, *Phys. Lett. B* **851**, 138584 (2024).
- [55] S. Acharya *et al.* [ALICE], Particle production as a function of charged-particle flatness in pp collisions at $\sqrt{s} = 13$ TeV, *Phys. Rev. D* **111**, 012010 (2025).
- [56] R. Rath, A. Khuntia, S. Tripathy and R. Sahoo, A Baseline Study of the Event-Shape and Multiplicity Dependence of Chemical Freeze-Out Parameters in Proton-Proton Collisions at $\sqrt{s} = 13$ TeV Using PYTHIA8, *Physics* **2**, 679 (2020).
- [57] S. Tripathy, A. Bisht, R. Sahoo, A. Khuntia and M. P. Salvan, Event Shape and Multiplicity Dependence of Freeze-Out Scenario and System Thermodynamics in Proton+Proton Collisions at $\sqrt{s} = 13$ TeV Using PYTHIA8, *Adv. High Energy Phys.* **2021**, 8822524 (2021).
- [58] A. Khuntia, S. Tripathy, A. Bisht and R. Sahoo, Event shape engineering and multiplicity dependent study of identified particle production in proton + proton collisions at $\sqrt{s} = 13$ TeV using PYTHIA8, *J. Phys. G* **48**, 035102 (2021).
- [59] A. M. K. R., S. Prasad, S. Tripathy, N. Mallick and R. Sahoo, Investigating radial-flow-like effects via pseudorapidity and transverse sphericity dependence of particle production in pp collisions at the LHC, *Eur. Phys. J. Plus* **140**, 110 (2025).
- [60] S. Prasad, B. Sahoo, S. Tripathy, N. Mallick and R. Sahoo, Probing strangeness with event topology classifiers in pp collisions at energies available at the CERN Large Hadron Collider with the rope hadronization mechanism in PYTHIA, *Phys. Rev. C* **111**, 044902 (2025).
- [61] S. Deb, R. Sahoo, D. Thakur, S. Tripathy and A. Khuntia, Investigating heavy-flavor vs light-flavor puzzle with event topology and multiplicity in proton + proton collisions at $\sqrt{s} = 13$ TeV using PYTHIA8, *J. Phys. G* **48**, 095104 (2021).
- [62] A. Khatun, D. Thakur, S. Deb and R. Sahoo, J/ψ production dynamics: event shape, multiplicity and rapidity dependence in proton+proton collisions at LHC energies using PYTHIA8, *J. Phys. G* **47**, 055110 (2020).
- [63] S. Deb, G. Sarwar, R. Sahoo and J. e. Alam, Study of QCD dynamics using small systems, *Eur. Phys. J. A* **57**, 195 (2021).
- [64] S. Deb, S. Tripathy, G. Sarwar, R. Sahoo and J. e. Alam, Deciphering QCD dynamics in small collision systems using event shape and final state multiplicity at the Large Hadron Collider, *Eur. Phys. J. A* **56**, 252 (2020).
- [65] N. Mallick, S. Tripathy, R. Sahoo and A. Ortiz, First implementation of transverse sphericity analysis for heavy-ion collisions at the Large Hadron Collider energies, [arXiv:2001.06849].
- [66] S. Tripathy, S. Prasad and R. Sahoo, Event shape dependence of symmetry plane correlations using the Gaussian estimator in Pb-Pb collisions at the LHC using AMPT, [arXiv:2504.09275].
- [67] S. Prasad, N. Mallick, D. Behera, R. Sahoo and S. Tripathy, Event topology and global observables in heavy-ion collisions at the Large Hadron Collider, *Sci. Rep.* **12**, 3917 (2022).
- [68] N. Mallick, R. Sahoo, S. Tripathy and A. Ortiz, Study of Transverse Sphericity and Azimuthal Anisotropy in Pb-Pb collisions at $\sqrt{s_{NN}} = 5.02$ TeV using A Multi-Phase Transport Model, *J. Phys. G* **48**, 045104 (2021).
- [69] N. Mallick, S. Tripathy and R. Sahoo, Event topology and constituent-quark scaling of elliptic flow in heavy-ion collisions at the Large Hadron Collider using a multiphase transport model, *Eur. Phys. J. C* **82**, 524 (2022).
- [70] S. Prasad, N. Mallick, S. Tripathy and R. Sahoo, Probing initial geometrical anisotropy and final azimuthal anisotropy in heavy-ion collisions at Large Hadron Collider energies through event-shape engineering, *Phys. Rev. D* **107**, 074011 (2023).
- [71] S. Prasad, A. M. K. R., R. Sahoo and N. Mallick, Higher order flow coefficients – A Messenger of QCD medium formed in heavy-ion collisions at the Large Hadron Collider, [arXiv:2505.01471].
- [72] T. Akesson *et al.* [Axial Field Spectrometer], The Dominance of Jets at Large Transverse Energy in a Full Azimuth Hadron Calorimeter at ISR Energies, *Phys. Lett. B* **128**, 354 (1983).
- [73] C. Albajar *et al.* [UA1], Analysis of the Highest Transverse Energy Events Seen in the UA1 Detector at the $SppS$ Collider, *Z. Phys. C* **36**, 33 (1987).

- [74] R. Ansari *et al.* [UA2], Jet Measures and Hadronic Event Shapes at the CERN $\bar{p}p$ Collider, *Z. Phys. C* **36** (1987), 175
- [75] T. Aaltonen *et al.* [CDF], Measurement of Event Shapes in Proton-Antiproton Collisions at Center-of-Mass Energy 1.96 TeV, *Phys. Rev. D* **83**, 112007 (2011).
- [76] P. A. Movilla Fernandez, S. Bethke, O. Biebel and S. Kluth, Tests of power corrections for event shapes in e^+e^- annihilation, *Eur. Phys. J. C* **22**, 1 (2001).
- [77] S. Chekanov *et al.* [ZEUS], Measurement of event shapes in deep inelastic scattering at HERA, *Eur. Phys. J. C* **27**, 531 (2003).
- [78] P. Achard *et al.* [L3], Determination of α_s from hadronic event shapes in e^+e^- annihilation at $192 \leq \sqrt{s} \leq 208$ GeV, *Phys. Lett. B* **536**, 217 (2002).
- [79] A. Heister *et al.* [ALEPH], Studies of QCD at e^+e^- centre-of-mass energies between 91-GeV and 209-GeV, *Eur. Phys. J. C* **35**, 457 (2004).
- [80] J. Abdallah *et al.* [DELPHI], The Measurement of α_s from event shapes with the DELPHI detector at the highest LEP energies, *Eur. Phys. J. C* **37**, 1 (2004).
- [81] G. Abbiendi *et al.* [OPAL], Measurement of event shape distributions and moments in $e^+e^- \rightarrow$ hadrons at 91-GeV - 209-GeV and a determination of α_s , *Eur. Phys. J. C* **40**, 287 (2005).
- [82] A. Aktas *et al.* [H1], Measurement of event shape variables in deep-inelastic scattering at HERA, *Eur. Phys. J. C* **46**, 343 (2006).
- [83] Z. W. Lin, C. M. Ko, B. A. Li, B. Zhang and S. Pal, A Multi-phase transport model for relativistic heavy ion collisions, *Phys. Rev. C* **72**, 064901 (2005).
- [84] Y. He and Z. W. Lin, Improved Quark Coalescence for a Multi-Phase Transport Model, *Phys. Rev. C* **96**, 014910 (2017).
- [85] B. Abelev *et al.* [ALICE], Measurement of inelastic, single- and double-diffraction cross sections in proton-proton collisions at the LHC with ALICE, *Eur. Phys. J. C* **73**, 2456 (2013).
- [86] M. L. Miller, K. Reygers, S. J. Sanders and P. Steinberg, Glauber modeling in high energy nuclear collisions, *Ann. Rev. Nucl. Part. Sci.* **57**, 205 (2007).
- [87] C. Loizides, Glauber modeling of high-energy nuclear collisions at sub-nucleon level, *Phys. Rev. C* **94**, 024914 (2016).
- [88] R. J. Glauber and G. Matthiae, High-energy scattering of protons by nuclei, *Nucl. Phys. B* **21**, 135 (1970).
- [89] C. Y. Wong, Introduction to High-Energy Heavy-Ion Collisions (World Scientific, Singapore, 1994).
- [90] P. F. Kolb, U. Heinz, P. Huovinen, K. J. Eskola, K. Tuominen, Centrality dependence of multiplicity, transverse energy, and elliptic flow from hydrodynamics, *Nucl. Phys. A* **696**, 197 (2001).
- [91] Sebastian Bysiak, The Fast Interaction Trigger Upgrade for ALICE". In: Proceedings PoS (LHCP2020) 382, 251 (2020).
- [92] "Technical Design Report for the Muon Forward Tracker," tech. rep., (2015). <https://cds.cern.ch/record/1981898>.
- [93] A. Hayrapetyan *et al.* [CMS], Pseudorapidity distributions of charged hadrons in lead-lead collisions at $\sqrt{s_{NN}} = 5.36$ TeV, *Phys. Lett. B* **861**, 139279 (2025).
- [94] S. Chatrchyan *et al.* [CMS], Dependence on pseudorapidity and centrality of charged hadron production in PbPb collisions at a nucleon-nucleon centre-of-mass energy of 2.76 TeV, *JHEP* **08**, 141 (2011).
- [95] V. Khachatryan *et al.* [CMS], Charged-particle Multiplicities in pp Interactions at $\sqrt{s} = 0.9, 2.36$, and 7 TeV, *JHEP* **01**, 079 (2011).
- [96] G. Aad *et al.* [ATLAS], Charged-particle multiplicities in pp interactions measured with the ATLAS detector at the LHC, *New J. Phys.* **13**, 053033 (2011).
- [97] G. Aad *et al.* [ATLAS], Charged-particle multiplicities in pp interactions at $\sqrt{s} = 900$ GeV measured with the ATLAS detector at the LHC, *Phys. Lett. B* **688**, 21 (2010).
- [98] G. Aad *et al.* [ATLAS], Charged-particle distributions in $\sqrt{s} = 13$ TeV pp interactions measured with the ATLAS detector at the LHC, *Phys. Lett. B* **758**, 67 (2016).
- [99] T. Sjostrand and P. Z. Skands, Multiple interactions and the structure of beam remnants, *JHEP* **03**, 053 (2004).
- [100] P. Bartalini, E. L. Berger, B. Blok, G. Calucci, R. Corke, M. Diehl, Y. Dokshitzer, L. Fano, L. Frankfurt and J. R. Gaunt, *et al.*, Multi-Parton Interactions at the LHC, [arXiv:1111.0469].
- [101] G. Hanson, G. S. Abrams, A. Boyarski, M. Breidenbach, F. Bulos, W. Chinowsky, G. J. Feldman, C. E. Friedberg, D. Fryberger and G. Goldhaber, *et al.*, Evidence for Jet Structure in Hadron Production by e^+e^- Annihilation, *Phys. Rev. Lett.* **35**, 1609 (1975).
- [102] E. Cuautle, R. Jimenez, I. Maldonado, A. Ortiz, G. Paic and E. Perez, Disentangling the soft and hard components of the pp collisions using the spher(o)city approach, [arXiv:1404.2372].
- [103] A. Ortiz, G. Paic and E. Cuautle, Mid-rapidity charged hadron transverse sphericity in pp collisions simulated with Pythia, *Nucl. Phys. A* **941**, 78 (2015).
- [104] A. Ortiz, Experimental results on event shapes at hadron colliders, *Adv. Ser. Dir. High Energy Phys.* **29**, 343 (2018).
- [105] A. Ortiz and G. Paic, A look into the "hedgehog" events in pp collisions, *Rev. Mex. Fis. Suppl.* **3**, 040911 (2022).
- [106] A. Ortiz, A. Khuntia, O. Vázquez-Rueda, S. Tripathy, G. Bencedi, S. Prasad and F. Fan, Unveiling the effects of multiple soft partonic interactions in pp collisions at $\sqrt{s} = 13.6$ TeV using a new event classifier, *Phys. Rev. D* **107**, 076012 (2023).
- [107] S. Prasad [ALICE], presented in Quark Matter 2025 conference, Available Online: <https://indico.cern.ch/event/1334113/contributions/6291974/>
- [108] G. Aad *et al.* [ATLAS], Measurement of the correlation between flow harmonics of different order in lead-lead collisions at $\sqrt{s_{NN}} = 2.76$ TeV with the ATLAS detector, *Phys. Rev. C* **92**, 034903 (2015).
- [109] A. M. Sirunyan *et al.* [CMS], Study of the underlying event in top quark pair production in pp collisions at 13 TeV, *Eur. Phys. J. C* **79**, 123 (2019).
- [110] J. Adam *et al.* [ALICE], Event shape engineering for inclusive spectra and elliptic flow in Pb-Pb collisions at $\sqrt{s_{NN}} = 2.76$ TeV, *Phys. Rev. C* **93**, 034916 (2016).
- [111] D. P. Barber, U. Becker, H. Benda, A. Boehm, J. G. Branson, J. Bron, D. Buikman, J. Burger, C. C. Chang and H. S. Chen, *et al.*, Discovery of Three Jet Events and a Test of Quantum Chromodynamics at PETRA Energies, *Phys. Rev. Lett.* **43**, 830 (1979).
- [112] L. Clavelli and D. Wyler, Kinematical Bounds on Jet Variables and the Heavy Jet Mass Distribution, *Phys. Lett. B* **103**, 383 (1981).

- [113] B. Adeva *et al.* [L3], Studies of hadronic event structure and comparisons with QCD models at the Z0 resonance, *Z. Phys. C* **55**, 39 (1992).
- [114] O. Adrian *et al.* [L3], Determination of α_s from hadronic event shapes measured on the Z0 resonance, *Phys. Lett. B* **284**, 471 (1992).
- [115] M. Acciarri *et al.* [L3], Study of the structure of hadronic events and determination of α_s at $\sqrt{s} = 130$ GeV and 136 GeV, *Phys. Lett. B* **371**, 137 (1996).
- [116] M. Acciarri *et al.* [L3], QCD studies and determination of α_s in e^+e^- collisions at $\sqrt{s} = 161$ GeV and 172 GeV, *Phys. Lett. B* **404**, 390 (1997).
- [117] M. Acciarri *et al.* [L3], Study of hadronic events and measurements of α_s between 30 GeV and 91 GeV, *Phys. Lett. B* **411**, 339 (1997).
- [118] M. Acciarri *et al.* [L3], QCD results from studies of hadronic events produced in e^+e^- annihilations at $\sqrt{s} = 183$ GeV, *Phys. Lett. B* **444**, 569 (1998).
- [119] M. Acciarri *et al.* [L3], QCD studies in e^+e^- annihilation from 30 GeV to 189 GeV, *Phys. Lett. B* **489**, 65 (2000).
- [120] P. Achard *et al.* [L3], Studies of hadronic event structure in e^+e^- annihilation from 30 GeV to 209 GeV with the L3 detector, *Phys. Rept.* **399**, 71 (2004).
- [121] W. Kittel and E. A. De Wolf, *Soft multihadron dynamics*, World Scientific (2005).
- [122] S. Catani, G. Turnock and B. R. Webber, Jet broadening measures in e^+e^- annihilation, *Phys. Lett. B* **295**, 269 (1992).
- [123] S. Catani, L. Trentadue, G. Turnock and B. R. Webber, Resummation of large logarithms in e^+e^- event shape distributions, *Nucl. Phys. B* **407**, 3 (1993).
- [124] B. Andersson, G. Gustafson, G. Ingelman and T. Sjöstrand, Parton Fragmentation and String Dynamics, *Phys. Rept.* **97**, 31 (1983).
- [125] R. Corke and T. Sjöstrand, Interleaved Parton Showers and Tuning Prospects, *JHEP* **03**, 032 (2011).
- [126] T. Sjöstrand, S. Mrenna and P. Z. Skands, A Brief Introduction to PYTHIA 8.1, *Comput. Phys. Commun.* **178**, 852 (2008).
- [127] Pythia8 online manual: <https://pythia.org/latest-manual/Welcome.html>.
- [128] P. Skands, S. Carrazza and J. Rojo, Tuning PYTHIA 8.1: the Monash 2013 Tune, *Eur. Phys. J. C* **74**, 3024 (2014).
- [129] B. Andersson, G. Gustafson and B. Soderberg, A General Model for Jet Fragmentation, *Z. Phys. C* **20**, 317 (1983).
- [130] S. Argyropoulos and T. Sjöstrand, Effects of color reconnection on $t\bar{t}$ final states at the LHC, *JHEP* **11**, 043 (2014).
- [131] R. J. Fries, B. Muller, C. Nonaka and S. A. Bass, Hadron production in heavy ion collisions: Fragmentation and recombination from a dense parton phase, *Phys. Rev. C* **68**, 044902 (2003).
- [132] R. J. Fries, B. Muller, C. Nonaka and S. A. Bass, Hadronization in heavy ion collisions: Recombination and fragmentation of partons, *Phys. Rev. Lett.* **90**, 202303 (2003).
- [133] X. N. Wang and M. Gyulassy, HIJING: A Monte Carlo model for multiple jet production in p p, p A and A A collisions, *Phys. Rev. D* **44**, 3501 (1991).
- [134] B. Zhang, ZPC 1.0.1: A Parton cascade for ultrarelativistic heavy ion collisions, *Comput. Phys. Commun.* **109**, 193 (1998).
- [135] Z. w. Lin and C. M. Ko, Partonic effects on the elliptic flow at RHIC, *Phys. Rev. C* **65**, 034904 (2002).
- [136] B. Li, A. T. Sustich, B. Zhang and C. M. Ko, Studies of superdense hadronic matter in a relativistic transport model, *Int. J. Mod. Phys. E* **10**, 267 (2001).
- [137] V. Greco, C. M. Ko and P. Levai, Parton coalescence at RHIC, *Phys. Rev. C* **68**, 034904 (2003).
- [138] S. Tripathy, S. De, M. Younus and R. Sahoo, Predictions for azimuthal anisotropy in Xe+Xe collisions at $\sqrt{s_{NN}} = 5.44$ TeV using a multiphase transport model, *Phys. Rev. C* **98**, 064904 (2018).
- [139] A. Ortiz, A. Paz, J. D. Romo, S. Tripathy, E. A. Zepeda and I. Bautista, Multiparton interactions in pp collisions from machine learning-based regression, *Phys. Rev. D* **102**, 076014 (2020).
- [140] S. Acharya *et al.* [ALICE], Multiplicity dependence of π , K, and p production in pp collisions at $\sqrt{s} = 13$ TeV, *Eur. Phys. J. C* **80**, 693 (2020).
- [141] S. Acharya *et al.* [ALICE], The ALICE experiment: a journey through QCD, *Eur. Phys. J. C* **84**, 813 (2024).
- [142] A. Ortiz Velasquez, P. Christiansen, E. Cuautle Flores, I. Maldonado Cervantes and G. Paic, Color Reconnection and Flowlike Patterns in pp Collisions, *Phys. Rev. Lett.* **111**, 042001 (2013).
- [143] S. Acharya *et al.* [ALICE], Production of charged pions, kaons, and (anti-)protons in Pb-Pb and inelastic pp collisions at $\sqrt{s_{NN}} = 5.02$ TeV, *Phys. Rev. C* **101**, 044907 (2020).
- [144] A. Ortiz, G. Bencedi and H. Bello, Revealing the source of the radial flow patterns in proton-proton collisions using hard probes, *J. Phys. G* **44**, 065001 (2017).
- [145] J. Y. Ollitrault, Anisotropy as a signature of transverse collective flow, *Phys. Rev. D* **46**, 229 (1992).
- [146] Z. F. Jiang, C. B. Yang and Q. Peng, Directed flow of charged particles within idealized viscous hydrodynamics at energies available at the BNL Relativistic Heavy Ion Collider and at the CERN Large Hadron Collider, *Phys. Rev. C* **104**, 064903 (2021).
- [147] S. Acharya *et al.* [ALICE], Observation of partonic flow in proton-proton and proton-nucleus collisions, [arXiv:2411.09323].
- [148] J. Adams *et al.* [STAR], Particle type dependence of azimuthal anisotropy and nuclear modification of particle production in Au + Au collisions at $\sqrt{s_{NN}} = 200$ -GeV, *Phys. Rev. Lett.* **92**, 052302 (2004).
- [149] A. M. Sirunyan *et al.* [CMS], Elliptic flow of charm and strange hadrons in high-multiplicity pPb collisions at $\sqrt{s_{NN}} = 8.16$ TeV, *Phys. Rev. Lett.* **121**, 082301 (2018).
- [150] Y. C. Chen, Y. Chen, A. Badea, A. Baty, G. M. Innocenti, M. Maggi, C. McGinn, M. Peters, T. A. Sheng and J. Thaler, *et al.*, Long-range near-side correlation in e^+e^- collisions at 183-209 GeV with ALEPH archived data, *Phys. Lett. B* **856**, 138957 (2024).
- [151] T. Bonnevier Wallstedt, Investigation of event-shape classifiers for proton-proton collisions with the ALICE experiment, Student Paper, Lund University, (2024). Available at: <http://lup.lub.lu.se/student-papers/record/9160009>.
- [152] S. Acharya *et al.* [ALICE], Transverse momentum spectra and nuclear modification factors of charged particles in pp , p-Pb and Pb-Pb collisions at the LHC, *JHEP* **11**, 013 (2018).

- [153] S. Acharya *et al.* [ALICE], Constraints on jet quenching in p-Pb collisions at $\sqrt{s_{NN}} = 5.02$ TeV measured by the event-activity dependence of semi-inclusive hadron-jet distributions, *Phys. Lett. B* **783**, 95 (2018).
- [154] S. Acharya *et al.* [ALICE], Measurements of jet quenching using semi-inclusive hadron+jet distributions in *pp* and central Pb-Pb collisions at $\sqrt{s_{NN}} = 5.02$ TeV, *Phys. Rev. C* **110**, 014906 (2024).
- [155] J. Adams *et al.* [STAR], Direct observation of dijets in central Au+Au collisions at $\sqrt{s_{NN}} = 200$ -GeV, *Phys. Rev. Lett.* **97**, 162301 (2006).
- [156] K. Aamodt *et al.* [ALICE], Particle-yield modification in jet-like azimuthal di-hadron correlations in Pb-Pb collisions at $\sqrt{s_{NN}} = 2.76$ TeV, *Phys. Rev. Lett.* **108**, 092301 (2012).
- [157] J. Adam *et al.* [ALICE], Jet-like correlations with neutral pion triggers in *pp* and central Pb-Pb collisions at 2.76 TeV, *Phys. Lett. B* **763**, 238 (2016).
- [158] G. Y. Qin and X. N. Wang, Jet quenching in high-energy heavy-ion collisions, *Int. J. Mod. Phys. E* **24**, 1530014 (2015).
- [159] S. Acharya *et al.* [ALICE], Symmetry plane correlations in Pb-Pb collisions at $\sqrt{s_{NN}} = 2.76$ TeV, *Eur. Phys. J. C* **83**, 576 (2023).
- [160] R. S. Bhalerao, M. Luzum and J. Y. Ollitrault, Determining initial-state fluctuations from flow measurements in heavy-ion collisions, *Phys. Rev. C* **84**, 034910 (2011).
- [161] S. Acharya *et al.* [ALICE], Higher-order symmetry plane correlations in Pb-Pb collisions at $\sqrt{s_{NN}} = 5.02$ TeV, [arXiv:2409.04238].
- [162] J. Jia, Event-shape fluctuations and flow correlations in ultra-relativistic heavy-ion collisions, *J. Phys. G* **41**, 124003 (2014).
- [163] H. Niemi, K. J. Eskola and R. Paatelainen, Event-by-event fluctuations in a perturbative QCD + saturation + hydrodynamics model: Determining QCD matter shear viscosity in ultrarelativistic heavy-ion collisions, *Phys. Rev. C* **93**, 024907 (2016).
- [164] J. Qian and U. Heinz, Hydrodynamic flow amplitude correlations in event-by-event fluctuating heavy-ion collisions, *Phys. Rev. C* **94**, 024910 (2016).
- [165] S. Acharya *et al.* [ALICE], Systematic studies of correlations between different order flow harmonics in Pb-Pb collisions at $\sqrt{s_{NN}} = 2.76$ TeV, *Phys. Rev. C* **97**, 024906 (2018).
- [166] J. Adam *et al.* [ALICE], Correlated event-by-event fluctuations of flow harmonics in Pb-Pb collisions at $\sqrt{s_{NN}} = 2.76$ TeV, *Phys. Rev. Lett.* **117**, 182301 (2016).
- [167] H. Niemi, G. S. Denicol, H. Holopainen and P. Huovinen, Event-by-event distributions of azimuthal asymmetries in ultrarelativistic heavy-ion collisions, *Phys. Rev. C* **87**, 054901 (2013).
- [168] N. Mallick, S. Tripathy, A. N. Mishra, S. Deb and R. Sahoo, Estimation of Impact Parameter and Transverse Sphericity in heavy-ion collisions at the LHC energies using Machine Learning, *Phys. Rev. D* **103**, 094031 (2021).